Probabilistic Fracture Mechanics of Forged Rotor Disks

Zur Erlangung des akademischen Grades
Doktor der Ingenieurwissenschaften
der Fakultät Maschinenbau
Karlsruher Institut für Technologie (KIT)

genehmigte
Dissertation
von

Dipl.-Phys.Ing. Christian Amann

Tag der mündlichen Prüfung: 4. Mai 2017
Hauptreferent: Prof. Dr. rer. nat. Peter Gumbsch
Korreferent: Prof. Dr.-Ing. Hans-Jörg Bauer

Abstract

The methodology described in this work enables the calculation of a conservative estimate of the *Probability of Failure* (*PoF*) of large land based gas turbines due to fatigue crack growth from inherent forging flaws. The developed *Probabilistic Fracture Mechanics* code (*ProbFM*) accounts for the variability of material and inherent flaw properties in large rotor forgings of land based gas turbines.

The results obtained by this method are *Probability of Failure* versus applied stress cycles and risk contour maps of the components based on the statistics of input quantities, i.e. material and flaw property distributions. Risk contour maps give insight into the critical areas of the component and this information can be used — for instance — to optimize ultrasonic inspections. The method yields an integral robust fracture mechanics evaluation and shows the fracture mechanical critical regions of the component. Furthermore, different operational conditions during the life cycle can be accounted for. As the calculated *Probability of Failure* versus applied stress cycles is in general a smooth function, it can be used in the optimization of component geometry and material selection.

One major objective for the development of the methodology is that the calculated *Probability of Failure* has to be an upper bound of the real *Probability of Failure*. The consequences of a rotor failure can be severe, as the kinetic energy stored in a typical large gas turbine rotor is on the order of the kinetic energy of 100 40t trucks each traveling at 100km/h.

For the same reason, the acceptable risk of failure has to be very low – typically on the order of one in a million. To resolve such small risks accurately in a *Brute Force Monte Carlo Simulation*, a large number (i.e. millions to billions) of individual crack assessment calculations have to be performed. To tackle such a computationally challenging approach, the developed code is optimized for fast calculation and a highly efficient ordinary differential equation solver has been developed. For additional speed, the code has been parallelized and tested on up to 500 interconnected CPUs simultaneously.

The developed method is geared towards large land-based gas turbine rotor forgings. However, it can be applied to other technical components including aero engines, steam turbine components and electrical generator forgings, as well as parts of renewable power plants. In general the method can also be applied to calculate the *Probability of Failure* of other technical components. It enables risk management, which is a significant improvement compared to the traditional deterministic safe life assessment which yields no information of associated risks.

Zusammenfassung

Die in dieser Arbeit beschriebenen Ansätze und Methoden ermöglichen es, eine konservative Abschätzung der Versagenswahrscheinlichkeit (PoF) von großen, stationären Gasturbinen aufgrund von inhärenten Schmiedefehlern zu berechnen. Die entwickelte Analysesoftware $ProbFM$ berücksichtigt dabei die Variabilität der Eigenschaften von Material und inhärenten Schmiedefehlern von großen, stationären Gasturbinen.

Die Ergebnisse, welche mit dieser Methode erzeugt werden, sind eine Versagenswahrscheinlichkeit als Funktion der Anzahl der Zyklen und Risikokarten der analysierten Komponenten, basierend auf den statistischen Eingabegrößen, wie zum Beispiel der Verteilungen von Material- und Fehlereigenschaften. Die Risikokarten geben einen Einblick in die kritischen Bereiche einer Komponente und können zum Beispiel zur Optimierung von Ultraschalluntersuchungen verwendet werden. Die Methode liefert eine robuste, integrale bruchmechanische Bewertung und zeigt die bruchmechanisch kritischen Bereiche einer Komponente. Zusätzlich können unterschiedliche Betriebsbedingungen während der Lebensdauer einer Komponente berücksichtigt werden. Da die berechnete Versagenswahrscheinlichkeit als Funktion der Anzahl der Zyklen im Allgemeinen eine glatte Funktion ist, kann diese auch bei der Optimierung der Komponente in Bezug auf ihre Geometrie und Materialauswahl verwendet werden.

Eine wesentliche Randbedingung bei der Entwicklung der beschriebenen Methode war, dass die berechnete Versagenswahrscheinlichkeit eine obere Abschätzung für die wirkliche Versagenswahrscheinlichkeit ist. Die Auswirkungen eines Rotorversagens einer großen, stationären Gasturbine können sehr schwerwiegend sein, da die gespeicherte kinetische Energie ungefähr der kinetischen Energie von 100 40t Lkws entspricht, wobei jeder mit einer Geschwindigkeit von 100km/h fährt.

Aus demselben Grund muss das akzeptable Risiko für ein Versagen sehr gering sein – üblicherweise in der Größenordnung von 1 in einer Million. Um solch geringe Risiken in einer Brute Force Monte Carlo Simulation zu beschreiben, ist eine große Anzahl (Millionen oder Milliarden) von individuellen Risssimulationen notwendig. Um solch einen rechentechnisch aufwändigen Ansatz zu realisieren, wurde der entwickelte Computer Code in Bezug auf kurze Rechenzeiten hin optimiert und ein effizienter Integrationsalgorithmus für einfache Differentialgleichungen entwickelt. Um die Berechnungszeit weiter zu reduzieren, wurde der Code für parallele Berechnung ausgelegt und auf bis zu 500 miteinander verbundenen CPUs getestet. Die entwickelte Methode ist spezifisch für große, stationäre Gasturbinen entwickelt worden, kann jedoch prinzipiell auch auf andere technische Komponenten, wie zum Beispiel Flugzeugtriebwerke, Dampfturbinen Komponenten und Generator Schmiedeteile, sowie für Teile aus z.B. Windkraftwerken angewendet werden. Zudem ermöglicht die entwickelte Methode das

Risikomanagement der analysierten Komponenten, was ein wesentlicher Vorteil gegenüber der traditionellen deterministischen Safe Life Auslegung ist, welche keine Aussage über das zugehörige Risiko liefert.

Acknowledgments

The presented work has been developed during my work at Siemens Gas Turbine and as Doctoral candidate at the Institute of Applied Materials at the Karlsruher Institute of Technology.

I would like to thank my thesis advisor Prof. Dr. rer. nat. Peter Gumbsch for advice and guidance.

My very special thanks goes to my advisor at Siemens GT Kai Kadau for many fruitful discussions, all the support and the good collaboration. Furthermore, I would like to thank the Siemens GT materials and technology and rotor component groups for supporting this work, specifically, Phillip Gravett, Dr. Georg Rollmann, Dr. Björn Beckmann, Dr. Sebastian Schmitz, Dr. Santosh Narasimhachary, Dr. Jose Pascual-Gutierrez, Dr. Karsten Kolk, Christopher Ross and Harald Hoell.

Also, I would like to thank Siemens GT for the support and to fund this research.

Finally, I thank my wife and family for their continued love and support.

Publications and Intellectual Property

Publications

C. Amann and K. Kadau, Numerically efficient modified Runge-Kutta solver for fatigue crack growth analysis, *Engineering Fracture Mechanics*, 2016, 161, 55-62

K. Kadau, C. Amann, and P. W. Gravett, Probabilistic fracture mechanics for heavy duty gas turbine forgings, Proceeddings of ASME Turbo Expo 2017, GT2017, submitted

K. Kadau, C. Amann, P. W. Gravett and P. Gumbsch, Direct Simulation Monte-Carlo Probabilistic Fracture Mechanics for Risk Management in the Energy Sector, in preparation

C. Amann, U. Hahn, M. Hesse and H. Schulte-Schrepping, Simulations of the pressure profiles of the PETRAIII frontends, *Journal of Physics: Conference Series*, 2008, 100, 092017

Intellectual Property

Method and system for probabilistic fatigue crack life estimation
Inventors: Christian Amann, Philip W. Gravett, Kai Kadau
US Patent Publication-Number: US20140107948 A1 (grant)
US Patent Application-Number: US 13/652,671 Year 2012
International Patent Publication-Number: WO2014/060160
International Patent Application-Number: PCT/EP2013/069096 Year 2013
Europe Patent Application-Number: 13762824.4 Year 2013
Chinese Patent Application-Number: 201380062999.6 Year 2013
Japanese Patent Application-Number: PCT/EP2013/069096 Year 2013
Korean Patent Application-Number: 2015-7012380 Year 2013

Verfahren zur Abschaetzung von Risslaengenfortschritten

Inventors: Christian Amann, Kai Kadau
US Patent Application-Number: US 14/282,081 Year 2014
Europe Patent Application-Number: 13169639.5 Year 2013

Verfahren zur Bestimmung der erwarteten Verteilung der inhärenten Fehlstellen in einem Bauteil
Inventors: Christian Amann, Kai Kadau
German Patent Application-Number: 102014209858.0 Year 2014

METHOD FOR ANALYSIS OF 3D FEATURES USING A 2D PROBABILISTIC ANALYSIS
Inventors: Kai Kadau, Christopher W. Ross, Chirag B. Patel, Christian Amann
US Patent Application-Number: US 14/314,159 Year 2014
International Patent Application Number: PCT/US2015/036870 Year 2015

4 additional Siemens trade secrets have been issued.

Contents

List of Figures

List of Tables

Nomenclature

Latin Symbols

ΔK	Stress intensity range	$[\,MPa\sqrt{m}\,]$
$\frac{da}{dN}$	Crack growth rate	$[\,m/cycle\,]$
a	Semiminor axis of the crack	[m]
a_{eff}	Effective crack length	[m]
C	Paris parameter	
c	Semimajor axis of the crack	[m]
E	Young's modulus	$[\,MPa\,]$
K	Stress intensity	$[\,MPa\sqrt{m}\,]$
k	Ultrasonic flaw size conversion factor	
K_{Ic}	Mode I fracture toughness	$[\,MPa\sqrt{m}\,]$
K_I	Mode I stress intensity	$[\,MPa\sqrt{m}\,]$
K_r	Stress intensity ratio	
KSR	Circular disk reflector	[m]
m	Paris exponent	
N	Number of cycles	
N_f	Number cycles to failure	
N_{ind}	Total number of indications	
N_t	Total number of inspected components	
P_X	Predicted value of property X	
PoD	Probability of detection	

PoF	Probability of failure	
Q	Flaw shape parameter	
Q_{eff}	Effective flaw shape parameter	
$q_{K_{Ic}}$	Fracture toughness - stress ratio	$[\sqrt{m}]$
R	Stress ratio	
r	Radius	[m]
r_p	Irwin plastic zone radius	$[m]$
r_y	Irwin crack length correction	$[m]$
S	Number of samples	
S_f	Number of failed samples	
s_{year}	Starts per year	
T	Temperature	$[°C]$
t	Plate thickness	$[m]$
T_{FATT}	50% Fracture appearance transition temperature	$[°C]$
T_{meas}	Measurement temperature	$[°C]$
T_{rel}	Relative temperature	
TFS	True flaw size	$[m]$
V_{tot}	Total volume of all inspected components	$[m^3]$
Y	Geometry factor	

Greek Symbols

$\Delta\sigma$	Stress range	$[MPa]$
ϵ_r	Relative residual	
ρ_{Flaw}	Mean volume based flaw density	$[1/m^3]$
σ	Stress	$[MPa]$

σ_c	Plastic collapse stress	$[\,MPa\,]$
σ_I	Mode I stress	$[\,MPa\,]$
σ_{max}	Maximum stress	$[\,MPa\,]$
σ_{min}	Minimum stress	$[\,MPa\,]$
σ_{RM}	Ultimate stress	$[\,MPa\,]$
σ_t	Tangential stress	$[\,MPa\,]$
σ_X	Standard deviation	
σ_{YS}	Yield stress	$[\,MPa\,]$

Subscripts

$_0$	Normalization Factor
$_b$	Bending
$_{III}$	Mode III
$_{II}$	Mode II
$_I$	Mode I
$_m$	Membrane

Abbreviations

FATT	50% Fracture Appearance Transition Temperature
ProbFM	Probabilistic Fracture Mechanics Code and Methodology
CDF	Cumulative Distribution Function
ECDF	Empirical Cumulative Distribution Function
FAD	Failure Assessment Diagram
IPZE	Irwin Plastic Zone Extension
IWM	Fraunhofer Institut für Werkstoffmechanik
LEFM	Linear Elastic Fracture Mechanics

MC Monte-Carlo

NDE Non Destructive Evaluation

PDF Probability Density Function

PFM Probabilistic Fracture Mechanics

SIF Stress Intensity Factor

TFS True Flaw Size

1. Introduction

In the manufacturing of technical components, it is not possible to control all variables like geometry, material properties, flaws, etc., such that all produced components are exactly the same. Therefore, in a deterministic assessment these variations are captured by 'worst' case assumptions e.g. 'minimum' material properties, 'largest' assumed crack sizes or 'most' critical operational conditions. In case of large forgings, such as gas or steam turbine rotor components, forging flaws can have a significant influence on the structural integrity of the part. During operation these flaws can nucleate into cracks which grow through cyclic loading conditions, e.g. start stop cycles of an engine. Due to the growth of the cracks, these can become so large that the material can no longer tolerate them and a rapid burst occurs. The consequences of such a rapid burst in a large rotor component can be severe and may even lead to fatalities, due to the high amount of stored kinetic energy in such a component. Fig. 1.1 shows a cross sectional cut of a Siemens gas turbine and the principle of the disk based center tie bolt design can be seen. The diameter of the disks is in the order of 1m to 2m and the length of the whole rotor is in the order of 8m to 15m.

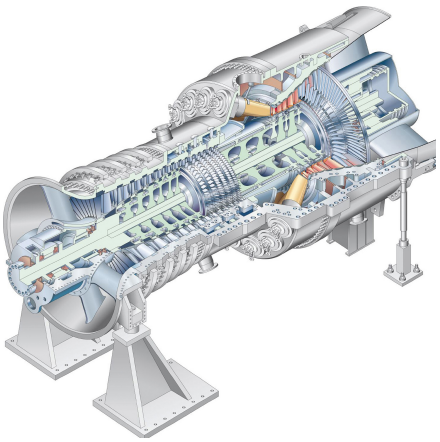

Figure 1.1.: Drawing of a Siemens large gas turbine with cross sectional cut. (with permission from Siemens AG)

In Fig.1.2, the result of such an unfortunate event is shown, which occurred in the 80's in Irsching, where the steam turbine rotor failed due to a rapid burst. Beside this catastrophic failure, several other incidents of this kind all over the world have been reported in the past [36; 37; 41; 42].

Figure 1.2.: Rotor fragment of a 28NiCrMoV 85 steam turbine rotor. The rotor failed by the nucleation and subsequent fatigue crack growth of a small undetected flaw inside the part. The shown fragment weigh about 24 tons. Smaller fragments ($\approx$ 1 ton) had been found up to a distance of a mile from the turbine in Irsching (with permission of Allianz AG [3])

.

The state of the art is to use deterministic fatigue crack growth calculations to estimate the lifetime or the number of cycles to failure of land based gas turbine rotor components. As mentioned before, in deterministic assessments 'worst' case assumptions are made resulting into mostly conservative life estimates [7]. However, it is not possible to quantify the remaining risk [3; 9] (Fig. 1.2).

As the risk at the deterministic life – sometimes called the *safe-life* – is unknown, components with the same risk level might be deemed fit or not fit for service depending on the design and other conditions. Fig.1.3 illustrates different risk levels at deterministic life for different life distributions.

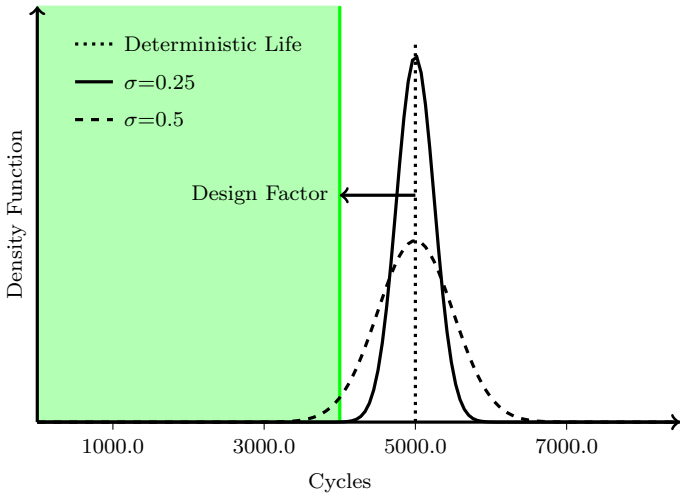

Figure 1.3.: The distribution of the lifetime (as measured in cycles N) depends on the variation of material properties and operating conditions. Deterministic approaches apply minimum material curves and additional safety factors to capture the scatter of material properties and flaw sizes. In general, the risk at the deterministic life (the vertical green line) is not zero and can vary. The green shaded region is called the safe-life region. For simplicity the deterministic approach is shown by one overall safety factor only.

The deterministic approach evaluates the component at the location with the assumed minimum life. Due to the mentioned variations, components can also fail at other locations. A whole component probabilistic approach integrates over the whole component volume and thus delivers an integral evaluation of the component. In Fig.1.4, the stress distribution of two different components with the same maximum stresses are shown. In this simplified picture, both components would have the same deterministic life based on the stress maximum. However, as the component illustrated on the left has a larger volume that is under the influence of high stress, its Probability of Failure (PoF) is larger.

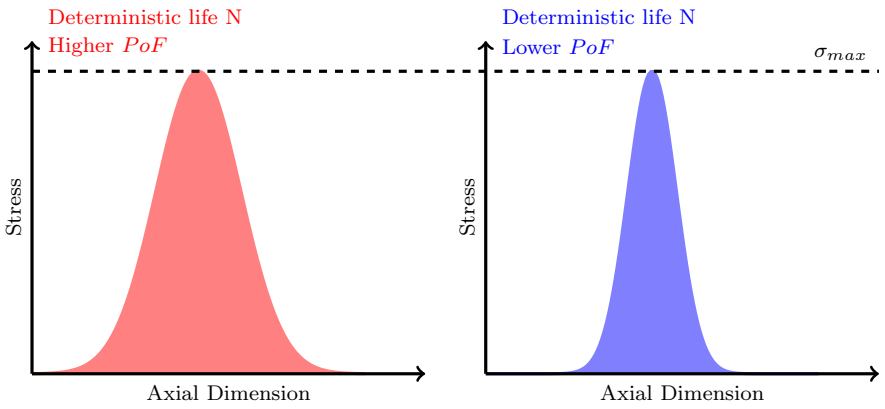

Figure 1.4.: Two components illustrated by the axial stress distribution. In a deterministic evaluation only the 'worst' location, i.e. stress peak σ_{max}, contributes to the evaluation of the part (worst case assumption). In a probabilistic evaluation the whole component can contribute to the overall risk of the component. The larger the highly stressed area is, the larger the *PoF* as the probability of having a flaw in the critical area increases. This can result in different *PoF* for the same deterministic life *N*.

Beside this the result of a deterministic assessment is typically not a true safe life, as the used assessment data are not true worst case values. Typically the material design curves are based on e.g. $1-3\sigma$ values of the distribution fitted to the measured data, thus there is always an intrinsic, not specified risk accepted by the deterministic assessment. If true worst case assumptions are made within the deterministic assessment typically the calculated component life will be zero. A probabilistic assessment allows designers to get an estimator of the remaining life and following the assessment results of different components are better comparable as in the deterministic results.

At the beginning of this development, several probabilistic tools were evaluated for their applicability and availability. The DARWIN tool (Design Assessment of Reliability With INspection, `http://probabilisticfracturemechanics.swri.org`) that is specifically geared towards the probabilistic evaluation of aero-engine rotor disks, has been investigated in depth for its applicability to land-based gas turbines. The following is a list of statements why the decision was made to develop a new tool and methodology (*Prob*abilistic *F*racture *M*echanics (*ProbFM*)) which is geared to the needs of the fracture mechanics assessments of land-based gas turbines:

- **Fracture Mechanics Modeling**
  DARWIN lacks the Failure Assessment Diagram (FAD) failure criterion, an ele-

ment which is implemented in different rotor design philosophies. Furthermore, the fracture toughness is limited to only 40 temperature levels which complicates the description of the typically observed transition from lower to upper shelf regions of some rotor steels [56]. The probabilistic fracture mechanics code *ProbFM* implements the Failure Assessment Diagram, as well as other techniques such as the IRWIN plastic-zone extension (which is also used in current rotor design philosophies) to account for plasticity. The fracture toughness and other material properties are described by a continuous description.

- **Flaw Distribution**
  DARWIN has no automated capability to model radial flaw distributions which are observed in typical land based disk forgings. Furthermore, DARWIN expects as an input the distribution of true flaw sizes, which are not readily available for typical land based disk forgings. *ProbFM* takes into account that the true flaw sizes and distributions are larger and more frequent than the observed Ultrasonic indications in forgings. Furthermore, *ProbFM* takes into account the radial flaw distribution. Usually more flaws tend to be towards the center of large forgings. The shape of the flaw can also vary to include most critical non-circular flaw shapes.

- **Probabilistic Lifing Model**
  DARWIN assumes that the number of cycles to failure is a log-normal random variable. This model is based on the assumption that the only influence comes from the scatter in the crack growth rate, and is log normal distributed [67]. It does not account for the individual scatter of other material properties such as the fracture toughness. In large forgings of land based gas turbines the largest material property influence factor is the variation in fracture toughness, which can not be accounted for in DARWIN. *ProbFM* takes into account all the individual material variability as measured by material tests.

- **Zone-based Probability of Failure Calculation**
  In DARWIN it is necessary to divide the components manually into zones to calculate the *PoF* of a component. For each zone a particular location and crack geometry is chosen to calculate the *PoF* of this zone. To get the *PoF* of the whole component, a volume weighted sum of these zone related *PoF*s is computed. The user has to manually perform a zone refinement including specifications of crack positions and geometries. This process is time consuming and not easy to reproduce, and therefore to some extent depends on the engineer using the tool. To be sure that the result is independent of the chosen zone distribution, a time consuming zone refinement has to be manually performed.

DARWIN is currently developing an automatic zone refinement algorithm, but until the end of 2013 this was not available. *ProbFM* is using a Direct Simulation Monte-Carlo approach [28] that does not require any zoning. This approach requires millions to billions of fracture mechanics calculations to be performed. To achieve this goal numerical algorithms for fast integration and memory access were developed during the course of this project.

For these reasons, and after testing the principal performance of computationally time-critical components of the proposed new approach, a new methodology and its manifestation in the *ProbFM* tool and methodology has been developed. When designing *ProbFM* reproduce ability of results and fast turn-around times that yields reliable and fast answers when needed have been in mind. The fracture mechanics modeling is performed with the same methodologies and solutions as implemented in the standard design tools IWM Verb (`http://www.iwm.fraunhofer.de/profil/vernetzung/projekte-mit-eigener-webseite/verb/`) and NASGRO (`http://www.swri.org/4org/d18/mateng/matint/nasgro/`). The probabilistic modeling and assumptions in this tool is done in a conservative way. Hence, the calculated PoF is an upper bound of the real PoF.

The tool exhibits a high grade of automation and allows for accounting of different operating conditions. Furthermore, the tool is optimized for fast execution as millions to billions of fracture mechanics simulations have to be performed. Therefore, the option of parallel computation has been implemented to speed-up the computation time roughly by the number of CPUs involved.

The presented results are based on real gas turbine components. For reasons of confidentiality the following presented geometries, material properties, $PoFs$ and cycle numbers have been scaled by factors as described in the nomenclature. The Hazard rates and annual risks have been calculated from this scaled PoF. The *ProbFM* methodology has been implemented in the Siemens Gas Turbine design philosophy and successfully applied to assess several different types of engines and rotor components.

Besides the PoF (Fig. 1.5), the methodology gives also insight into the local failure risk and the critical states of components as shown in Fig. 1.6. This figure shows the local failure risk is not constant in the component and it is not only dominated by surface flaws. Especially in the middle of the component, the failure is controlled by a transient state during the start up of the engine. The critical state is controlled by the interaction of the mechanical and thermal stresses and the temperature dependence of the fracture toughness.

One central result of this work is that the probability of failure at the deterministic calculated life of a component can be significantly different for simple components as shown in chapter 6.2 due to the probabilistic size effect. For the examples shown in

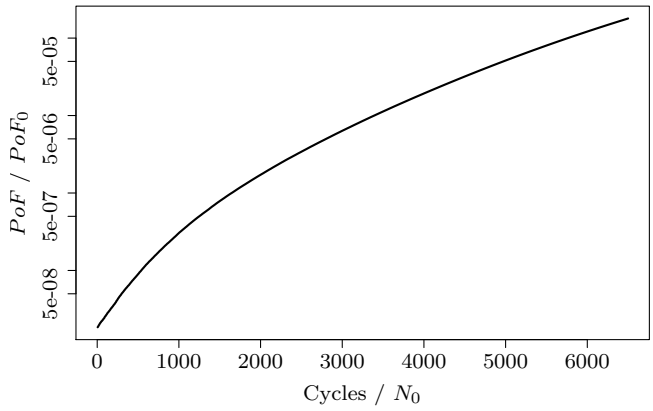

Figure 1.5.: PoF development with increasing number of cycles of an example component.

chapter 6.2 there is a factor of up to 5.47 between the probability of failure at the deterministic life, but this factor can be even larger, for instance if the difference in volume is larger.

It should be clearly stated that the presented methodology calculates the probability of failure induced by the growth and failure of pre-existing forging flaws. In conjunction with other assumptions, or future extensions of the described methodology, it can also be used to quantify a probability of failure based on service induced defects (Low Cycle Fatigue crack initiation and the like). It accounts for material property variation, flaw size variation and their Ultrasonic detectability as has been measured or determined otherwise. It does not account for the element of human errors, such as mislabeling of components, acts of sabotage, earthquakes or other unforeseen events. The calculated probabilities should be treated as such.

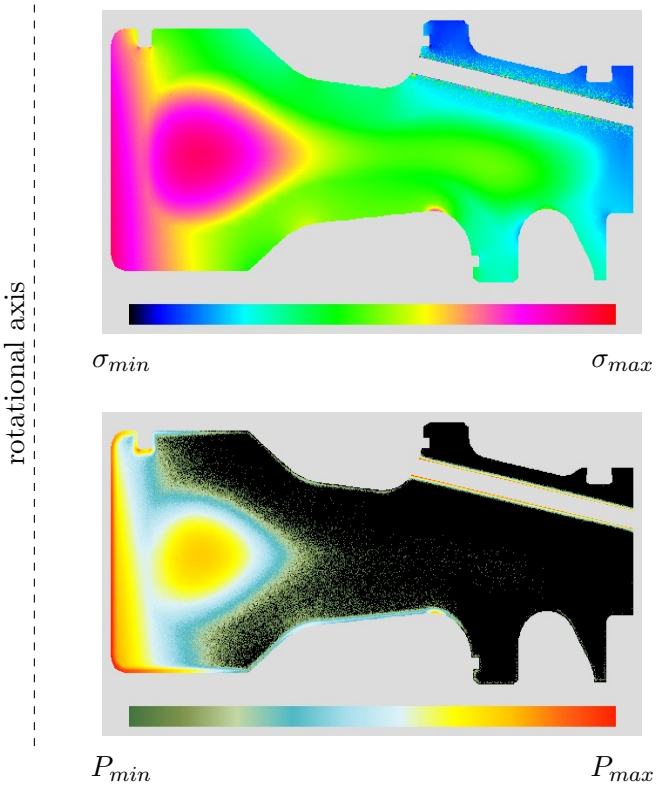

Figure 1.6.: Transient maximum first principle stress and local failure rate map of a gas turbine rotor disk for cold start operation. (Figures not to scale.)

2. Theory

The theory in this probabilistic fracture mechanics framework comprises linear elastic fracture mechanics including failure assessment diagram (FAD) and the Irwin plastic zone extension (IPZE). Additionally probabilistic modeling approaches are used for the material properties, like fracture toughness, crack growth rate and tensile properties, and a probabilistic modeling approach of a non destructive evaluation (NDE) method. The following describes those theoretical assumptions. Most of them are standard literature knowledge, while some had to be extended to our particular needs.

2.1. Fracture Mechanics

In continuum-based fracture mechanics modeling, a crack in a 3-dimensional structure can be described as a 2-dimensional material separation. The crack opening can then be described by three basic modes which are denoted by the roman numbers I-III (Fig. 2.1). All other openings can be described as a linear combination of these three basic modes.

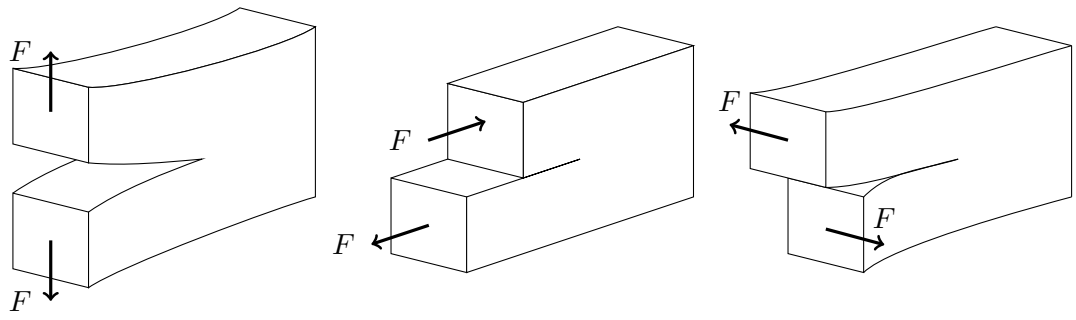

Figure 2.1.: Crack opening modes

Assuming isotropic material properties, mode I cracks exhibit the largest growth rate for a given cyclic stress-field, as all other modes dissipate energy by friction

processes between the two sides of the material [5; 25; 48]. Therefore, many cracks tend to grow into mode I direction independent of their initial orientation. Furthermore, non-mode I crack data is more difficult to measure and therefore very sparely available. Hence, most practical applications assume a mode I crack growth.

It should be noted that the continuum fracture mechanics approach does not account for material inhomogeneities such as grain boundaries, micro-structural gradients, or chemical variations. It is assumed that the length-scales in which changes of these properties take place are small compared to the assessed crack size. For most rotor steels with their relatively small grain sizes compared to the assessed crack sizes, this assumption is easier to justify than for cast parts such as blades, vanes, or most casing related materials.

It should be further noted that the described and applied fracture mechanics approach is a phenomelogical approach that only describes the observed phenomena. It cannot explain or predict relevant mechanisms. Fracture mechanics takes place on much smaller length scales, namely the atomistic and mesoscopic ones, where atoms are separated, dislocations absorb energy and blunt the crack tip on the meso-scale, and nano-voids are nucleated in front of the crack tip. To improve fracture mechanics properties in industrially applied materials, these atomistic mechanisms have to be better understood [16; 27]. Their investigation is subject to other research and beyond the scope of this work.

2.1.1. Linear Elastic Fracture Mechanics

In Linear Elastic Fracture Mechanics (LEFM), it is assumed that the stress field around the crack can be described by means of linear elastic theory. The linear elastic stress field in front of an idealized sharp crack tip (near field) can be approximated by (2.1) [15; 23; 50]. For definition of r and θ see Fig. 2.2.

$$\begin{aligned}
\hat{\sigma}_{xx}(r,\theta) &= \frac{K_I}{\sqrt{2\pi r}} cos\frac{\theta}{2}\left(1 - sin\frac{\theta}{2}sin\frac{3\theta}{2}\right) \\
\hat{\sigma}_{yy}(r,\theta) &= \frac{K_I}{\sqrt{2\pi r}} cos\frac{\theta}{2}\left(1 + sin\frac{\theta}{2}sin\frac{3\theta}{2}\right) \\
\hat{\tau}_{xy}(r,\theta) &= \frac{K_I}{\sqrt{2\pi r}} cos\frac{\theta}{2}sin\frac{\theta}{2}cos\frac{3\theta}{2}
\end{aligned} \tag{2.1}$$

The factor K_I is called the mode I stress intensity and defines the magnitude of the stress field within the framework of linear elasticity. It is defined by the applied mode I stress σ_I (acting in y-direction), the crack length a and the geometry factor Y (2.2).

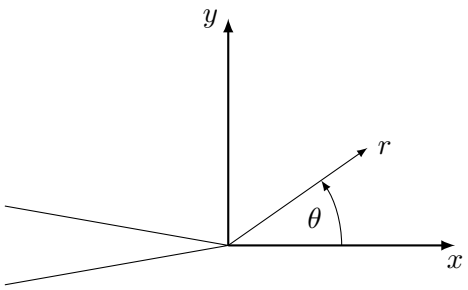

Figure 2.2.: Coordinate system with crack tip in the center at (0,0), crack propagation direction along x-axis.

$$K_I = \sigma_I \sqrt{\pi\, a}\, Y \tag{2.2}$$

For idealized elliptic embedded and semi-ellipticial surface cracks, Y is in general a function of the half-axis ratio $\frac{a}{c}$ and optional parameters to describe the crack embedding geometry (see Figure 2.5). For most rotor applications the crack embedding geometry is relatively large compared to the crack size. However, there might be circumstances where the crack embedding geometry might be of importance and can not be assumed to be large. For these cases, *ProbFM* offers a finite crack embedding geometry correction that will be discussed in 2.3.4.

Within the framework of linear elastic fracture mechanics, it is assumed that the crack growth and its stability can be described by the stress intensity factor alone. This is a phenomenological observation and has some theoretical motivation as the stress-field near the crack tip can be solely described by the stress intensity and does not need the crack size and applied stress separate. One can further argue that possible crack growth phenomena such as void nucleation in front of the crack tip depends only on the stress field and thus on the stress intensity [49]. It should be noted that for large applied stresses the concept of linear elastic fracture mechanics might be challenged. Here, the transferability of cyclic test data under low applied stress should always be investigated. Within this project, such high stress experiments with stresses up to 800 MPa have been performed to investigate these questions (Chapter A.5).

2.1.2. Irwin Plastic Zone Extension

The formula for the stress field in front of a crack tip is given by equation (2.1) and in equation (2.2) the stress intensity is introduced. Equation (2.1) exhibits a singularity

at the crack tip of the order of $\frac{1}{\sqrt{r}}$. This singularity results in infinite stresses at the crack tip which causes a plastic zone near the crack tip as the material yields at high stresses.

To account for this change in material behavior at the crack tip, Irwin [24] proposed an effective crack length a_{eff} [5, chap. 2.8.1]. In the crack plane ($\phi = 0$) the normal stress $\hat{\sigma}_{yy}$ is given by equation (2.1). A first estimate for the crack length correction Δa can be developed by the assumption that plastic behavior occurs if the stress is bigger than a yield criterion σ_{YS}. With $\hat{\sigma}_{yy} = \sigma_{YS}$ and $\phi = 0$, equation (2.1) can be reshaped to (2.3).

$$r_y = \frac{1}{2\pi} \left(\frac{K_I}{\sigma_{YS}} \right)^2 \tag{2.3}$$

Without strain hardening, the normal stress from the crack tip up to r_y is limited by yielding to σ_{YS} as shown in Fig. 2.3.

The simple assumption above ignores the energy conservation as the stored elastic energy (shaded area in Fig. 2.3) has to be redistributed due to yielding. To account for this, Irwin suggested the following correction (2.4) which increases the plastic zone size.

$$\sigma_{YS}\, r_p = \int_0^{r_y} \sigma_{yy} dr \tag{2.4}$$

Solving equation (2.4) for r_p results into (2.5).

$$r_p = \frac{1}{\pi} \left(\frac{K_I}{\sigma_{YS}} \right)^2 \tag{2.5}$$

The plastic zone of the second correction is twice as large as the of the first correction $r_p = 2\, r_y$.

Irwin defined an effective crack length a_{eff} to account for the larger plastic zone. The effective crack length is defined by equation (2.6).

$$a_{eff} = a + r_y \tag{2.6}$$

In the derivation of the plastic zone size, plane stress conditions have been assumed. If plane strain conditions are acting, the plastic zone size is reduced by a factor of 3. For large gas turbine rotor forgings in general, plane strain conditions can be assumed as the cracks are much smaller than the dimensions of the component.

The effective crack length a_{eff} depends on the stress intensity. Therefore, the stress intensity and the crack length usually have to be calculated in a time consuming, iterative process.

In the case of elliptical or semi elliptical cracks an approximated closed form of the

crack length correction is available (2.7) [5, chap. 2.8.1].

$$
\begin{aligned}
K_{eff} &= \sigma\sqrt{\frac{\pi a}{Q_{eff}}}\left(sin^2\left(\phi\right) + \left(\frac{a}{c}\right)^2 cos^2\left(\phi\right)\right)^{\frac{1}{4}} \\
Q_{eff_{emb}} &= Q - 0.212\left(\frac{\sigma}{\sigma_{YS}}\right)^2 \\
Q &= 1 + 1.464\left(\frac{a}{c}\right)^2 \\
Q_{eff_s} &= \left(Q - 0.212\left(\frac{\sigma}{\sigma_{YS}}\right)^2\right)\lambda_s \\
\lambda_s &= \left(1.13 - 0.09\left(\frac{a}{c}\right)\right)\left(1 + 0.1\left(1 - sin\phi\right)^2\right)
\end{aligned}
\tag{2.7}
$$

In case a special geometry factor solution should be used, Q has to be substituted (2.8) by the corresponding geometry factor.

$$
Q = \frac{1}{Y^2} \tag{2.8}
$$

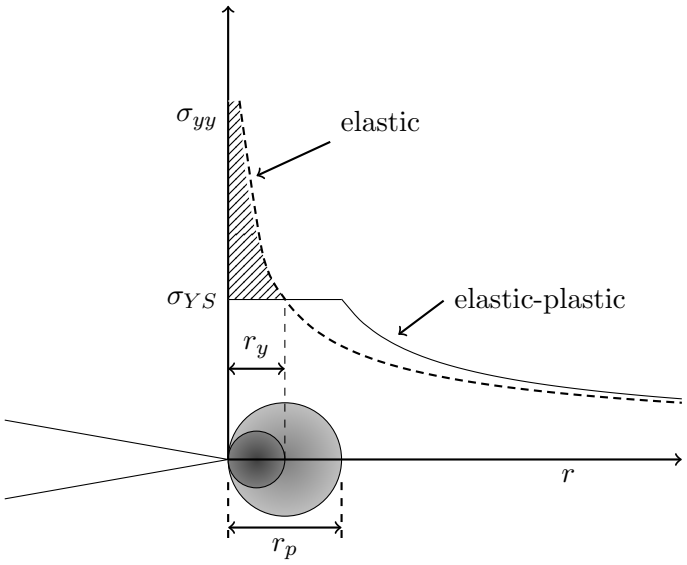

Figure 2.3.: Irwin plastic zone extension

In [5, chap. 2.8.3] a comparison of the linear elastic fracture mechanics and the Irwin plastic zone extension model is shown. Up to a ratio of approximately $\frac{\sigma}{\sigma_{YS}} = 0.5$,

the linear elastic fracture mechanics and the Irwin plastic zone extension predict similar stress intensities. For larger ratios, the stress intensities predicted by the linear elastic fracture mechanics and Irwin plastic zone extension diverge, where the Irwin plastic zone extension predicts larger stress intensities than the linear elastic fracture mechanics. Due to this, the Irwin plastic zone extension model predicts an increased crack growth at high stress levels compared to the linear elastic fracture mechanics.

2.2. Crack Geometries

In general, no solutions of the geometry factor Y are available for an arbitrary component, crack geometry and loading condition. Commonly, the geometry of the component is approximated by a simple geometry, for example a plate, bar or tube (Figure 2.4). The crack is then in general approximated by elliptic or rectangular shapes. Many geometry factors for such generic cases are available in form of approximate functions and tables [6; 35; 46].

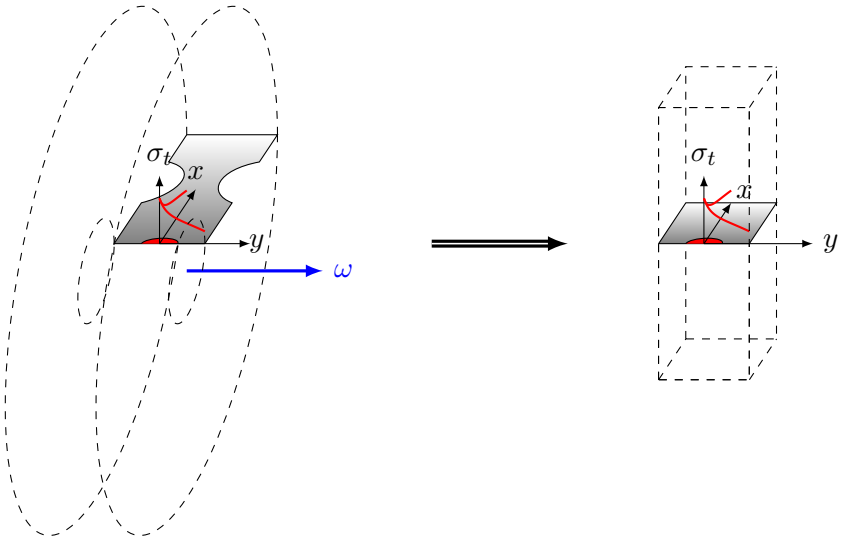

Figure 2.4.: Modeling a semi-elliptical surface crack in the hub of a rotor disk by a simplified crack model in a rectangular plate.

Two types of crack geometries, elliptic embedded and semi elliptic surface, are

implemented for plates in *ProbFM*. The plate size can be assumed to be infinite in *ProbFM*. Typical critical crack sizes in stationary gas turbine rotors are on the order of a few millimeters and the component dimensions are from several centimeters up to a meter. Therefore, this is a reasonable approximation. However, an automatic plate size generator has been implemented, and for the large rotor forgings geometries that have been considered, no significant change in the results has been observed in most cases. By default in our design the automated plate size generator is used.

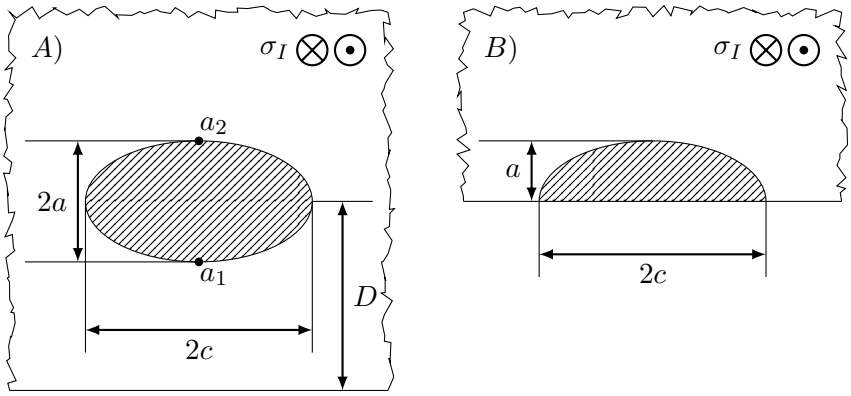

Figure 2.5.: A) Elliptic embedded and B) semi elliptic surface crack loaded with mode I stress.

Furthermore, it is conservatively assumed that the cracks are oriented perpendicular to the transient maximum of the first principal stress of the start stop cycle. For most of the relevant practical applications, this is a reasonable simplification as cracks tend to grow in mode I even if they are not oriented perpendicular at the beginning.

2.3. Stress Intensity Factors

Currently six different geometry factor solutions are available in *ProbFM*, three elliptic embedded and three semi elliptic surface cracks. The general structure of the solutions is shown in (2.9) and (2.10).

$$K_{I@a} = \left\{ \sigma \, Y_{m@a}\left(\frac{a}{c}\right) \; F_{m@a}\left(\frac{a}{c}, \frac{D}{a}\right) + \left[\frac{\delta\sigma}{\delta r}\right]_{max} 2a \, Y_{g@a}\left(\frac{a}{c}\right) \; F_{g@a}\left(\frac{a}{c}, \frac{D}{a}\right) \right\} \sqrt{\pi \, a} \tag{2.9}$$

$$K_{I@c} = \sigma \, Y_{m@c}\left(\frac{a}{c}\right) \; F_{m@c}\left(\frac{a}{c}, \frac{D}{a}\right) \sqrt{\pi \, a} \tag{2.10}$$

IWM VERB and NASGRO distinguish between the crack tips a_1 and a_2 (as shown in figure Fig. 2.5) if surface effects or stress gradients influence the stress intensity. To increase the calculation speed in *ProbFM*, it is conservatively assumed that the a axis is oriented parallel to the stress gradient and perpendicular to the next component surface.

For embedded cracks, it is assumed that the stress gradient is positive if approaching to the next component surface. Furthermore, *ProbFM* only calculates the stress intensity at the half axis points which deliver the highest stress intensity and uses this for both crack tips of a half axis. Thus, if a stress gradient is accounted for, it always decreases the number of cycles to failure of a crack compared to a pure membrane assessment and increases the PoF. For semi elliptic surface cracks no stress gradient assessment is done at all. In order to reduce conservatism the latter can be accounted for in the future.

The implemented geometry factor solutions are based on textbooks [25] or manuals [57; 60]. The geometry factors are imported to *ProbFM* as equidistant tables $Y\left(\frac{a}{c}\right)$ and $F\left(\frac{a}{c}, \frac{a}{D}\right)$. As mentioned in Section 2.2, the substitute plates can be assumed to be infinite or a manual plate size correction factor can be used to account for small plates, or the previously named auto plate function can be utilized as well.

The implemented SIF solutions match almost exactly IWM VERB or NASGRO. Some minor corrections are not captured by the described SIF structure ((2.9) and (2.10)). This has only a small or even no effect on the calculated failure cycle number as shown in chapter A.

In general, each SIF solution which can be written as shown in (2.9) and (2.10) can be used, as the SIF solution is read in to *ProbFM* as a table.

2.3.1. Textbook Stress Intensity Factor Solution

The textbook solutions for the elliptic embedded and semi-elliptic surface crack implemented in *ProbFM* are taken from [25, p.52ff] [39; 46]. Where $\phi = \frac{\pi}{2}$ defines the crack tip at a and $\phi = 0$ defines the crack tip at c. The correction factor C is given in table 2.1.

		C			
		$\frac{a}{t}$			
$\frac{a}{c}$	ϕ	0.2	0.4	0.6	0.8
0.2	0	0.617	0.724	0.899	1.190
	$\pi/4$	0.990	1.122	1.384	1.657
	$\pi/2$	1.173	1.359	1.642	1.851
0.4	0	0.767	0.896	1.080	1.318
	$\pi/4$	0.998	1.075	1.247	1.374
	$\pi/2$	1.138	1.225	1.370	1.447
0.6	0	0.916	1.015	1.172	1.353
	$\pi/4$	1.024	1.062	1.182	1.243
	$\pi/2$	1.110	1.145	1.230	1.264
1.0	0	1.174	1.229	1.355	1.464
	$\pi/4$	1.067	1.104	1.181	1.193
	$\pi/2$	1.049	1.062	1.107	1.112

Table 2.1.: Surface semi elliptic SIF correction factor C

$$K_{I\,emb} = \frac{\sigma\sqrt{\pi\,a}}{\frac{3\pi}{8} + \frac{\pi a^2}{8c^2}} \left(sin^2\phi + \frac{a^2}{c^2} cos^2\phi \right)^{\frac{1}{4}} \tag{2.11}$$

$$K_{I\,sur} = C\,\frac{\sigma\sqrt{\pi\,a}}{\frac{3\pi}{8} + \frac{\pi a^2}{8c^2}} \left(sin^2\phi + \frac{a^2}{c^2} cos^2\phi \right)^{\frac{1}{4}} \tag{2.12}$$

2.3.2. IWM VERB Stress Intensity Factor Solution

The implemented IWM Verb solution for an embedded elliptic crack is given by [60, chap. 3.6.1] and [59]. The semi-elliptic surface crack solution is provided in [60, chap. 3.3.1] and [65]. The Y_m part of this SIF solutions is shown in Figures 2.6 and 2.7 with $\phi(a) = \pi/2$ and $\phi(c) = 0$.

2.3.3. NASGRO Stress Intensity Factor Solutions

The Y_m part of the NASGRO SIF solutions are also shown in Figures 2.6 and 2.7 with $\phi(a) = \pi/2$ and $\phi(c) = 0$. Apparently, there are no significant differences between these two SIF solutions if no stress gradients or surface effects are accounted for.

In addition Figure 2.8 shows the factor by which the stress intensity increases of an elliptic embedded crack due to the presence of a free surface.

The embedded crack solution is based on the EC05 solution from NASGRO [57, Appendix C3] [40], and the semi elliptic surface crack solution is based on the SC17 solution from NASGRO [57, Appendix C4] [14; 55]

The crack assessment in NASGRO uses two additional modifications of the SIF if the crack intersects a surface and the changed stress conditions (plane strain <-> plane stress) at this crack tip. The stress intensity at the surface is modified by the β correction function (2.13) which has been proposed by Newman and Raju [38] to account for crack closure effects at the surface during crack growth.

$$\beta = 0.9 + 0.2\,R^2 - 0.1\,R^4 \tag{2.13}$$

Since the crack state at the surface is more like plane stress than the plane strain as assumed in the interior of the component [50, chapter 5.2], the fracture toughness is increased. Within the used NASGRO SIF solution the fracture toughness at the surface is independent of the stress ratio R and kept constant as shown in (2.14).

$$K_c = 1.1\,K_{Ic} \tag{2.14}$$

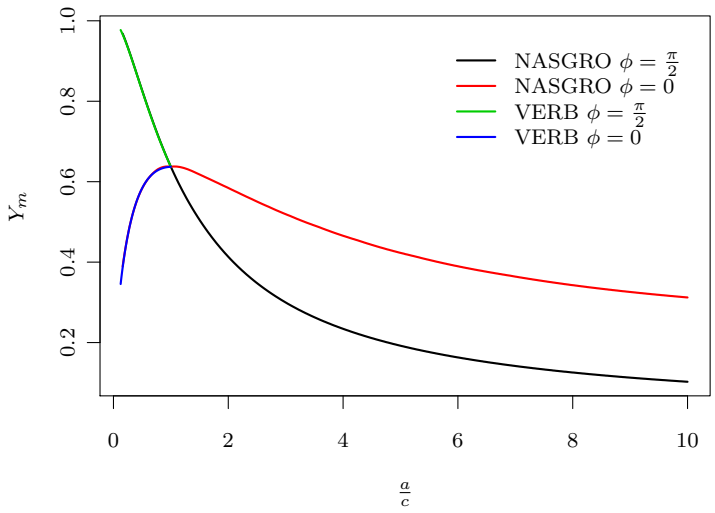

Figure 2.6.: IWM VERB and NASGRO SIF solutions for embedded elliptic cracks with pure tension stress

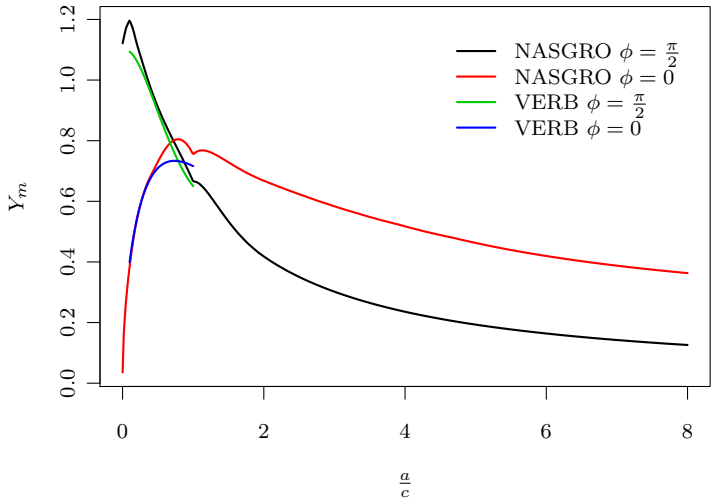

Figure 2.7.: IWM VERB and NASGRO SIF solutions for surface semi elliptic cracks with pure tension stress

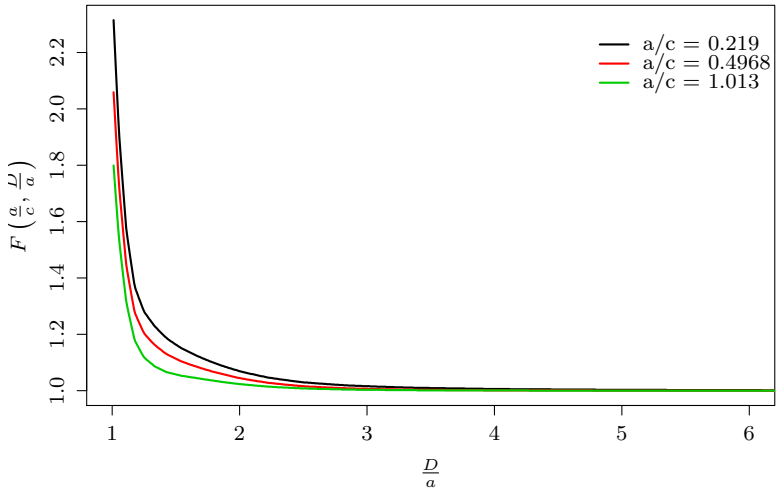

Figure 2.8.: NASGRO SIF solutions increase factor for embedded elliptic cracks with pure tension stress close to a surface

2.3.4. Finite Plate Size Correction

In case component dimensions are not much larger than the crack dimensions, the finite dimension has to be accounted for in the plate solution for the SIF calculation. In this case, a finite plate size correction can be used. The following equations describe a correction factor for the embedded elliptic (2.16) [59; 60] crack and for the semi elliptic crack (2.15) [40; 60].

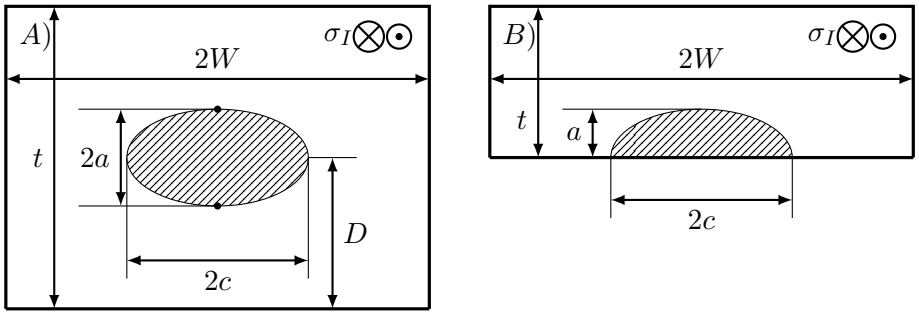

Figure 2.9.: A) Elliptic embedded and B) semi elliptic surface crack plate size definition loaded with mode I stress.

$$f_{w\,emb} = \sqrt{sec\left(\frac{\pi\, c}{2\, W}\sqrt{\frac{2\, a}{t}}\right)} \tag{2.15}$$

$$f_{w\,sur} = \sqrt{sec\left(\frac{\pi\, c}{2\, W}\sqrt{\frac{a}{t}}\right)} \tag{2.16}$$

2.4. Failure Criteria

Within this framework two different failure criteria have been implemented as follows.

2.4.1. Fracture Toughness

Components are assumed to fail if the stress intensity K associated with a crack reaches a critical value. Assuming mode I, plane strain conditions, and brittle failure, this value is the so called mode I fracture toughness K_{Ic}. The fracture toughness is a temperature dependent material property and shows significant scatter (Fig. 2.10). Many steels exhibit a strong temperature dependence due to a brittle to ductile transition. For low temperatures, dislocation movement is limited, slip bands are not activated and the material shows brittle failure associated with a low fracture toughness (often times referred to as the *lower shelf* value). At higher temperatures, modes of plasticity get activated and the material shows in general a larger fracture toughness (*upper shelf*). At temperatures where a ductile failure mechanism is observed, the K_{Ic} alone is not a valid failure criterion. The reason for this is that K_{Ic} is only valid in the linear elastic fracture mechanics with small scale yielding. A possible failure criterion for the ductile failure can be expressed by so-called J-Integral method that takes into account non-linearities by integrating along a path around the crack tip [47].

Furthermore, under the assumption of plane strain conditions a K_{JIc} value can be calculated from the measured J_c value (2.17) [11].

$$K_{JIc} = \sqrt{\frac{J_c\, E}{1-\nu^2}} \tag{2.17}$$

The K_{JIc} value is used as the fracture toughness K_{Ic}.

2.4.2. Failure Assessment Diagram

To account for plasticity effects in the failure criterion, the Failure Assessment Diagram (FAD) is implemented in *ProbFM*. The utilized assessment curve (2.20) is the basic level assessment from SINTAP [1]. If the assessment point (points A and B in Fig. 2.11) is below the assessment curve, no failure is predicted, otherwise a failure is assumed. The assessment curve and its parameters are described by equations (2.18) - (2.20).

$$K_r = \frac{K_I}{K_{Ic}} \tag{2.18}$$

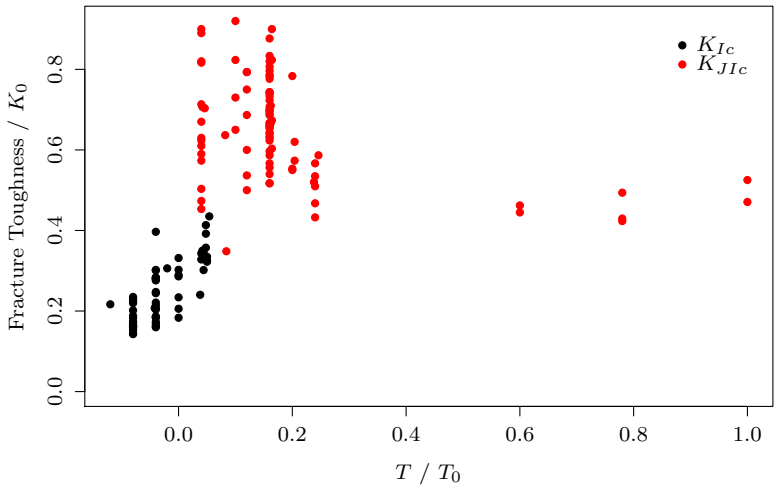

Figure 2.10.: Measured K_{Ic} and K_{JIc} values of a high alloy high strength rotor steel (12%Cr, CostE, Siemens AG data).

$$L_r = \frac{\sigma}{\sigma_f} \tag{2.19}$$

$$f(L_r) = \begin{cases} \left(1 + \frac{L_r^2}{2}\right)^{-\frac{1}{2}} \left[0.3 + 0.7e^{-\mu L_r^6}\right], & 0 \le L_r \le 1 \\ 1.5^{-\frac{1}{2}} \left[0.3 + 0.7e^{-\mu}\right] L_r^{\frac{N-1}{2N}}, & 1 < L_r \le L_{r\,max} \end{cases} \tag{2.20}$$

$$\mu = min\left(0.001\frac{E}{\sigma_{YS}};\ 0.6\right)$$

$$N = 0.3\left(1 - \frac{\sigma_{YS}}{\sigma_{UT}}\right)$$

$$L_{r\,max} = \frac{\sigma_{YS} + \sigma_{UT}}{2\sigma_{YS}}$$

The failure assessment curve $f(L_r)$ in (2.20) defines an area where no failure is expected. The safe region is shown by the gray area in Fig. 2.11. As long as the assessment point stays within this area no failure is expected. The assessment point is defined by K_r (2.18) and the load parameter L_r (2.19). The load parameter is the

ratio of the applied stress σ to the stress which would cause a plastic collapse of the component σ_f.

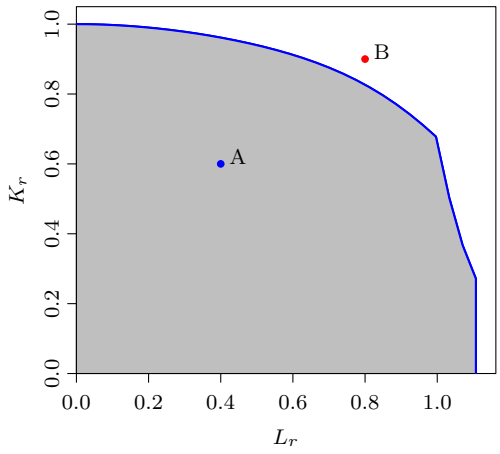

Figure 2.11.: Failure assessment diagram example: (A) No Failure expected
(B) Failure expected
Instantaneous component failure is expected if the load is larger than the flow stress

In *ProbFM*, multiple ways to estimate the L_r parameter are implemented. In general, the influence of the crack size on the load parameter L_r can be neglected for large forged gas turbine components as the critical crack size is much smaller than the component size, i.e. $A_{crit} \ll A_{comp}$. Hence, the crack has no influence on the overall stress field of the component.

The first approach is based on the assumption that the local plastification reduces the local fracture toughness. This approach yields usually extremely conservative estimates at low values of the PoF as it does not account for the support effect of the reaming component for the high stressed regions. On the other side the tails of the PoF is populated by the high stress states in the component. This approach basically evaluates a local yielding with no support of the surrounding component. It should not be used for design purposes, as it yields extremely conservative results.

$$L_r = \frac{\sigma\left(x, y, z, LS\right)}{\sigma_{YS}\left(T\right)} \tag{2.21}$$

The second approach calculates one load parameter for the entire component. Within this approach, the local plastification is integrated over the total volume – or a user-specified sub-volume – of the component Ω (2.22).

$$L_r = \frac{\int\limits_{\Omega} \frac{\sigma(x,y,z,LS)}{\sigma_{YS}(T)} dx\, dy\, dz}{\Omega} \tag{2.22}$$

In a third approach an L_r parameter for the entire component – for instance if this has been calculated by means of FEA –can be defined by the user. The default calculation mode uses the total volume of the component for the calculation of L_r. As the integration requires stress and yield stress values – and for most practical applications a transient FEA is processed – *ProbFM* offers two modes (T=Temperature, LS=Load Step) for selecting the stress and temperature values:

- mode 1 (default): $\sigma_{YS}(T)$ and $\sigma\,(x, y, z, LS)$ are taken at the transient load step (LS), which is critical in terms of the fracture toughness.
- mode 2: $\sigma_{YS}(T)$ is taken at the maximum temperature during the cycle, σ is set to the largest stress during the cycle. This yields very conservative results.

A true evaluation of L_r can be performed by a non-linear FEA analysis of the component and the revealed L_r can be used within $ProbFM$.

2.5. Fatigue Crack Growth Calculation

The crack growth rate in *ProbFM* is described as a function of the stress intensity range ΔK, the stress ratio R and the Temperature T (2.23).

$$\frac{da}{dN} = f\,(\Delta K,\ R,\ T) \tag{2.23}$$

$$\Delta K = \Delta\sigma\sqrt{\pi a}\, Y \tag{2.24}$$

Historically, a power law between the stress intensity range and the crack growth rate has been proposed, it is known as the Paris-law (2.25) [45].

$$\frac{da}{dN} = C\,\Delta K^m \tag{2.25}$$

Many other crack growth rate models modify and add further complexity to the above Paris-equation. Most of them still have an intermediate range that exhibits power-law behavior. In order to capture the variety of these crack growth models, *ProbFM* is able to read in three-dimensional high-performance numerical look-up tables for the description of the crack growth rate. This allows an external code to precalculate the tables with no restrictions on the analytical form of the model. Another advantage is the speed at which these tables can be looked-up during calculations.

Since the stress intensity range ΔK is a function of the crack size a, equation (2.23) becomes an ordinary differential equation. In general, it is not possible to get an analytic solution for this ordinary differential equation. Therefore, the crack size after a number of cycles has to be numerically integrated. Simple Euler integration schemes could be used for the integration, however integration step size would have to be very small in order to obtain acceptable numerical errors. More sophisticated higher order integration schemes such as Runge-Kutta 4th order [51] schemes ought to be applied instead.

$$\tilde{a}_{n+1} = \tilde{a}_n + \frac{d\tilde{a}_1}{6} + \frac{d\tilde{a}_2}{3} + \frac{d\tilde{a}_3}{3} + \frac{d\tilde{a}_4}{6} \tag{2.26}$$

$$d\tilde{a}_1 = dN f\left(\Delta K_n\right) \tag{2.27}$$

$$d\tilde{a}_2 = dN f\left(\Delta K_n + \frac{1}{2}\frac{\Delta K_n}{2\tilde{a}_n} d\tilde{a}_1\right) \tag{2.28}$$

$$d\tilde{a}_3 = dN f\left(\Delta K_n + \frac{1}{2}\frac{\Delta K_n}{2\tilde{a}_n} d\tilde{a}_2\right) \tag{2.29}$$

$$d\tilde{a}_4 = dN f\left(\Delta K_n + \frac{\Delta K_n}{2\tilde{a}_n} d\tilde{a}_3\right) \tag{2.30}$$

In *ProbFM*, a modified Runge Kutta approach (2.26) - (2.30) is used as published in [4]. This approach has the advantage that for typical conditions in gas turbine disks, the crack growth is overestimated even for very large integration step sizes. Thus the calculated PoF becomes an conservative estimate of the real PoF. For small integration step sizes, the scheme converges to the correct result. The aim is the assessment of very small *PoFs*, in which case only very few of the simulated cracks will have caused failures of the component. The modified integration scheme is used to pre-screen the simulated flaws with large integration steps for flaws which for sure will not fail during a given number of cycles. Hence the number of cracks which have to be calculated with a small integration step size to resolve accurate results is significantly reduced, i.e. the calculation time for calculating the PoF is reduced.

2.6. Crack Transition

During a component's life some embedded cracks which are at the beginning near the surface can evolve to surface flaws due to crack growth. *ProbFM* contains three different models to account for crack transitions from embedded to surface cracks. All implemented models are assumed to be conservative if used appropriately. Currently, there are very few experimental validations for crack transition available, especially

for elliptical embedded to semi elliptic embedded cracks.

In all models it is assumed, that the a axis is orthogonal to the next component surface.

2.6.1. Surface Area Model

This model does not account for crack transitions due the fatigue crack growth. Instead of a crack transition during the lifetime the user has to define a surface thickness D wherein all cracks start from the beginning to grow as a surface crack. Therefore, all cracks which are not within this surface area are embedded cracks. If a crack lies within the surface thickness, the crack immediately turns into a surface crack.

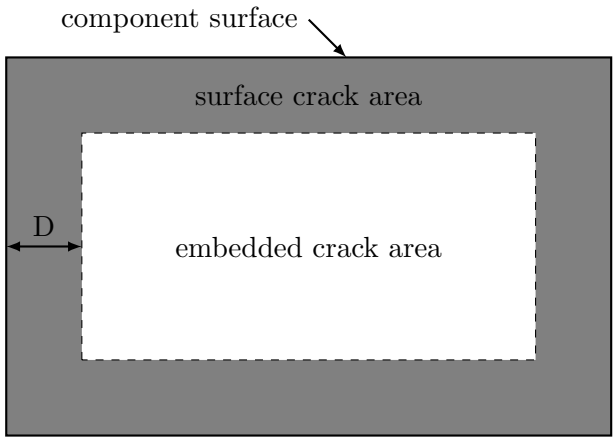

Figure 2.12.: Surface area model for crack transition.

2.6.2. Constant Crack Area Model

The second model is based on a NASGRO crack transition model [57, Appendix D, EC02-SC17]. If $a \geq 0.9D$ (Fig. 2.13) the elliptical embedded crack becomes a semi elliptical crack with the same area A.

$$\begin{aligned} a &\geq 0.9\, D \Rightarrow \text{Transition} \\ a' &= 2a \\ c' &= c \\ A' &= A \end{aligned} \tag{2.31}$$

2.6.3. Increased Crack Area Model

The third crack transition model is the EC05 to SC17 transition model from NASGRO [57, Appendix D]. The transition occurs if $a \geq 0.99D$. The resulting surface crack has an area A which is approximately 1.14 times the area of the elliptic embedded flaw.

(a) Embedded elliptical crack (b) Semi-elliptical surface crack

Figure 2.13.: Embedded elliptical crack to surface semi-elliptical crack

$$
\begin{aligned}
& a \geq 0.99\, D \Rightarrow \text{Transition} \\
& A' = \frac{\pi\, a\, c}{2} + 2\, c\, D \\
& a' = a + D \\
& c' = \frac{2\, A}{\pi\, a'} = c \left(\frac{1}{2} + \frac{2}{\pi} \right) \approx 1.13662\, c \\
& A' \approx 1.14\, A
\end{aligned}
\tag{2.32}
$$

2.7. Probabilistic Material Modeling

As mentioned before, the PoF of interest is such a small number, so that the input parameters like the material properties have to be described by appropriate distributions. The description of the lower tails of the distribution can have a significant impact on the overall result. In the following, general modeling assumptions and the explicit modeling of the material properties are described.

2.7.1. Maximum Likelihood Estimator

In deterministic mechanical engineering approaches it is common to use least square fits and normal distributions to describe material data and derive deterministic design curves. In a probabilistic approach, the description of material data by a normal

distribution is oftentimes not advisable as the normal distribution is not limited to positive values as it is often the case for material properties. Furthermore, in a probabilistic assessment, it is essential to describe the material data and the scatter of the residuals as good as possible as in general no safety or design factors are applied.

The well known least square fit contains the intrinsic assumption that the residuals are normally distributed. To account for other types of distributions during the fitting process, the more general Maximum-Likelihood approach can be used (2.33) [22; 58]. It is computationally easier to calculate a sum rather than a product and most optimization algorithms minimize a given target function. Thus, the negative logarithm of the likelihood is used for optimization (2.34).

$$L\left(\theta \mid x_1, ..., x_n\right) = \prod_{i=1}^{N} f\left(\theta; x_i\right) \tag{2.33}$$

$$-\,l\left(\theta \mid x_1, ..., x_n\right) = -ln\left(L\left(\theta \mid x_1, ..., x_n\right)\right) = -\sum_{i=1}^{N} ln\left(f\left(\theta; x_i\right)\right) \tag{2.34}$$

In this case, f is the probability density function (PDF) which describes the relative likelihood for a given random variable to take a given value. The cumulative distribution function (CDF) F describes the probability that a random variable takes a value equal or smaller than a given value and is defined as (2.35).

$$F\left(x\right) = \int_{\infty}^{x} f(z)dz \tag{2.35}$$

The estimator $\hat{F}$ of the CDF is called the empirical cumulative distribution function (ECDF) and is defined by (2.36).

$$\hat{F}\left(x\right) = \frac{1}{n}\sum_{i=1}^{n} Ind\left(x, x_i\right) \text{ with } Ind(x,t) = \begin{cases} 1 & \text{if } x \leq t \\ 0 & \text{if } x > t \end{cases} \tag{2.36}$$

Where n is the number of residuals.

Appropriate distributions are Lognormal, Weibull, Gamma or other distributions which are defined from 0 to $+\infty$. The corresponding density functions are given by (2.37) to (2.39).

$$f_{lnorm}\left(x\right) = \frac{1}{\sqrt{2\,\pi}\,\sigma\,x}\, e^{-\frac{(ln(x)-\mu)^2}{2\,\sigma^2}} \tag{2.37}$$

$$f_{weib}\left(x\right) = \frac{a}{b}\,\left(\frac{x}{b}\right)^{a-1}\, e^{-\left(\frac{x}{b}\right)^a} \tag{2.38}$$

$$f_{gamma}(x) = \frac{1}{s^a \, \Gamma(a)} \, x^{a-1} \, e^{-\frac{x}{s}} \tag{2.39}$$

$$\Gamma(x) = \int_0^{+\infty} t^{x-1} \, e^{-t} dt \tag{2.40}$$

As in general the distribution type of the residuals is unknown, it has to be decided which distribution describes the residuals best. In order to do so, one can make use of so called hypothesis tests such as the Kolmogorov-Smirnov (KS) or Anderson-Darling (AD) test [22; 58]. The AD test statistics A_n gives a larger weight to the tails of the distribution as compared to the KS test statistics D_n as can be seen by equations (2.41) and (2.42).

$$D_n = sup \left| F(x) - F_n(x) \right| \tag{2.41}$$

$$A_n = n \int_{-\infty}^{\infty} \frac{\left(F_n(x) - F(x)\right)^2}{\left[F(x)\left(1 - F(x)\right)\right]} dF(x) \tag{2.42}$$

The calculation of the P-values for the test statistics A_n and D_n is described for instance in [34] and [33]. The P-value describes the probability of obtaining a test statistic at least as extreme as the observed one.

Other means to judge the goodness of fit are graphical assessments such as so-called Quantile-Quantile- (QQ) or Probability-Probability- (PP) plots [58]. They show in a graphical manner how good a distribution fits to the measured data. In the QQ-plot the empirical quantiles are plotted vs. the analytic expected quantiles and in the PP-plot the same is done for the probabilities. Just as the AD test, the QQ-plot pronounces the deviations in the tails compared to the PP-plot.

At this point it should be mentioned that all these hypothesis tests do not account for any possibly existing temperature dependence of the residual shape and scatter. Also, the Maximum-Likelihood approach only searches for the most probable parameters for the assumed functional model. It only accounts for a variable scatter if this is explicitly modeled. Thus the described tests are only a first step to identify an appropriate distribution to describe the residuals. In a second step, it has to be checked if the found distribution describes the residuals at all temperatures.

2.7.2. Modeling Assumptions

For most material properties, only a limited amount of data is available. *ProbFM* conservatively assumes that the relative scatter of the data is constant and not a function of the temperature or other variable parameters. With this approach, scatter from

one region — for instance high temperature regions, or transition regions — will be transfered to all other regions. As *ProbFM* calculates low probabilities, every additional scatter increases the failure probability. Therefore, the approach overestimates the probability of failure.

In general no explicit type of the relative residual distribution $\langle \epsilon_r \rangle$ is assumed for the simulation. Only the definition of the residuals has to be done according to the following equation (2.43).

$$\langle \epsilon_r \rangle = \frac{\langle A(\Theta) \rangle}{P(\Theta)} - 1 \tag{2.43}$$

$\langle A(\Theta) \rangle$ denotes the actual value distribution, $P(\Theta)$ is the predicted value and $\langle \epsilon_r \rangle$ describes the residual distribution.

For each input distribution, the appropriate distribution type can be chosen and fitted by the methods described in section 2.7.1. The dependence of the material properties on different parameters Θ, e.g. temperature, stress intensity, stress ratio, are modeled for instance by a mean, median or other scaling value curve $P(\Theta)$. The material properties for the simulation are drawn from the distribution $\langle A(\Theta) \rangle$ which is given by equation (2.44)

$$\langle A(\Theta) \rangle = P(\Theta)\ (1 + \langle \epsilon_r \rangle) \tag{2.44}$$

2.7.3. Fracture Toughness Modeling

The details of the fracture toughness model used within *ProbFM* can not be described here as the modeling approach is part of a Siemens AG trade secret. In general the modeling approach describes a global fracture toughness value which is in parts similar to the Wallin Master curve approach [64]. The modeling approach accounts for different scatter processes at different temperatures, thus the scatter of the effective fracture toughness is dependent on temperature. In Fig. 2.14 the fracture toughness of an artificial steel is shown, which is similar to the high alloyed steels which are used within Siemens gas turbine rotor forgings. As shown here the material experiences a transition from brittle to ductile failure mechanism with increasing temperature, which is a typical behavior for body centered cubic crystal structures. In this case the transition occurs within the operational temperature range which is an important fact which has to be accounted for in the simulation.

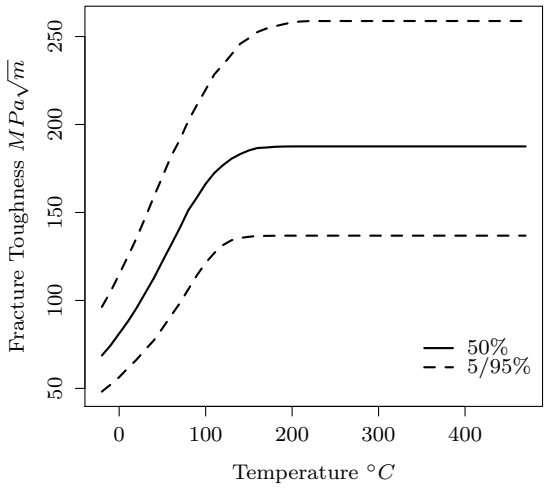

Figure 2.14.: Fracture toughness curve of an artificial material.

50% Fracture Appearance Transition Temperature Scaling Approach

The fracture toughness model has been tailored to the measured fracture toughness data of a high strength steel (CostE) shown in figure 2.10.

The fracture toughness is a temperature dependent material property. In addition to the temperature dependence, the fracture toughness is influenced by production variances. It also changes due to material aging during engine operation. In case of CostE, the available data shows that the lower and upper shelf fracture toughness levels are only marginally affected by aging processes, for the tested exposure temperatures and exposure times. Only the transition temperature changes due to embrittlement. Contrary to this, there are a number of other steels which exhibit a change of the lower and upper shelf fracture toughness in addition to the shift of the transition temperature. Therefore, the described scaling approach can not be applied in general. For CostE material, the shift of the transition temperature is also supported by the measured 50% Fracture Appearance Transition Temperature (FATT) data (Fig. 2.15). The FATT is defined as the temperature at which the fracture surface of a charpy notch specimen shows 50% ductile and 50% brittle surface morphology.

As the mean FATT is increasing with increasing aging time, a dimensionless tem-

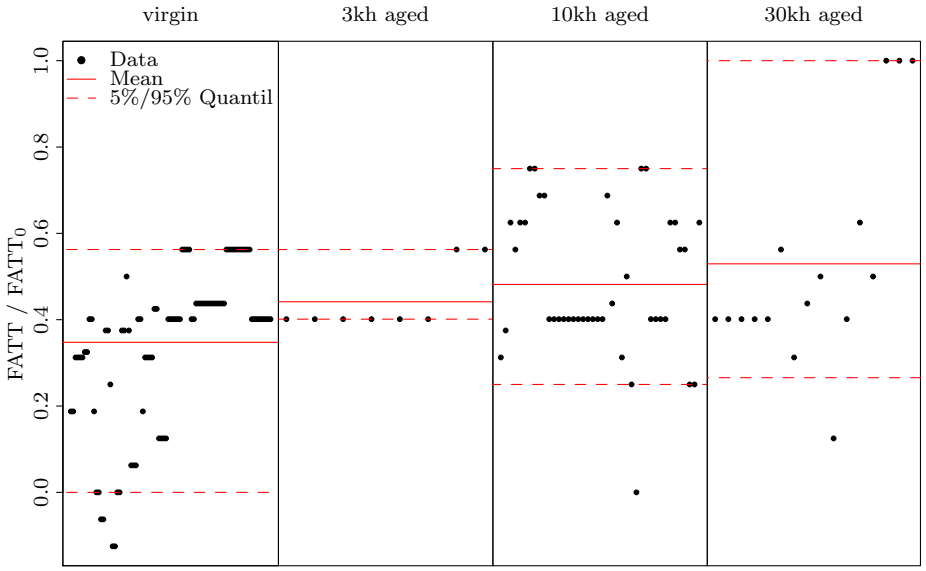

Figure 2.15.: Fracture appearance transition temperature of CostE material at different aging levels

perature approach has been chosen to describe the temperature dependence of the fracture toughness. The dimensionless temperature is defined as the ratio of the measurement temperature T_{meas} and the FATT of the specimen T_{FATT} (2.45), where all temperatures are given on the absolute Kelvin scale.

$$T_{rel} = \frac{T_{meas}}{T_{FATT}} \tag{2.45}$$

This scaling approach is somewhat different to the Wallin Master Curve approach but it delivers similar results for the fitted CostE fracture toughness data. The reason for not using the T_0 correction from the Master Curve approach is simply that this information is not available and in addition for embrittled material the slope in the transition region is a little bit smaller than for virgin material. This additional change in slope is effectively described by the scaling approach. A similar change in slope has also been described in literature for instance by Margolin et al. [32] for steel with a high degree of embrittlement. The $FATT$ is, in contradiction to T_0, measured routinely during the quality assurance testing for nearly all forged rotor components. Viehrig et al. [62] have shown that the T_0 distribution is similar to the $FATT$ distribution. Thus it seems likely to use the $FATT$ as a scaling parameter

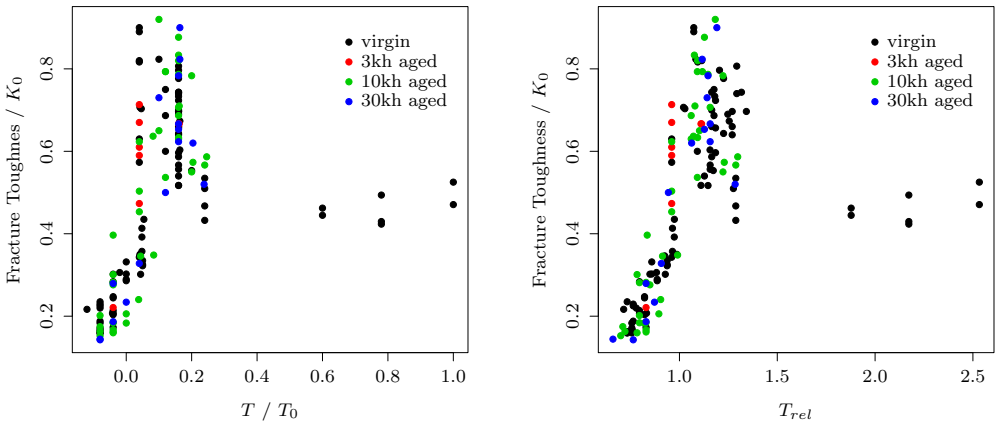

(a) Measured temperature

(b) Relative temperature

Figure 2.16.: Fracture toughness at different aging levels vs. measured temperature T and relative temperature T_{rel}

for the measurement temperature instead of T_0. The $FATT$ scaling approach can be seen as an approach to reduce the scatter, for instance originating from manufacturing differences (batch effect), by moving data in the transition region in a horizontal direction.

2.7.4. Crack Growth Rate Modeling

In *ProbFM* the crack growth rate is modeled as a fully correlated random process as shown by Yang et al. [67]. This is characterized by adding a random relative scatter to a scaling curve $F_{\frac{da}{dN}}(\Delta K, T, R)$ which has been fitted to the measured crack growth rates ((2.46)).

$$\left\langle \frac{da}{dN} \right\rangle = F_{\frac{da}{dN}}(\Delta K, T, R)\,(1 + \langle \epsilon_r \rangle) \tag{2.46}$$

In the following two different approaches are used to describe the crack growth rate, but in general any description can be used which follows the scheme of equation (2.46). In this work a Paris law type function, as given by equation 2.47 and a so called NASGRO-equation, as shown in (2.48), are used. In the Paris type model below

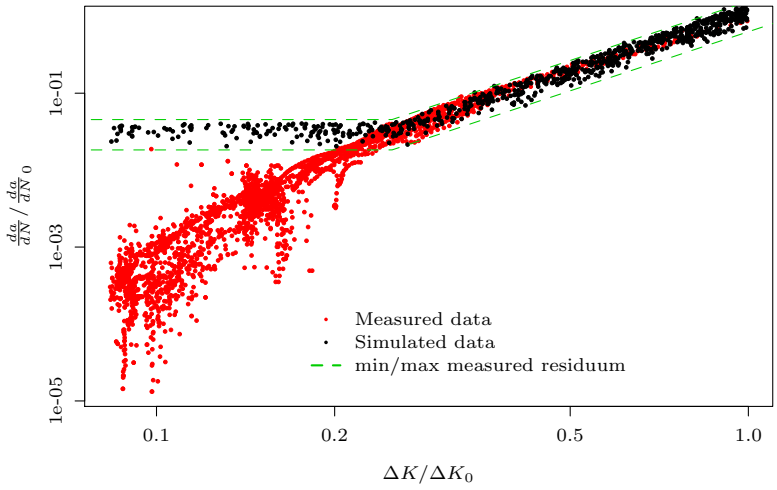

Figure 2.17.: Measured and simulated crack growth rate at 20°C and R=0.1 of COSTE material

a given stress intensity range ΔK_{con} the crack growth rate is kept constant (Figure 2.17).

$$F_{\frac{da}{dN}}(\Delta K, R, T) = \begin{cases} C(R,T)\ \Delta K^{m(R,T)} & \Delta K > \Delta K_{con} \\ C(R,T)\ \Delta K_{con}^{m(R,T)} & \Delta K \leq \Delta K_{con} \end{cases} \tag{2.47}$$

This is a conservative approach to describe the crack growth data close to the threshold stress intensity range ΔK. The reason for this is the increased scatter in the data close to ΔK, otherwise this increased scatter would be transfered by the modeling approach to the larger ΔK values. Furthermore this is a conservative approach to account for the possibility of abnormal crack growth rates of micro structural short cracks, which can occur close to the threshold stress intensity range ΔK [48; 52]. In the evaluated cases this has only a small effect on the calculated probabilities of failure as cracks which start with such low stress intensity ranges do not significantly contribute to probabilities of failure which are investigated. For a larger number of cycles, this might change since then even small cracks can grow to a critical size.

As *ProbFM* uses tabulated input data, other function types (2.48) can be used to describe the crack growth rate, for instance as published by Forman and Mettu [13] (Fig. 2.18).

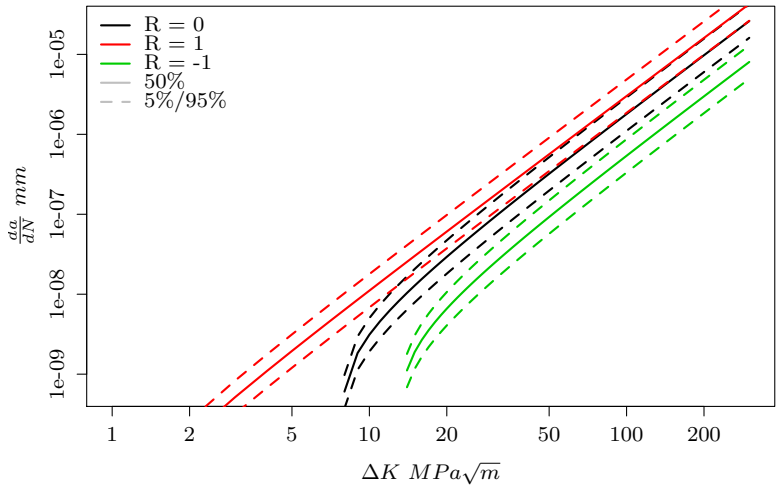

Figure 2.18.: Artificial crack growth rate model as used for comparison of deterministic and probabilistic assessments at $15°C$ for different R ratios.

$$F_{\frac{da}{dN}}(\Delta K, R, T) = C(R,T)\left(\left(\frac{1-f}{1-R}\right)\Delta K\right)^{n}\frac{\left(1-\frac{\Delta K_{th}}{\Delta K}\right)^{p}}{\left(1-\frac{K_{max}}{K_c}\right)^{q}} \tag{2.48}$$

Equation (2.48) will not be further discussed here, as there is a lot of information available in the literature. Further details in a condensed form on (2.48) can be found for instance in [57].

2.8. Ultrasonic Inspection

In general it is not possible to manufacture components in an industrial process without having any discontinuities. In large forged components like forged rotor disks of land based gas turbines, inherent discontinuities have to be expected. The major part of these discontinuities originate from the casting process of the ingot [20].

Therefore, Non Destructive Examination (NDE) methods are used to detect possible defects. For large forgings, the typical NDE method in use are ultrasonic examination techniques.

The state of the art ultrasonic inspection (UT) for heavy forgings for land based gas turbines is the so called pulse-echo technique (Fig. 2.19) [63; 68].

Typical discontinuities which are observed in rotor disks are [63]:

- metallic inclusion
- nonmetallic inclusion
- secondary pipes
- quench cracks

Metallic inclusions such as segregations are expected to be the most difficult discontinuities to detect, as the impedance difference between the discontinuities and the surrounding material is expected to be small, and therefore, the pulse echo to be low. Nonmetallic inclusions as metal oxides are typically well detectable due to the fact that the impedance difference to the surrounding material is large. Furthermore due to the forging process, they are usually oriented perpendicular to the ultrasonic sound path. This type of inclusion is the most frequently occurring inclusion in todays forgings. Secondary pipes are rather critical flaws as they tend to form close to the center of the ingot. These are also the areas where usually the highest stresses during operation occur. Secondary pipes can form during the solidification process of the ingot, during the shrinkage of the inner core or due to bursts during the forging process. Secondary pipes are often of center located and the surface of the inclusion is rough. Following they may be undersized as they are only detected by the outer cone of a radial scan and the sound wave is scattered due to the rough surface. The Irsching rotor failure (Fig. 1.2) [3] has been caused by such a type of flaw.

To assess the failure probability due to fatigue crack growth, the inherent flaw distribution is needed. This distribution is in general unknown and very expensive to obtain via direct measurements. Hence, an alternative assessment is used.

A simplified picture of the pulse echo technique is given in Fig. 2.19. A more comprehensive description of the pulse-echo method and the application can be found in [31]. From the fracture mechanics point of view, the measured pulse-echo signal contains two major features: the flaw echo and the noise threshold. The flaw echo can be converted into a circular disk reflector size (KSR) and is a measure for the size of the detected flaw, where the noise threshold is a measure for the smallest flaw size (KSR_{th}) which can be detected.

2.8.1. Circular Disk Reflector Correction Factor

The critical flaw size in land based gas turbine disks is usually smaller than the ultrasonic beam diameter area and the flaw size is estimated by the amplitude of the

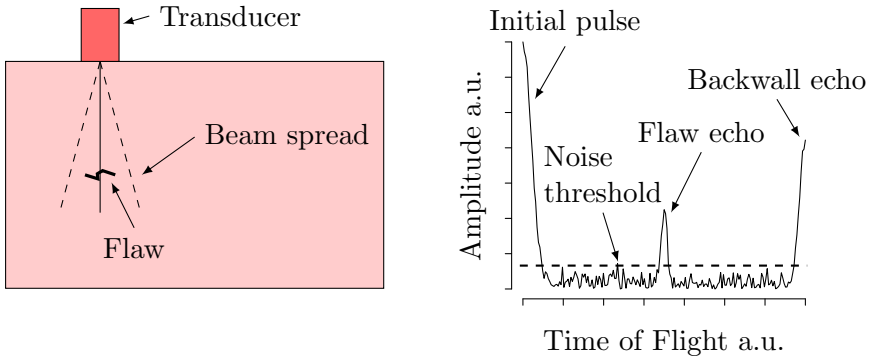

Figure 2.19.: Principle of the ultrasonic pulse-echo technique

reflected signal [30; 63].

The indication size is given in terms of the diameter of a circular flat bottom hole at the same sound path length as the indication.

As the echo amplitude is not only influenced by the area of the flaw but also by several other factors e.g. shape, roughness, material, orientation, ..., the ratio k (equation (2.49)) of the real size to the predicted size varies. Kern et al. [29] and Jestrich at al. [26] published some of these very rare and expensive measurements for large forgings (Fig. 2.20). The data from this publication is used for the conversion of the measured Circular Disk Reflector (Kreis Scheiben Reflektor KSR) size into a 'True Flaw Size' (TFS). Furthermore, it is assumed that the conversion factor is independent of the real flaw size. This assumption is not true for large flaws but it is conservative as the conversion factor of large flaws tends to one and the size of large indications should be over-sized in the simulation. Within the reported Kern data single and group indications have been differentiated. This is in principle an artificial difference as it depends on the resolution of the ultrasonic system, as even most of the single indications consist of several small inclusions. Thus in the presented results no distinction has been made between group and single indications.

As the ultrasonic technology has evolved since this conversion factors have been measured, it is expected, that the scatter of the conversion factor is reduced in todays ultrasonic measurement.

$$k = \frac{TFS}{KSR} \tag{2.49}$$

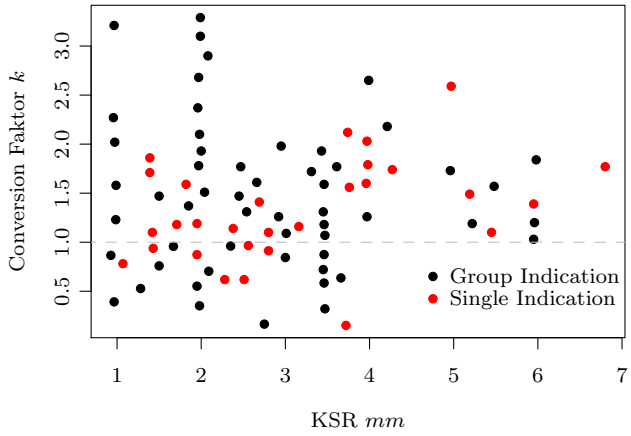

Figure 2.20.: KSR to TFS conversion as published in [29].

In the simulation, the conversion factor can be described by the measured conversion factors or by a distribution which has been fitted to the measured data. For example, three different distributions (lognormal $L(k)$, gamma $G(k)$ and Weibull $W(k)$) have been fitted to the measured data (Fig. 2.21 and Tab. 2.2). The density functions of the fitted distributions are given in equations (2.37)-(2.40).

	Parameters	Log-Likelihood	KS P-value	AD P-Value
Lognormal	$\mu = 0.21$; $\sigma = 0.58$	-91.56	0.30	0.20
Gamma	$s = 3.74$; $r = 0.38$	-85.19	0.83	0.78
Weibull	$a = 2.20$; $b = 1.60$	-83.59	0.97	0.97

Table 2.2.: Distribution parameters, Log-Likelihood and P-value of the Kolmogorov-Smirnov and Anderson-Darling test of the fitted distributions

The highest likelihood and p-value is given by the Weibull distribution (Tab. 2.2). Likewise the QQ and PP - Plots (Fig. 2.21) show that the Weibull distribution is a good description of the conversion factor distribution. Nevertheless, it might be that the Weibull distribution underestimates the occurrence rate of large conversion factors as shown by the QQ - Plot (Fig. 2.21c) Hence, the Gamma distribution is suggested

to use for simulation. The presented *ProbFM* results have been obtained using the measured data and not the fitted distributions.

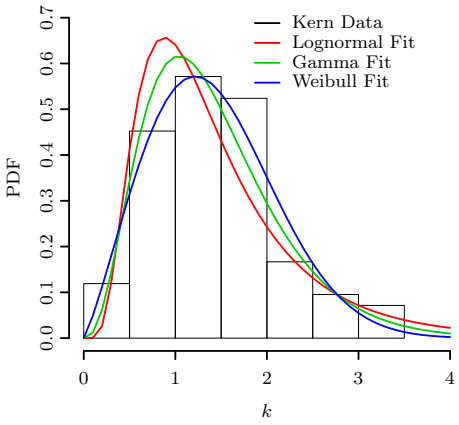

(a) Estimated and fitted PDF

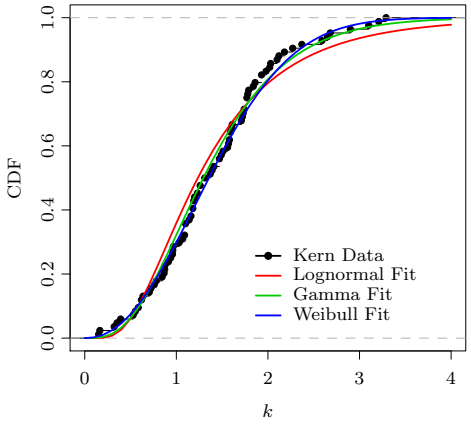

(b) Estimated and fitted CDF

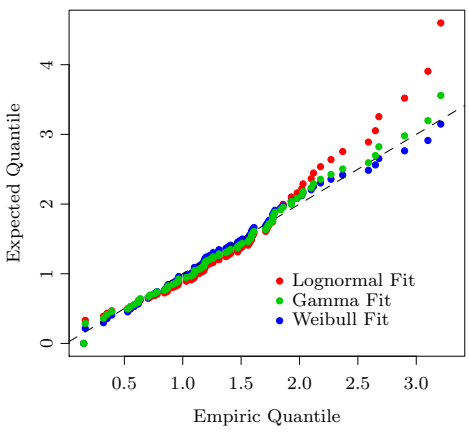

(c) qq-Plot of the estimated and fitted Probability functions

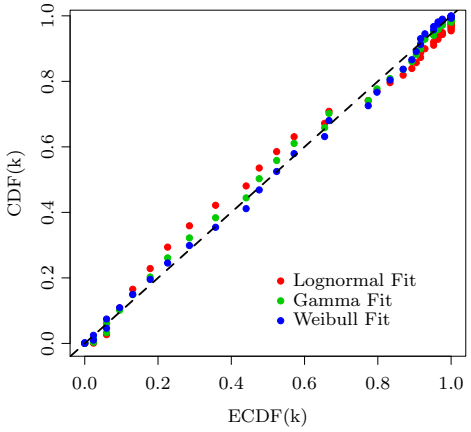

(d) pp-Plot of the estimated and fitted Probability functions

Figure 2.21.: Comparison of the estimated Probability function of the conversion factor and fitted Probability functions

2.8.2. Probability of Detection

Additional to the size uncertainty of an ultrasonic indication, it is possible to not detect a flaw at all. There are several approaches in the literature describing how to deal with this Probability of Detection (PoD) and how it can be estimated [17]. In general, the PoD of natural inherent flaws is unknown and can only be estimated with destructive methods.

One way to estimate the PoD is to introduce known artificial flaws into a component and do several ultrasonic inspections. This approach is very expensive, and in general, natural flaws have a different ultrasonic signal than artificial flaws.

Another possibility to estimate the PoD is to explicitly use the knowledge of the conversion factor distribution and assuming a KSR threshold value (KSR_{th}) [17]. This approach is called the Threshold Value Theorem (TVT). All KSR values larger than KSR_{th} will be detected and all smaller ones will not be detected. The KSR_{th} value can be either the noise threshold given by the ultrasonic inspection technique or a KSR reporting limit (whichever is larger). With these assumptions, the POD can be estimated by equation 2.50

$$PoD\left(TFS\right) = Pr\left(KSR > KSR_{th}\right) \tag{2.50}$$

where $Pr\left(\cdot\right)$ is the Probability of the event $(\cdot)$.

Using the KSR - TFS conversion approach shown in subsection 2.8.1 and combining equations 2.49 and 2.50, the PoD estimate can be calculated by equation 2.52.

$$PoD\left(TFS\right) = Pr\left(KSR > KSR_{th}\right) \tag{2.51}$$

$$= Pr\left(\frac{TFS}{k} > KSR_{th}\right) \tag{2.52}$$

Assuming $KSR_{th} = 1.0$mm, using the measured k data and the fitted distributions, the PoD estimates shown in Fig. 2.22 can be calculated. The plot shows that in this case the chosen distribution type to describe the conversion factor distribution has only a small influence on the PoD.

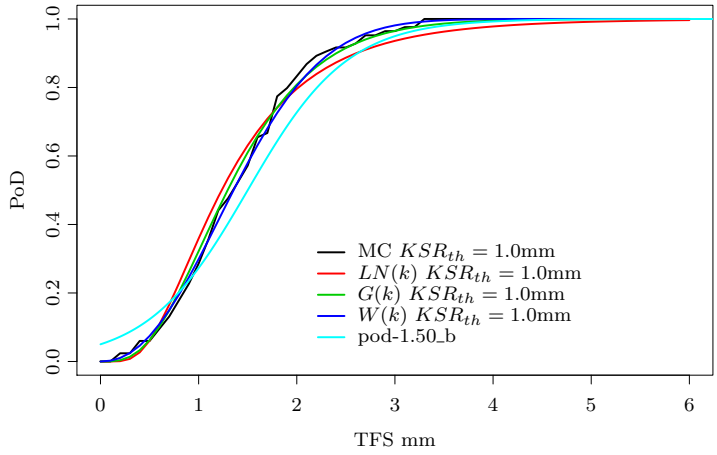

Figure 2.22.: PoD's estimated from the measured conversion factor distribution based on the data published by [29] and fitted functions using KSR_{th} = 1.0mm

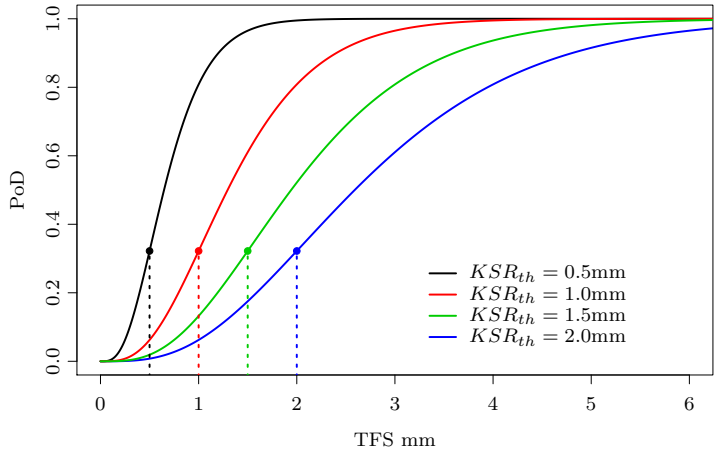

Figure 2.23.: Estimated PoD's using the fitted Gamma distribution and different KSR_{th} values

If the conversion factor k is assumed to be independent of the real flaw size TFS (as in (2.52)) then the PoD can be calculated by a simple scaling approach from one 'Master'-PoD. In this case, only the TFS-axis has to be scaled by the KSR_{th} value. This is shown in Fig. 2.23 by the vertical lines which are located at the KSR_{th}

value which has been used for the calculation of the corresponding PoD. Due to this scaling, the PoD distribution becomes broader for larger KSR_{th} values and is not only shifted to the KSR_{th} location as might be expected.

2.8.3. Observed KSR Database

Currently Siemens is running a Gas Turbine fleet of approx 1000 units. During production, ultrasonic inspections of the rotor parts have been performed and the results have been stored into a database. Several of the inspected components contain ultrasonic indications. The empiric probability function of the flaw sizes of this database is shown in Figure 2.24. [1] The database contains information about the total number of inspected parts N_t, the type of inspected components, the total number of indications N_{ind}, the KSR size, the location of indications which have been detected and the volume of the inspected components.

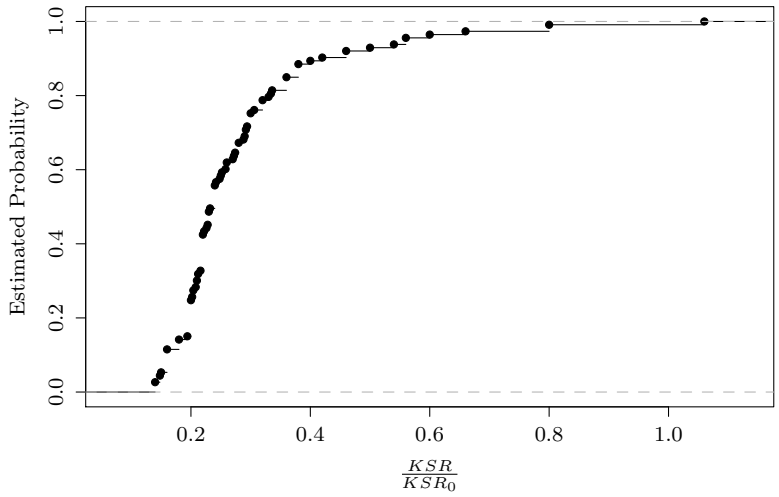

Figure 2.24.: Indication size probability in the Siemens NDE database

To calculate a probability of failure, estimates of the flaw density, the flaw size distribution and the flaw locations are required. All these pieces of information can be extracted from the given database.

From the database, a KSR list can be extracted which contains N_t entries. Assuming that flaws occur independent of each other, N_{ind} entries are non-zero entries

[1] For confidentiality reasons the reported KSR sizes have been scaled by KSR_0.

and contain the reported KSR size of the indications. The N_{ind} entries in the list are an estimate of the flaw size distribution. In conjunction with the zero entries and the mean inspected component volume, the list is also an estimate for the mean flaw density per volume.

In addition to the information about the size and the mean flaw density, information about the radial flaw distribution can be obtained from the KSR database.

The total number of flaws N_{ind} is assumed to be proportional to the total volume V_{tot} of all assessed forging ingots.

$$\rho_{Flaw} = \frac{N_{ind}}{V_{tot}} \tag{2.53}$$

Furthermore, the KSR database shows that the flaw density is dependent on the radial position in the component. This seems to be related to the solidification process of the ingot as the ingot solidifies from the outside to the inside. The solidification front drives impurities to the middle of the ingot. Therefore, the flaw density increases with decreasing radial position (Figure 2.25). The database contains several components with different ingot diameters. To compare the different ingot sizes, it is assumed that the radial position r can be scaled by the outer diameter d_{out} of the ingot (2.54). The observed Siemens fleet data are taken from forgings with different diameters and the radial flaw density distribution can be described as a function of a relative radial position r_{rel} (2.54).

$$r_{rel} = \frac{r}{d_{out}} \tag{2.54}$$

Using this assumption, the probability of flaw occurrence shown in Fig. 2.25 can be obtained from the Siemens ultrasonic database.

2.8.4. Expected True Flaw Size Distribution

On basis of the observed KSR PDF and the conversion factor PDF, an estimate of the 'observed' true flaw size TFS_{obs} PDF, can be calculated by equation 2.55.

$$f_{KSR \cdot k_{dat}}(z) = \int_{-\infty}^{\infty} \frac{1}{|t|} f_{KSR}(t)\ f_{k_{dat}}\left(\frac{z}{t}\right) dt \tag{2.55}$$

A more convenient way to calculate the $\langle TFS_{obs} \rangle$ realization by numeric means is the Kronecker product of the $\langle KSR \rangle$ data list and the conversion factor data list $\langle k \rangle$ 2.56.

$$\langle TFS_{obs} \rangle = \langle KSR \rangle \otimes \langle k_{dat} \rangle \tag{2.56}$$

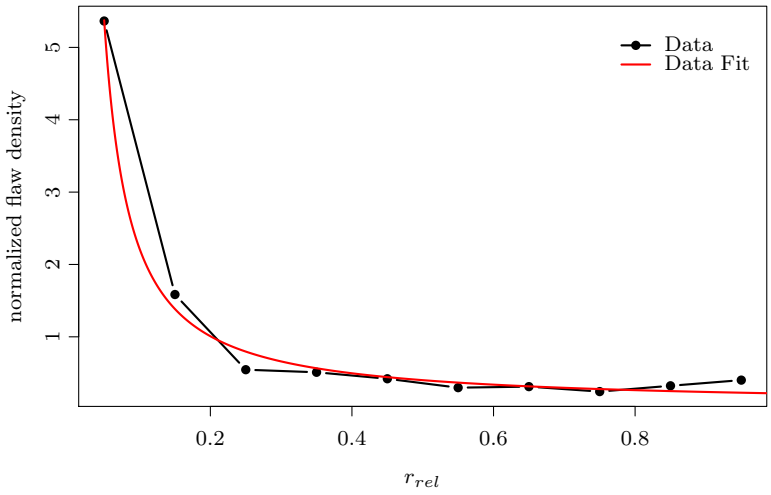

Figure 2.25.: Flaw occurrence probability vs. relative radial component position

$\langle TFS_{obs} \rangle$ is only an estimate for the TFS sizes of the observed KSR sizes as pointed out in subsection 2.8.2. There is still the probability of flaws which have not been detected by ultrasonic inspection, which has to be accounted for by a PoD_{dat}. The expected true flaw size PDF f_{exp} (2.57) describes the flaw size distribution in a component if no ultrasonic examination is conducted.

$$f_{exp}(TFS) = \frac{f_{obs}(TFS)}{PoD_{dat}(TFS)} \tag{2.57}$$

If the probability density function ($f_{obs}(TFS)$) of the observed TFS_{obs} is available, then the expected probability density function f_{exp} can be calculated by equation (2.57).

If $\langle TFS_{obs} \rangle$ has been calculated using equation (2.56) the probability density function $f_{obs}(TFS)$ is unknown. In this case, $\langle TFS_{exp} \rangle$ can be calculated by a Monte-Carlo (MC) process.

$$\langle TFS_{exp} \rangle = MC_{PoD\_dat}[\langle TFS_{obs} \rangle] \tag{2.58}$$

The MC process MC_{PoD_dat} in equation (2.58) changes the number of the non

zero entries according to equation 2.59 with n_{i_new} entries of size TFS_i in $\langle TFS_{exp} \rangle$, n_{i_old} number of entries with size TFS_i in $\langle TFS_{obs} \rangle$, N_{obs} total number of entries in $\langle TFS_{obs} \rangle$, N being the number of components and $PoD_{dat}(TFS_i)$ the probability of detection at TFS_i for the KSR database. The discretizing error, which is generated by the limited number of entries, can be reduced by expanding $\langle TFS_{obs} \rangle$ by an integer factor. The larger the factor the smaller the discretizing error. This assessment is a reasonably good estimate as long as the number of indications per component or reference volume is smaller than 1. Otherwise, the number of required non-zero entries is larger than the number of entries in the list. An easy way to circumvent this problem is to reduce the components volume artificially and multiply the PoF results by that reduction factor.

$$n_{i\_new} = round\left[n_{i\_old}\frac{N}{N_{obs}}\frac{1}{PoD_{dat}(TFS_i)}\right] \tag{2.59}$$

TFS_{exp} is the expected true flaw size distribution in the reference volume if no ultrasonic examination is conducted.

2.8.5. Expected True Flaw Size Distribution after Ultrasonic Inspection

In general, ultrasonic inspection is performed for each component before it is assembled in a gas turbine. Therefore, it is possible to scrap components with ultrasonic indications and thus reduce the number of possible flaws in the components of the fleet. This inspection process is described by a second probability of detection, PoD_{acc}, and a KSR limit KSR_{lim}. KSR_{lim} is the largest KSR size which is expected to be in the KSR distribution.

For instance, if an ultrasonic indication is larger than the deterministic decision limit KSR_{dec}, the component is scrapped. Consequently the flaw is removed from the simulation flaw ensemble. Just as described in subsection 2.8.4, there are two possibilities to calculate the expected true flaw size after inspection, TFS_{acc}. On the one hand, if the probability density functions are available the probability density function f_{acc} can be calculated by equation (2.60).

$$f_{acc}(TFS) = f_{exp}(TFS)\left[1 - Pr\left(\frac{TFS}{k_{acc}} > KSR_{lim}\right) \cdot PoD_{acc}(TFS)\right] \tag{2.60}$$

On the other hand, if no probability functions are available but a list of realizations $\langle TFS_{exp} \rangle$, then the list of realizations $\langle TFS_{acc} \rangle$ can be calculated by a MC process (equation 2.61)

$$\langle TFS_{acc} \rangle = PoD_{MC\_acc} \left[\langle TFS_{exp} \rangle \right] \tag{2.61}$$

The PoD_{MC_acc} process removes an entry TFS_i from the realization list $\langle TFS_{exp} \rangle$ if the following two conditions are fulfilled.

$$\frac{TFS_{exp\_i}}{k_{acc\_i}} \geq KSR_{lim} \tag{2.62}$$

$$random\,(0,1)_i \leq PoD_{acc}\,(TFS_{exp\_i}) \tag{2.63}$$

The evolution from the KSR database to the final TFS_{acc} distribution is shown in Figure 2.26.

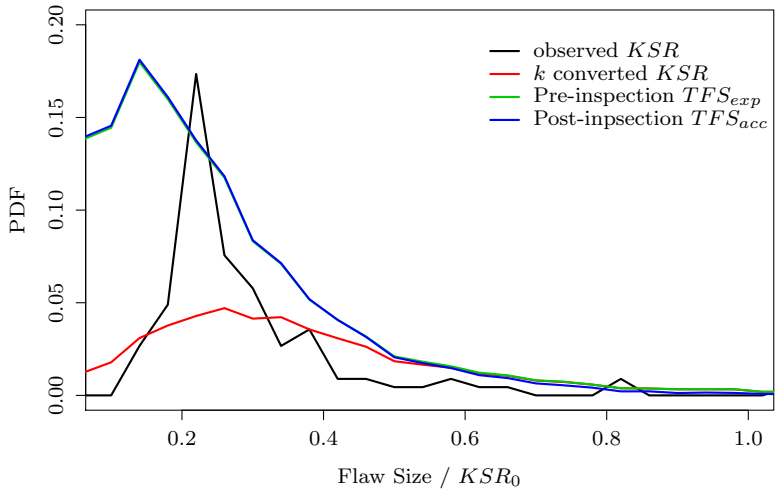

Figure 2.26.: Anomaly Size Distribution developed from the KSR database, with group and single indication conversion, PoD_{dat} is pod-1.50_b.tab, PoD_{acc} is pod-3.00_b.tab, correlated k values and a KSR decision limit of 2mm.

As $\langle TFS_{acc} \rangle$ is finally calculated from the $\langle KSR \rangle$ realization list, $\langle k_{dat} \rangle$ and $\langle k_{acc} \rangle$ can be assumed to be either completely correlated or uncorrelated. In case of uncorrelated data, a slightly lower probability of large flaws in the component is obtained. One comparison of a correlated and an uncorrelated TFS_{acc} distribution is shown in Figure 2.27.

Until now there are no data available to validate the TFS_{exp} distribution for large rotor forgings. The only possibility so far is to compare the TFS_{exp} with true flaw

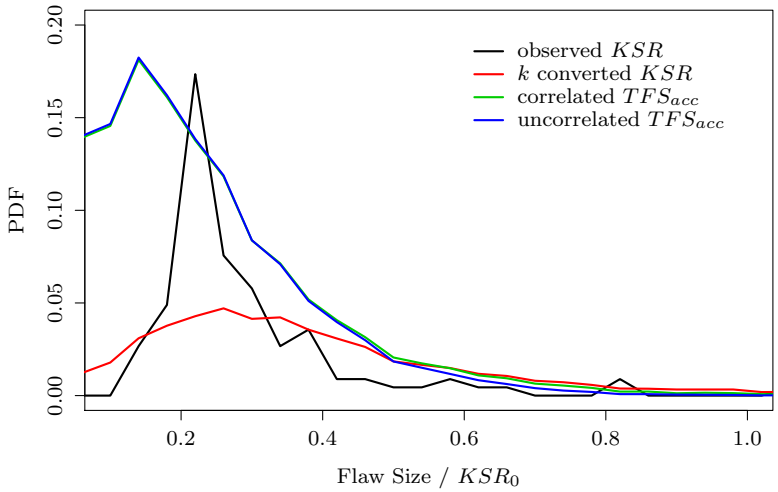

Figure 2.27.: Anomaly Size Distribution developed from the KSR database, with group and single indication conversion, PoD_{dat} is pod-1.50_b.tab, PoD_{acc} is pod-3.00_b.tab. With correlated and uncorrelated k values and a KSR decision limit of 2mm.

size distribution estimates implemented in DARWIN (Figure 2.28). This comparison is only of limited value as the production process, the material (Titanium alloys) and the flaw type (Hard Alpha inclusions) are different. However, it shows significantly more and larger flaws in the large stationary gas turbine disks as in aero engine disks.

The TFS distributions in DARWIN are given in terms of an *exceedance rate* (Fig. 2.28). An *exceedance Rate* describes the amount of flaws which are larger as a defined flaw size and is given as a function of the flaw area.

2.8.6. Initial True Flaw Size Distribution calculation

In the chapters 2.8.1 to 2.8.5 the single parts of a methodology to calculate an estimate of the initial true flaw size distribution expected in a gas turbine fleet have been described. A total picture of the whole process is given in Fig. 2.29. The calculation of the initial TFS consists of three sub steps described below.

The first step described in chapter 2.8.3 is the calculation of the true flaw size which is expected based on the observed KSR and k distributions. As mentioned in chapter 2.8.1 generally only the reported ultrasonic signals are available which are not equal

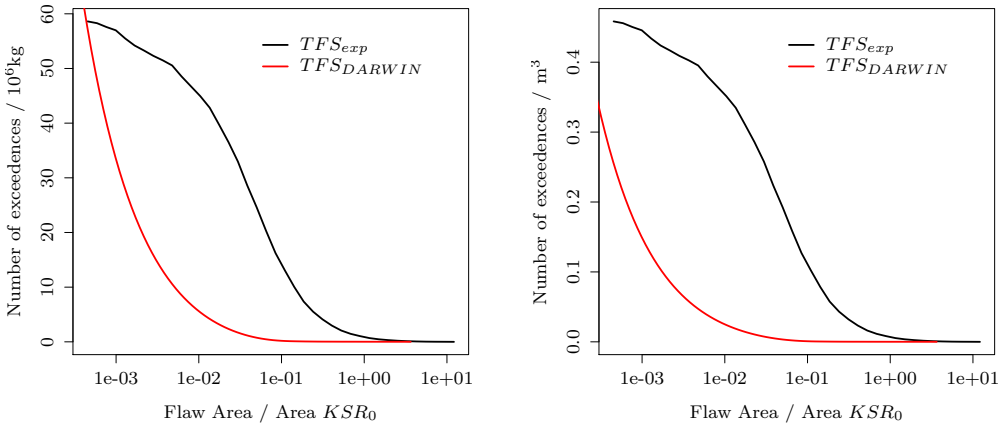

(a) Mass based TFS exceedance rate (b) Volume based TFS exceedance rate

Figure 2.28.: Comparison of the $ProbFM$ TFS_{dat} exceedance rate (estimated from KSR-database, conversion distribution and PoD1.50_b) and the worst case DARWIN exceedance rate TFS_{DARWIN}.

to the TFS. Thus the reported ultrasonic signals have to be converted into a TFS value. The ratio of the KSR and the TFS value depends on many factors, where many of them are unknown during a ultrasonic inspection of a component. Thus the conversion factor k has to be described in a probabilistic simulation by a distribution. The result of the KSR distribution transformation into a TFS distribution by the conversion factor distribution is the so called observed TFS distribution TFS_{obs}. This distribution is expected to be observed if all observed KSR indications would be broken up.

In the second step the possibility of not finding flaws is accounted for by increasing the occurrence probability of flaws depending on the TFS value, as described in chapter 2.8.4. So far the TFS_{obs} distribution describes only the TFS sizes of the indications which have been detected. In general it is possible that some inclusions have not been detected. For instance the detection of small inclusions is very unlikely and also larger inclusions can be undetected if for instance the orientation of the inclusion is awkward. This probability of missing an inclusion in general is accounted for by the PoD as described in chapter 2.8.2. As in general, large flaws are easier

to detect than small flaws, the occurrence probability of small flaws is more strongly influenced by this step than the occurrence probability of large flaws. The result of this step describes the true flaw size occurrence probability in a component which has not been ultrasonically tested, as the KSR database contains all observed indications, even if a component has been scrapped based on the the found indication.

The third step outlined in chapter 2.8.5 accounts for a possible quality assurance process which removes detected critical indications from the simulation. Due to this the occurrence probability of flaws is reduced. As a reminder, the decision if a component has to be rejected or not is based on the observed KSR value, not on the TFS value. Thus if a flaw has been detected within the simulation, an observed KSR value has to be calculated from the TFS value and compared to a limiting value KSR_{lim}. If the observed KSR value is larger than the decision limit KSR_{lim} the component is removed from the simulation ensemble, to account for the quality assurance process.

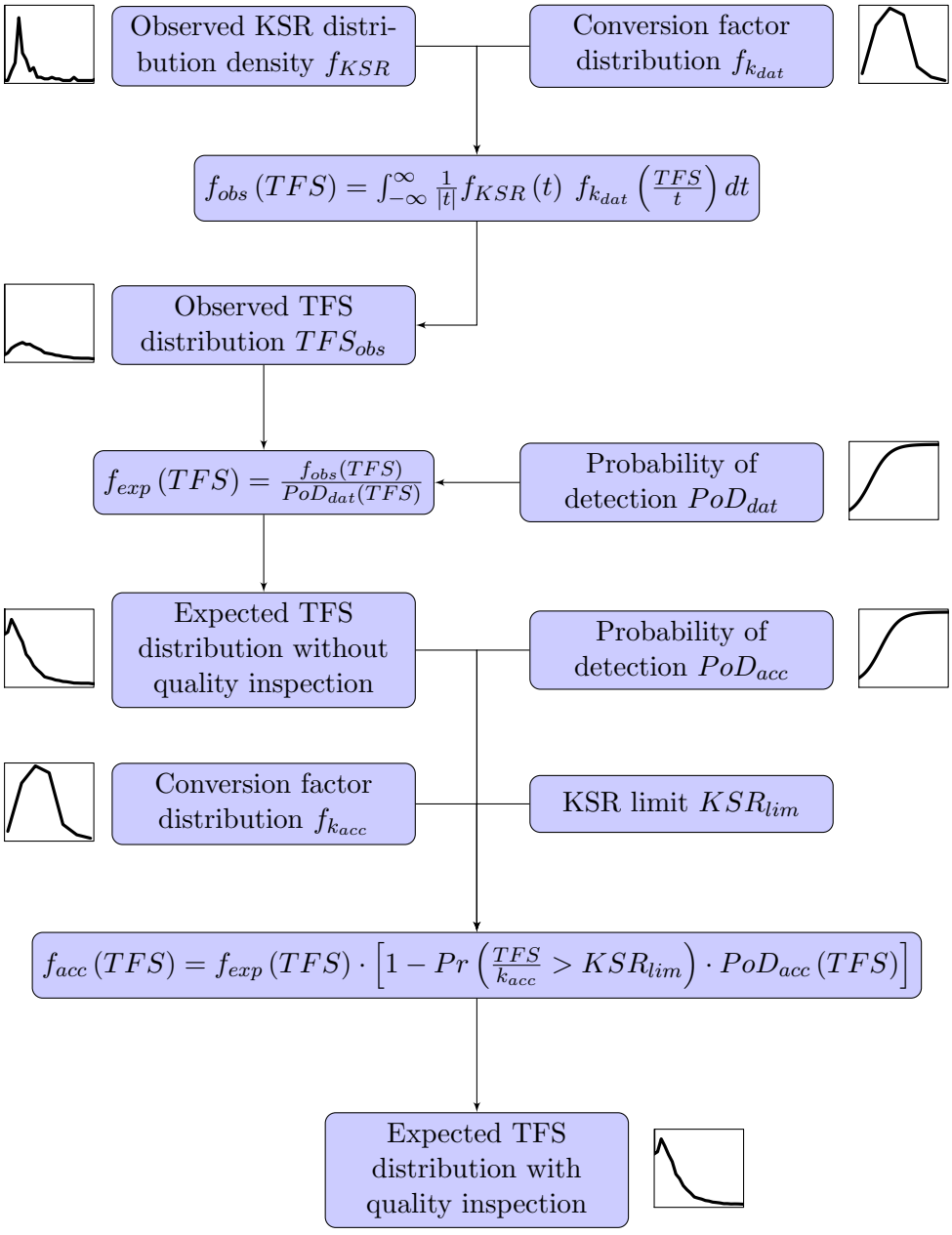

Figure 2.29.: Flowchart of the true flaw size distribution estimation process in the component assuming uncorrelated conversion factor distributions k_{dat} and k_{acc}.

2.8.7. Crack Interaction Probability

ProbFM does not account for the interaction of cracks. It has been shown by Ch. Weichert [66] that interacting cracks can lead to a significantly increased crack growth. The interaction of cracks can be modeled by FEA or involved analytic techniques. Ch. Weichert [66] gives an estimate for the interaction function (2.64) which describes the increase in the stress intensity at the facing crack tips.

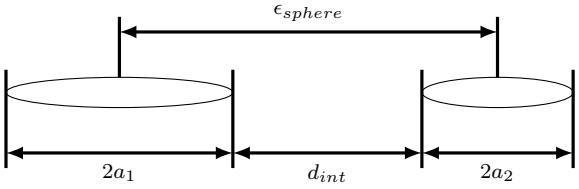

Figure 2.30.: Definition of the crack interaction distance

$$f_{int}\left(\frac{d_{int}}{2a_1}, \frac{a_1}{a_2}\right) = 0.94 + \frac{0.16 + \frac{0.2538}{\frac{a_1}{a_2}}}{\frac{d_{int}}{2a_1}} \; ; a_1 \geq a_2 \tag{2.64}$$

d_{int} is the distance between the two facing crack tips as shown in Fig. 2.30, a_1 is the small half axis of the larger crack and a_2 of the smaller crack.

Ch. Weichert suggests to neglect the crack interaction at $d_{int} = 1.7 \cdot a_1$. At this distance the interaction function is in the order of 1.15. Based on this estimate, the flaw density, a critical crack size and, assuming independence of the crack occurrence, the occurrence probability of interacting cracks can be estimated.

Assuming all cracks in a sphere with the radius ϵ_{sphere} are interacting as described by the interaction function f_{int}. This is a conservative assumption, as most of the cracks in the sphere are not coplanar and might be oriented in different directions, which weakens the interaction of the cracks. The radius ϵ_{sphere} of the sphere can be estimated by (2.66).

$$V_s(\epsilon) = \frac{4}{3}\pi \, \epsilon_{sphere}^3 \tag{2.65}$$

$$\epsilon_{sphere} = d_{max} + a_1 + a_2 \tag{2.66}$$

Here, a_2 is set to a_1 as an upper bound for the sphere size of interacting cracks and $a_1 = TFS/2$. d_{max} can be defined as a factor of a_1 as shown in (2.67).

$$d_{max} = g\, a_1 \tag{2.67}$$

The factor g can be set to 1.7 as suggested by [66] or even larger values, for instance 3, to get more conservative results. With the described assumptions ϵ_{sphere} becomes

$$\epsilon_{sphere} = a_1\ (2+g) = \frac{TFS}{2}\ (2+g) \tag{2.68}$$

$$V_s\,(TFS) = \frac{4}{3}\pi\,\frac{TFS}{2}\ (2+g) \tag{2.69}$$

An upper bound estimate of the lifetime crack interaction probability can be calculated by assuming a critical crack size TFS_{crit} at which a crack will lead to failure. This can be used to estimate the lifetime interaction probability density (2.70) and probability (2.71). The interaction probability density is given by the product of the probability of finding a flaw of the size TFS in the component and a flaw with a smaller flaw size within a sphere with a volume as given by (2.69). In the case the flaw size is larger than the critical flaw size, the component fails. Following, it does not matter if this flaw interacts with other flaws.

$$p_{life}\,(TFS, TFS_{crit}) = \begin{cases} \rho_{flaw}\,(TFS)\ P_{flaw}\,(TFS)\ V_c\, V_s\,(TFS)\,, & TFS \geq TFS_{crit} \\ \rho_{flaw}\,(TFS)\ P_{flaw}\,(TFS)\ V_c\, V_s\,(TFS_{crit})\,, & TFS < TFS_{crit} \end{cases} \tag{2.70}$$

p_{life} denotes the lifetime interaction probability density, $\rho_{flaw}\,(TFS)$ is the volume based flaw density as function of the TFS, $P_{flaw}\,(TFS)$ is the cumulative volume based flaw density, V_c is the volume of the component and V_s is the TFS dependent volume of the sphere of interaction.

Finally the interaction probability of observing any crack interactions between flaws up to a given size, is given by the cumulative probability, as defined by (2.71).

$$P_{life}\,(TFS_{crit}) = \int_0^\infty p_{life}\,(TFS, TFS_{crit})\,\delta TFS \tag{2.71}$$

P_{life} is the cumulative lifetime interaction probability as function of the critical crack size. If the flaws do not tend to cluster or to occur in groups, this is a conservative estimate for the interaction probability of flaws as it is assumed that all flaws grow until they reach a critical size.

With the initial TFS distribution determined from the Siemens NDE Database (Fig. 2.31) and assuming a mean component volume $V_c = 0.7\mathrm{m}^3$, P_{life} can be calculated (Fig. 2.32).

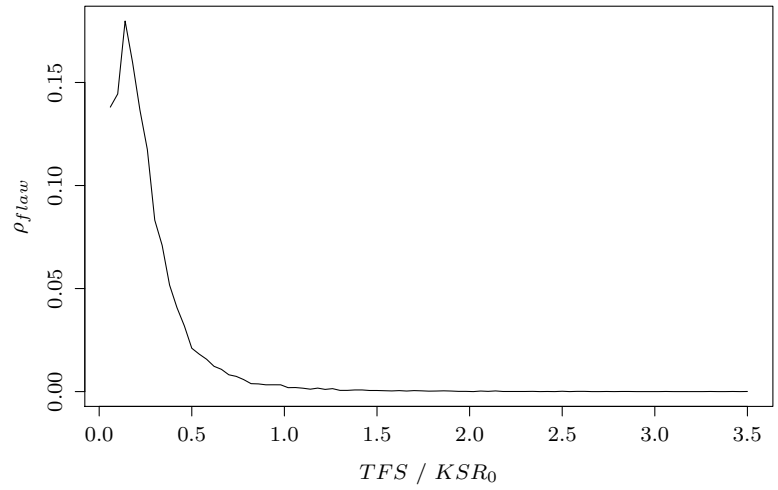

Figure 2.31.: Assumed flaw density vs. flaw size in large forged rotor components of gas turbines.

The upper bound estimate of the lifetime crack interaction probability P_{life} in the whole component is in the order 10^{-7} to $5 \cdot 10^{-6}$ for typical critical crack sizes of gas turbine rotor forgings.

The lifetime PoF of a critical component is in the order of 10^{-4} [10]. As the lifetime crack interaction probability is 2-3 orders of magnitude smaller, this effect will not significantly contribute.

This statement is only valid for the described boundary conditions and components. For other component types, for instance steam turbine rotors, this might be different since the production process and the component size are different as compared to the gas turbine rotor components, or the flaws might tend to build clusters.

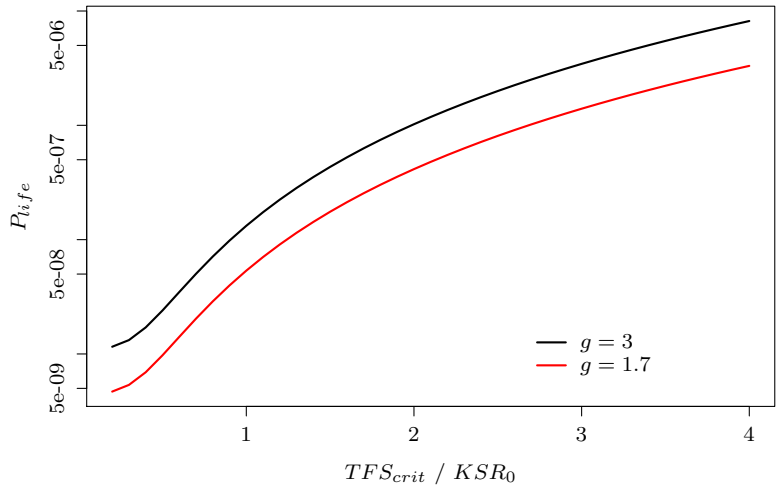

Figure 2.32.: Estimate of the crack interaction probability during the crack lifetime.

2.9. Conservative Assumptions in Probabilistic Fracture Mechanics Code

Several conservative assumptions are made in the described probabilistic fracture mechanics modeling. Therefore, the calculated probability of failure is an upper bound of the expected probability of failure:

- ***Crack Nucleation Time***
  Initially, most of the forging flaws are not cracks to begin with. It takes some cyclic loading to form a sharp crack tip which can be described by Irwin plastic zone extension methods. The modeling of this crack nucleation time is complicated and is influenced by several factors. *ProbFM* conservatively assumes that crack formation time is zero, and flaws start immediately to grow as cracks. Studies of the Fraunhofer Institute in Freiburg that investigated specimens of our rotor steels with ultrasonic indication show that for small indications (<2mm KSR) several thousand cycles at 600-800MPa are needed to nucleate those flaws into cracks (see section A.5 for details). As only a limited number of such very involved tests have been conducted, we would be hesitant to generalize these statements and to apply this to our lifing methodology as is. However, future

studies of that nature might give enough statistical insight to take advantage of this possibly huge safety margin. Further modeling efforts in that area can support such an approach.

- ***Crack Orientation***
  ProbFM assumes that any flaw is always mode I oriented (worst case)

- ***Residual Scatter Modeling***
  As for most material properties only a limited amount of data is available, *ProbFM* conservatively assumes that the relative scatter of the data is constant and not a function of the temperature or other parameters. Since low probabilities are calculated, every additional scatter will increase the failure probability. With the assumed approach, scatter from one region — for instance high temperature regions, or transition regions— will be also assumed for all other regions. Hence, the approach overestimates the probability of failure.

- ***Crack Growth Modeling***
  ProbFM assumes the crack growth rate at the highest temperature and maximum stress range during the cycle. Therefore, the crack growth is overestimated as these states do not necessarily occur at the same point in time.

- ***Surface Effect***
  ProbFM accounts for the surface effect on the stress intensity for embedded cracks in a conservative way. The stress intensity of an embedded crack without surface effect or gradient is the same at the crack tips a_1 and a_2 as shown in Fig. 2.5. If an embedded crack is near to a surface, this is not the case and the stress intensity at the crack a_1 which is closer to the surface is higher as the one at the other crack tip a_2 (2.72).

$$SIF\,(a_1) > SIF\,(a_2) \tag{2.72}$$

  In *ProbFM* only the higher stress intensity ($SIF\,(a_1)$) is calculated and used for the crack growth calculation at both crack tips. In general, the crack growth is overestimated by this (see Fig. A.8)

- ***Stress Gradient***
  In case of a gradient stress field, a similar assessment is done as for the surface effect. Only the increased stress intensity is used for the crack growth calculation. The crack growth is in general overestimated by this as shown in Fig. A.7.

- ***Threshold value*** KSR_{th}
  The KSR_{th} value is an increasing function of the length of the sound path. In general, it is estimated by the longest possible sound path. Hence, the POD estimate by the threshold value theorem underestimates the real PoD for most regions of the component and the total amount of flaws is overestimated.

- ***Conversion factor distribution***
  ProbFM assumes that the ultrasonic flaw size conversion factor is independent of the true flaw size. As only the low tails of the PoF are of interest, this is in general a conservative assumption as for larger flaws the conversion factor tends to be reduced [54].

In addition to these modeling conservatisms which are included in the *ProbFM* code, the user can model the input data in a conservative way. One example for such a conservative material modeling is shown in Fig. 2.17, where the crack growth rate is kept constant for $\Delta K \leq \Delta K_{con}$ to assure that the small crack growth is described in a conservative way.

One uncertainty which is not captured up to now is the uncertainty in the FEA results which are related to the material property, geometry and service condition uncertainties. To account for these uncertainties in a conservative manner, worst case conditions, for instance cold starts of the engine ($-20°$C metal temperature) and daily starts are used for calculation. The combination of these assumptions is physical impossible, as a typical stationary gas turbine rotor needs several days to cool down to ambient conditions.

In general it is not possible to give an exact estimate of the factor between the expected and calculated PoF since the expected PoF is unknown. But at least a rough estimate of the different contributing factors is given in Tab. 2.3. Most of the factors are expected to be in the order of $\approx 1 - 2$ as there are accurate modeling approaches available. The biggest part of the overestimation originates from the assumption that it is assumed that each possible flaw starts to grow at the first cycle like a sharp crack. As will be shown in chapter A.5, this is not the case and it can take a large amount of cycles until such a crack is nucleated. The number of cycles to failure is underestimated or vice versa the PoF at a given cycle number is overestimated.

Contributing Factor Name	Factor
Crack Nucleation Time	$\approx 10 - 100$
Crack Orientation	$\approx 1 - 2$
Crack Growth Modeling	$\approx 1 - 2$
Surface Effect	$\approx 1 - 2$
Stress Gradient	$\approx 1 - 2$
Threshold Value KSR_{th}	$\approx 1 - 2$
Conversion factor k	$\approx 1 - 2$
Stress Intensity Factor Solutions	$\approx 1 - 2$
Total	$\approx 10^1 - 10^4$

Table 2.3.: Estimation of the overrating of the *PoF* in a *ProbFM* calculation

3. Stress and Temperature Fields

Gas turbines components experience complex transient stress and temperature cycles due to different operational conditions. These changing stress and temperature fields can be simulated by means of finite elements (FE). The FE modeling of rotational symmetric components is often done in a 2D axis symmetric model and the examples shown in this work reflect this. However, the presented methods can also be used for the assessment of 3D models.

As there are many different commercial FE codes in use, an intermediate file format has been defined. It can be created by all available codes and contains the location, transient stress tensor and temperature information of each node in the FE model.

The stress and temperature information is mapped on a regular grid or voxel ('volume pixel') structure which in general has a much finer spacing than the spacing of a finite element mesh. This voxel representation of the component can be compared with the pixel structure of a bit map picture. Here instead of colors we have stresses, temperatures, failures, geometric information, etc. The values are stored linearly in RAM memory and can be accessed very fast for evaluation when needed. Furthermore, the 'voxelized' component can be easily stored and transferred for later use.

3.1. Critical Stress and Temperature State for Crack Growth Calculation

The critical state for the fatigue crack growth rate during an operating cycle is not defined by a single load step as the fatigue crack growth is assumed to be driven by the change in the stress intensity during a cycle. In the same cycle, also the temperature may change and it is not possible to define one single critical load step. Therefore, the temperature and stresses for the crack growth calculation are defined in a conservative way by assuming the maximum stress range and associated R-ratio and the maximum temperature. In general, the maximum temperature will yield the maximum crack growth rate.

The first assumption for the assessment of the stresses for crack growth calculation is that the crack is always growing perpendicular to the transient maximum first principle stress σ_I^{max} during the cycle (eqn. (3.1)). The maximum value σ_I^{max} and

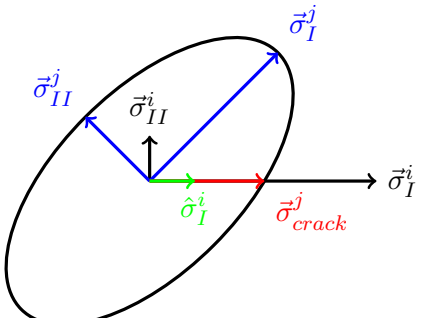

Figure 3.1.: 2D example of the calculation of the stress acting orthogonal to the crack plane

the direction $\hat{\sigma}_I^{max}$ of the first principle stress σ_I is determined for each location in the component from the transient stress tensor $\underline{\sigma}(t)$.

$$\sigma_I^{max} = max \left\| \vec{\sigma}_I(t) \right\| \tag{3.1}$$

$$\hat{\sigma}_I^{max} = \frac{\vec{\sigma}_I^{max}}{\sigma_I^{max}} \tag{3.2}$$

Furthermore, as the crack growth rate is a function of the stress intensity amplitude, also the minimum stress value σ_{min} in the same direction as $\hat{\sigma}_I^{max}$ during the cycle is determined (eqn. (3.4)). The stress component acting in the direction $\hat{\sigma}_I^{max}$ can be calculated from the local stress tensor $\underline{\sigma}^j$ using (3.3). A 2D example is shown in Fig. 3.1.

$$\vec{\sigma}_{crack}^j = \underline{\sigma}^j \cdot \hat{\sigma}_I^{max} \tag{3.3}$$

$$\sigma_{min} = min \left\| \underline{\sigma}(t) \cdot \hat{\sigma}_I^{max} \right\| \tag{3.4}$$

A worst case estimate for σ_{min} can be determined by the transient minimum of the third principle stress σ_{III}^{min}.

The stress amplitude is given by

$$\Delta\sigma = \sigma_I^{max} - \sigma_{min} \tag{3.5}$$

The temperature $T_{\frac{da}{dN}}$ for estimating the crack growth rate is chosen as the maximum temperature during the transient analysis (3.6). As in general the temperature

is changing during the cycle, the crack growth rate is expected to be the highest at the highest temperature. This is a conservative estimate for most of the steels for the crack growth rate.

$$T_{\frac{da}{dN}} = max \left\| T\left(t\right) \right\| \tag{3.6}$$

In summary, the simulation does not account for non-mode I crack growth and it is assumed that the crack is always growing in the same direction regardless of the orientation of the stress field. These are reasonable assumptions in the case of rotation symmetric rotor disks, as the first principal stress is governed by the tangential stress and in general this is much larger than the other stress components, at least at the most critical locations.

3.2. Critical Transient Fracture Toughness State

As stated above, in general it is assumed that the crack grows perpendicular to the direction of the transient maximum principle stress σ_I^{max}.

As the failure criterion, as described in chapter 2.4.1, is controlled by the stress and the temperature in a single load step, the transient maximum of equation (3.7) defines the most critical condition regarding the failure criterion.

$$Q\left(t\right) = \frac{\left\| \underline{\sigma}\left(t\right) \cdot \hat{\sigma}_I^{max} \right\|}{K_{Ic}\left(T\left(t\right)\right)} \tag{3.7}$$

As most steels have a pronounced temperature dependence of the fracture toughness including the lower to upper shelf transition, the stress and temperature at this critical point in time is in general not defined by the minimum or maximum of the stress or temperature.

An example for this is shown in Fig. 3.3. The five plots show the time transient development of five different properties at a location in the bulk region (see Fig. 3.2) of a gas turbine disk during start up. Shown are the rotational velocity, the temperature, the stress in direction of the transient maximum first principal stress, the fracture toughness and the ratio of stress and fracture toughness.

An overshoot in the stress occurs due to additional thermal stresses, as the temperature at the surface increases faster than in the bulk. Due to this the surface area expands faster than the bulk, and by this, additional tensile stresses occur in the bulk region.

In the last plot the ratio of stress and fracture toughness is shown, where the transient maximum defines the most critical point in time with respect to the failure

Figure 3.2.: Location in the component of the transient behavior shown in Fig. 3.3. (Figure not to scale.)

criterion. As is shown in this plot, the critical point in time is not necessarily defined by characteristic points in the development of the stress or the fracture toughness.

The critical state for the fracture toughness can also be estimated in a very conservative way by using the maximum stress and the minimum temperature during the cycle.

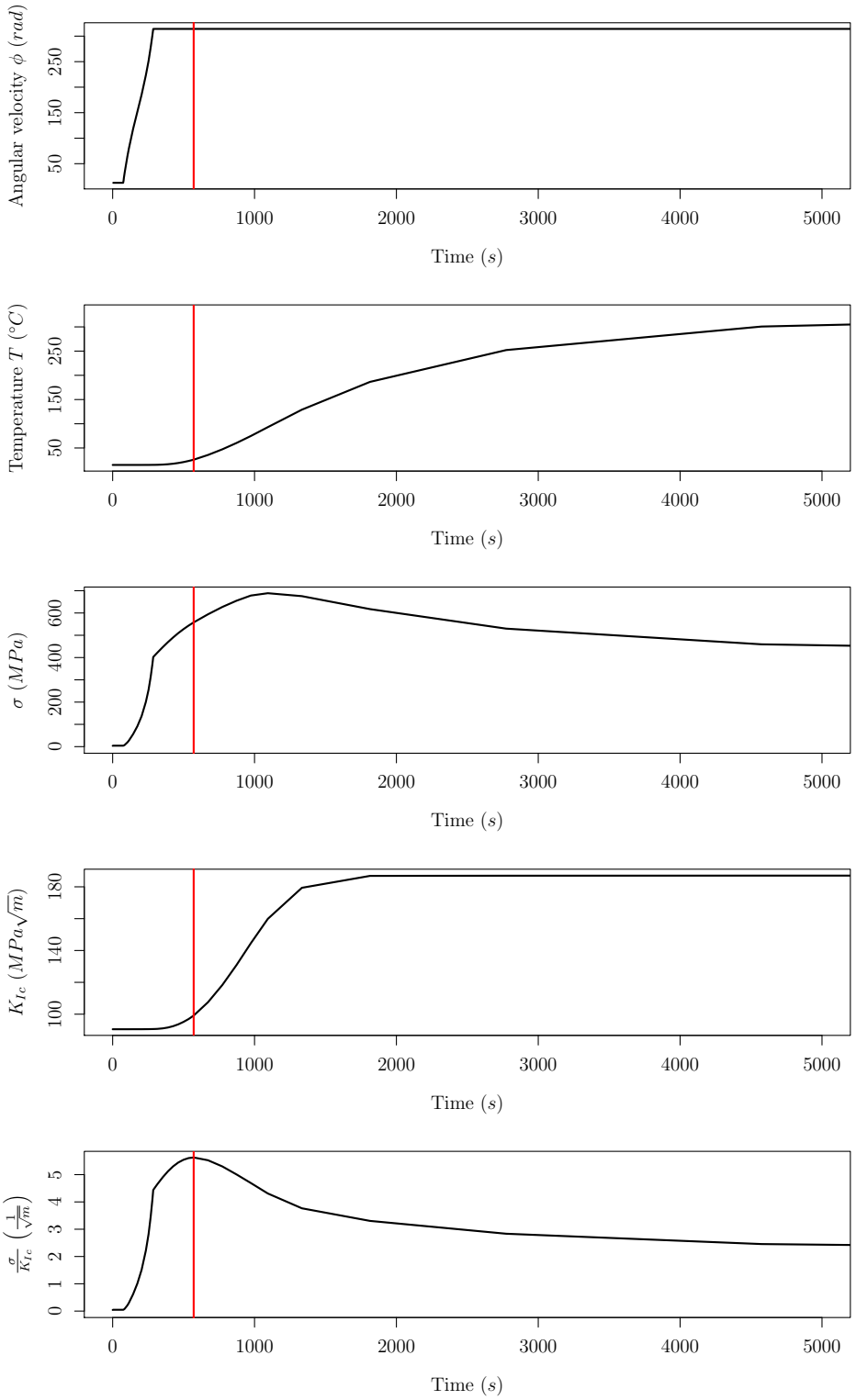

Figure 3.3.: Example of the transient behavior of failure criterion related properties (bulk region) for a typical gas turbine start-up. The critical point for fracture in time is marked by the vertical red line.

3.3. Critical State for Tensile Properties

Two extensions of the linear elastic fracture mechanics, the Irwin plastic zone extension in chapter 2.1.2 and the failure assessment diagram in chapter 2.4.2, have been described. For these advanced methods also the tensile properties of the material are needed to describe plasticity effects beside the fracture toughness and the crack growth rate.

As the tensile properties are temperature dependent, a critical temperature state in the time transient has to be defined. *ProbFM* contains two different assessment possibilities. The first uses the temperature for the tensile properties which has been determined for the critical state of the fracture toughness. This accounts for the mechanical load which can be withstood by the component at this critical point in time.

The second uses the maximum temperature during the transient cycle. This approach is in general more conservative than the first one as the elastic properties become typically worse at higher temperatures.

4. ProbFM Code Structure

So far different realization approaches for the probabilistic fracture mechanics assessment have been evaluated. Namely, these have been the already existing probabilistic fracture mechanics code DARWIN and in-house developed codes in the statistical interpreter language R and in the compiler language C/C++. The reasons for not using the commercial tool DARWIN have already been mentioned in the introduction (chapter 1).

In the early development phase, two codes have been developed in parallel in R and C/C++. R has good graphical and statistical implemented libraries which simplify the statistical modeling and the display of the results. As a drawback, R is an interpreter language and depending on the mathematical problem, the calculation time can be significantly larger than the calculation time of an optimized C/C++ code. The advantage of C/C++ is the fast calculation time as the code is compiled into machine language and its use on high-performance multi-core computer architecture.

In the further development of the code it became obvious that for the problem at hand R is significantly slower than C/C++. The integration of the differential equation in C/C++ is approximately two orders of magnitude faster than in R. Therefore, the code development in R has been stopped and the R code has only been used for cross checking of modules of the C/C++ code.

The *ProbFM* code has been developed by Kai Kadau in the compiler language C. Message passing interface (MPI) is utilized to ensure massive parallelization which is needed to speed up calculation significantly. *ProbFM* is implemented following a modular concept. The main modules are shown in Fig. 4.1. The main advantage is that single modules can be exchanged easily, e.g. the FM module can be chosen that it accounts for different fracture mechanics models, like linear elastic fracture mechanics, Irwin plastic zone extension or failure assessment diagram.

The user has to define an input deck using the I/O device. This input deck is interpreted by the I/O module which provides the inputs for the computation, the FEA and fracture mechanics module. These modules access different libraries according to the definitions in the input deck. The FEA module interprets the stress, temperature and location information and maps this information on a regular grid. This information is then passed to the fracture mechanics module. The computation module carries out the probabilistic calculations. It generates random sets of input param-

eters for the Fracture Mechanics module and calculates the PoF from the fracture mechanics calculation which is done by the Fracture Mechanics module.

All this information is gathered again in the I/O module which passes the information back to the I/O device which displays the results.

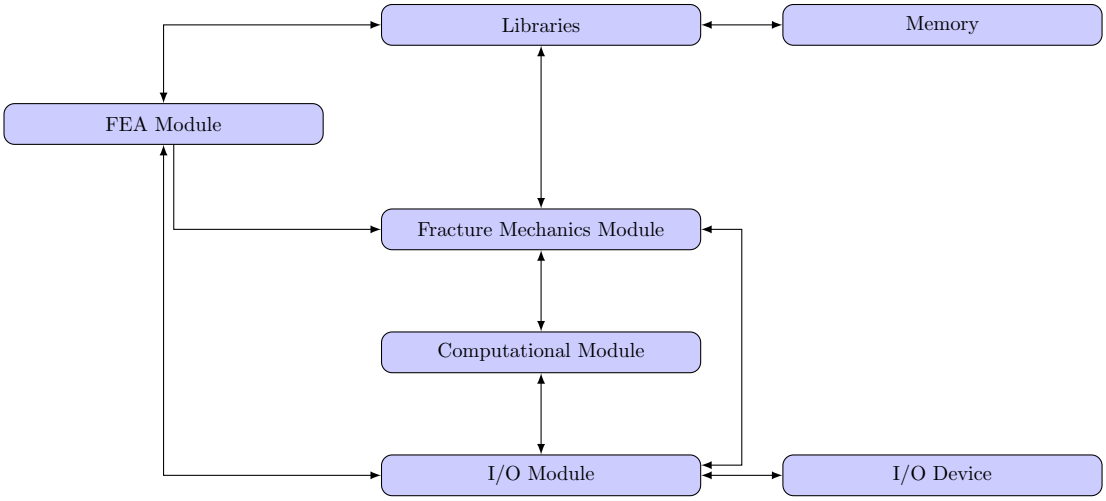

Figure 4.1.: Computational module flowchart of *ProbFM*

One example of a possible calculation loop is shown in Fig. 4.2. In the first step, the material properties data and the temperature and stress information is used to calculate critical transient state maps which contain the critical stresses for the failure criterion and fatigue crack growth calculation.

In parallel, from the NDE related input, KSR limit value, KSR size distribution, the probability of detection and the conversion factor distribution, the initial flaw size distribution is calculated following the process shown in Fig. 2.29.

In addition to the TFS distribution, a crack shape distribution with the $\frac{a}{c}$ values is loaded. Currently, the information about the crack shape is very limited. Therefore, it is assumed that the crack shape is uniformly distributed and independent from the location in the component and from the size of the flaw. In future, this might be changed if more information about the crack shape distribution is available and correlations with the size and the location might be found.

With this information the simulation is started by choosing randomly a position in the component. From the critical transient state map the stresses and temperatures at this location are obtained. With the stress and temperature information random material properties, flaw sizes and shapes are drawn from the distributions. Then the

crack growth is calculated up to the defined number of cycles. If the stress intensity reaches a critical value within the number of cycles the crack is counted as failed. The number of failed cracks S_f and the PoF is proportional to the ratio of the total number of samples S and the number of failed cracks S_f.

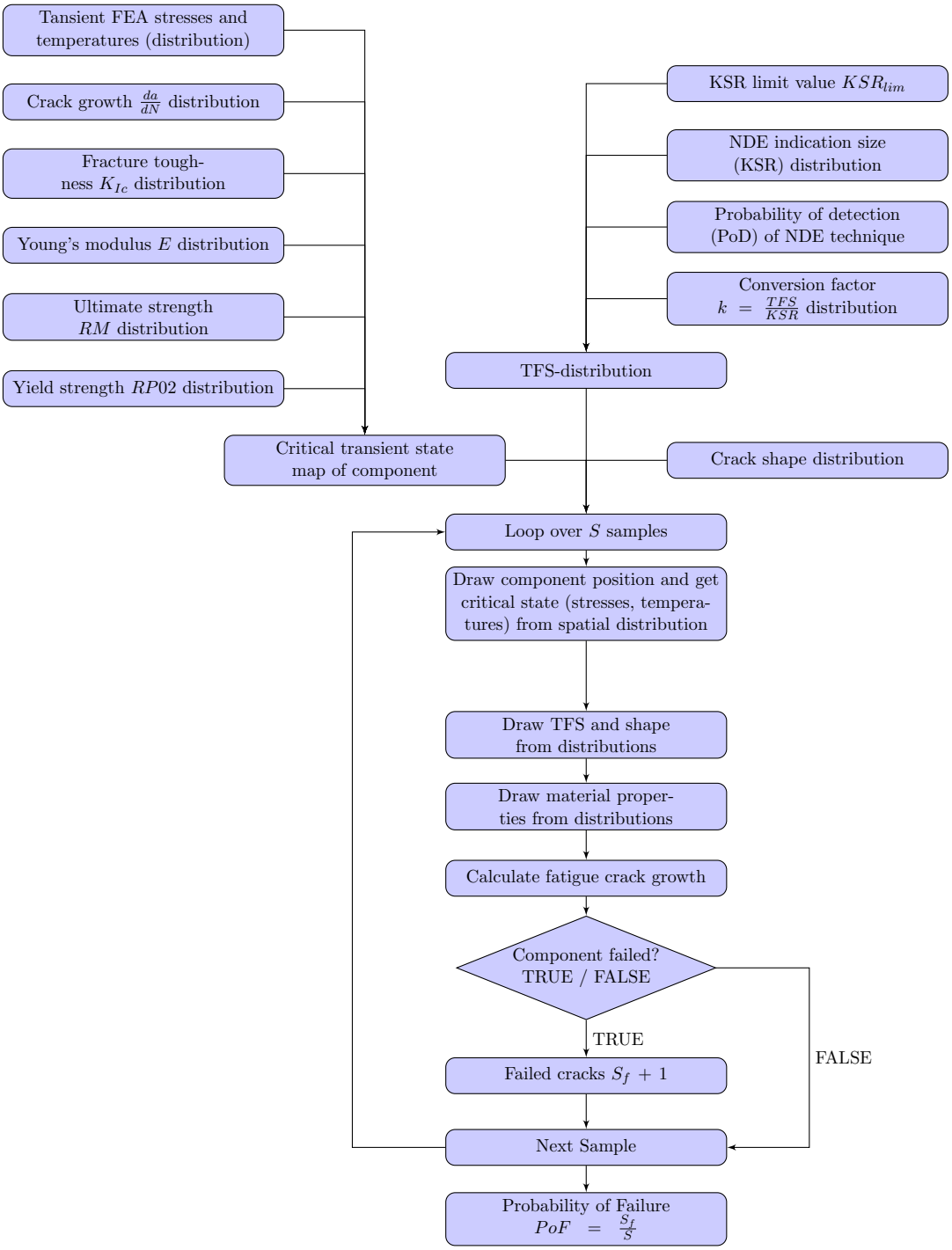

Figure 4.2.: Logical data Flowchart of *ProbFM*

4.1. High speed look up tables

To enable very fast access to functions that are evaluated over and over again, the functions are stored in high speed look-up tables. High speed look-up tables are well known in the high performance computation community and they are used to describe complex functions $y = f(x)$ where x_i, y_i and f can be scalar or a vector. The basis of a high speed look-up table is a fine spaced regular grid with a known grid distance Δx, the minimum / maximum x values and the function value y.

In case of a one dimensional function $f(x)$, the look-up table consists of one column containing the corresponding function values y. In order to speed up things even faster the local derivative can be pre-calculated as well so that the equation for evaluation reduces to:

$$\left.\begin{aligned} i &= int\left(\frac{x - x_0}{\Delta x}\right) \\ f(x) &\approx table[i] + table_{dx}[i](x - x_0 - i\Delta x) \end{aligned}\right\} x_0 \leq x \leq x_{max} \tag{4.1}$$

This one dimensional scheme can be augmented to the needed number of dimensions. If a complex function has to be evaluated very often in a limited, known area this look-up table approach can speed up the calculation time by several orders of magnitude, compared to the calculation of the function itself, depending on the complexity of the function which has to be evaluated. *ProbFM* uses these scheme for up to 3 dimensions.

4.2. Scaling behavior of Multi-core Calculations

As each single crack calculation in the Monte Carlo simulation is independent of each other, it is possible to perform these calculations in parallel on multiple CPUs with only a limited amount of communication. *ProbFM* can be used in a multi-core mode. Strong- and weak-scaling has been measured on the Siemens Grid Engine (SGE). The weak scaling has also been measured on a Workstation with up to 10 CPUs.

In Figure 4.3b the weak scaling measurements are shown. With the used test case, the multi-core calculation becomes faster between 10^5 and 10^6 samples but the ideal speed up is not reached until 10^7 samples. The ideal speed up s_{ideal} and the speed up s are given by

$$s_{ideal} = \frac{N_{CPU}}{N_{CPUref}} \tag{4.2}$$

$$s = \frac{t_{ref}}{t} \tag{4.3}$$

.

N_{CPUref} is the number of used CPUs and t_{ref} is the CPU time needed for a reference calculation. N_{CPU} is the number of CPUs used in the calculation to compare and t is the CPU time needed.

The example shows that starting at $10^6 - 10^7$ samples per CPU a parallel processing is efficient. For a smaller number of samples per CPU, the overhead to distribute the samples and collect the results is larger than the gained speed up.

The same test case has been used to measure the strong scaling on the SGE (Figure 4.3a). Up to ≈100, CPUs *ProbFM* scales almost linearly with the number of used CPUs on the SGE. With more CPUs, the speed up reduces compared to the ideal speed up, but it is still significant.

With the multi-core option of the *ProbFM* code a typical gas turbine disk design assessment can be performed in less than one hour on 12 CPUs of SGE. Alternatively, the same calculation can be performed in a couple of minutes if more CPUs are used.

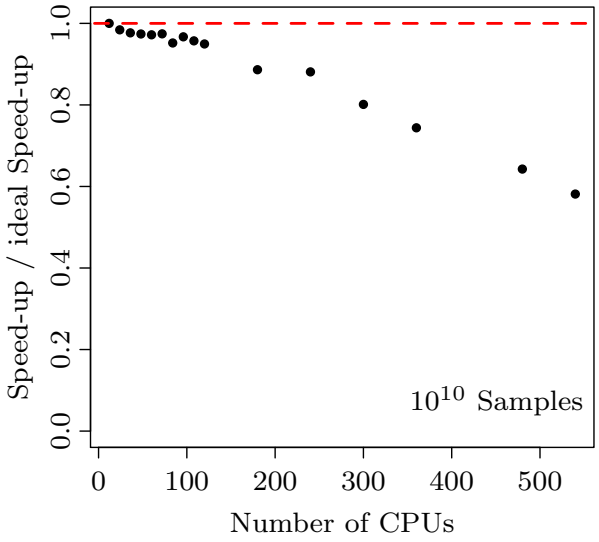

(a) Strong scaling

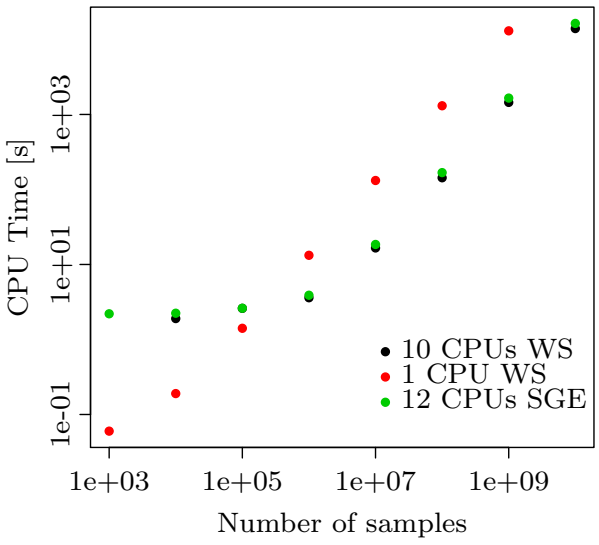

(b) Weak scaling

Figure 4.3.: *ProbFM* multi-core scaling behavior.

5. Probability of Failure and Risk Assessment

To calculate the PoF, *ProbFM* configures S samples representing a fleet of components in the field by drawing location in the component, crack size (TFS_{acc}), shape ($\frac{a}{c}$), and a random set of material properties (K_{Ic}, $\frac{da}{dN}$, σ_{YS}, σ_{US}, E) according to the local stress and temperature conditions from the Respective distributions. With this set of values, deterministic fatigue crack growth is calculated to the desired number of cycles N. If the stress intensity reaches the fracture toughness K_{Ic} or the load parameter reaches plastic collapse according to the failure assessment diagram, a failure is predicted. The probability of failure is calculated as the ratio of the samples failed S_{failed} within N Cycles and the total number of samples S of the Monte Carlo Simulation. This is a Direct Simulation MC scheme (Fig. 5.1), as no approximations to the MC scheme itself are applied. This approach will always converge to the right answer within the scope of the model.

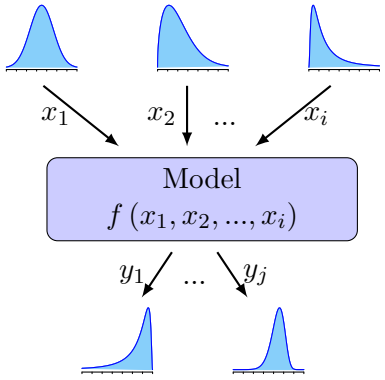

Figure 5.1.: Principle of a Direct Simulation Monte Carlo scheme

$$PoF(N) = \frac{S_{failed}}{S} \tag{5.1}$$

The hazard rate H can be calculated from the PoF by equation (5.2). It is a measure for the probability of failure within the next cycle under the condition that no failure has occurred before. For small PoF values, the hazard rate is approximately

the derivative of the PoF. In case of a numeric simulation the Hazard rate can be estimated by equation (5.3).

$$H(N) = \frac{\frac{\delta PoF}{\delta N}}{1 - PoF(N)} \tag{5.2}$$

$$H(N + \Delta N) = \frac{\frac{PoF(N+\Delta N) - PoF(N)}{\Delta N}}{1 - PoF(N)} \tag{5.3}$$

To make use of the probabilistic results in a design process, an acceptable risk limit has to be defined. The acceptable risk limit can be defined for instance on the basis of an ISO standard [2] and specifications from the Nuclear Regulatory Commission (NRC) [10] for the acceptable risk for steam turbines in nuclear power plants. In the latter case the acceptable annual risk for turbo machinery rotors is 10^{-5} - 10^{-4} per year depending on the orientation of the rotor with respect to the nuclear reactor. To distribute a legally acceptable risk of 10^{-4} for the whole rotor evenly to all rotor forgings, the acceptable risk limit is divided by the number of forgings. For example, for a rotor with 20 forgings, the acceptable risk limit per forging is $5 \cdot 10^{-6}$ per year and disk. This is a conservative assessment, as in general only few disks are critical and contribute significantly to the risk.

As the legally acceptable risk is defined on a per year basis but the failure mechanism is cycle controlled, the way how the engine is operated has a considerable impact to the operational lifetime of the components. The annual risk per component can be calculated from the hazard rate by assuming a specific number of starts per year s_{year} (typically between 12-365 starts per year).

$$t_{oper} = \frac{N}{s_{year}} \tag{5.4}$$

$$H_{year}(t_{oper}) = \int_{t_{oper} - \frac{1}{s_{year}}}^{t_{oper}} H(t)\, \delta t \tag{5.5}$$

Here N is the total number of starts, s_{year} the number of starts per year, H_{year} the annual risk and H the Hazard rate.

At this point it should be stated that the safe life approach as it is assumed by the deterministic approach does not truly exist. In the deterministic approach some type of statistic input is used as the material data and the used conversion factors are not true worst case assumptions. The material design curve is described for instance by a one to three sigma curve. Assuming a two sigma curve there is still a probability

of 2.275% that there are values below this curve. The same is true for the conversion factor distribution as shown in section 2.8.1. Assuming the data published by [29] are Gamma distributed, there is still a probability of 19.16% of underestimating the flaw size if a conversion factor of 2 is used in the deterministic assessment as recommended by [29]. Due to these reasons, even components with a long deterministic life have a finite risk of failure (Figure 5.2). These calculations have been done using only the real measured material data and not the fitted distribution functions. Since some failures can even occur at the first cycle a deterministic calculation would predict zero life if truly all worst case assumptions would be accounted for, even without any applied design factor.

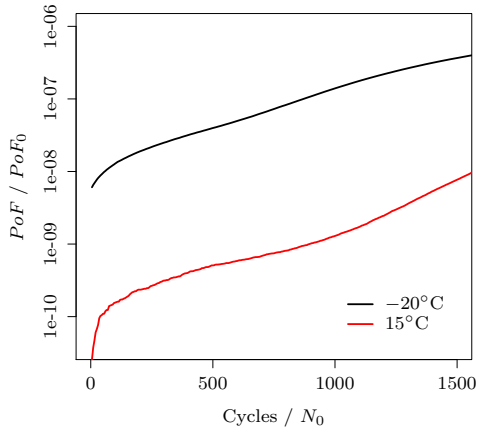

(a) PoF of Low risk component for a $-20°C$ cold start and an ISO start

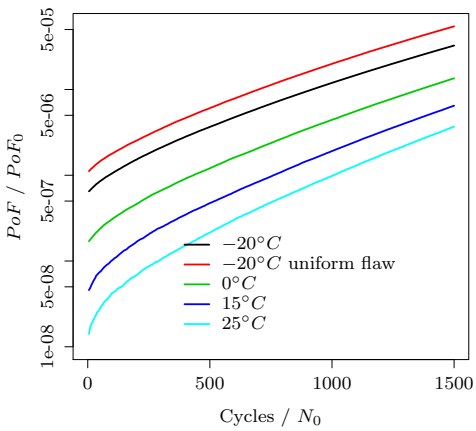

(b) PoF of Medium risk component for several different start temperatures

Figure 5.2.: The PoF curves for of the two components show that even in the first cycle a failure is possible.

Depending on the amount of available information for a specific component, the PoF can change significantly. Therefore, in the following subsections three different risk assessment conditions are described.

- design risk assessment
- component without indication risk assessment
- component with indication risk assessment

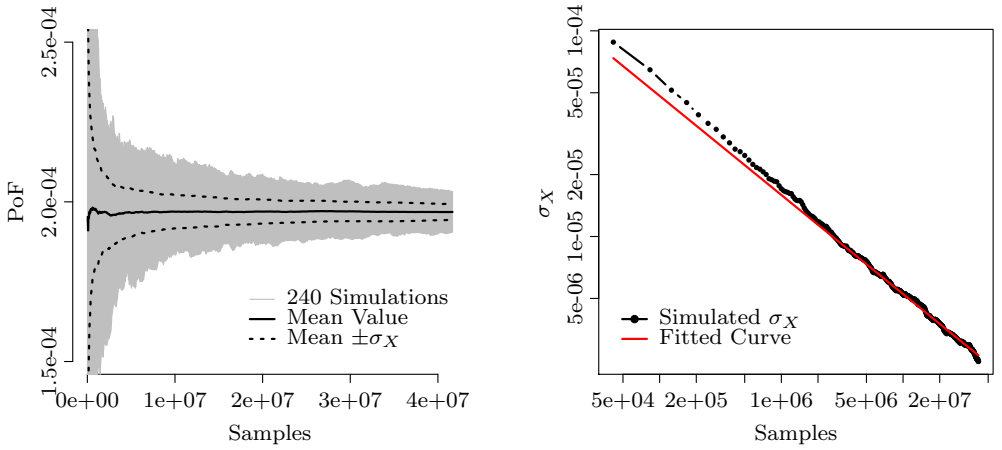

(a) *PoF* convergence as function of samples (b) Standard deviation vs. # of samples

Figure 5.3.: Convergence behavior of the MC simulation as function of the number of samples

5.1. Convergence of Probabilistic Fracture Mechanics Simulation

As for all types of simulations, one measure of the convergence of the simulated result is needed to get an information on the reliability of the simulation. In case of Monte Carlo simulations, a measure for the error in the simulation is the standard deviation of the result. It is well known that in case of brute force Monte Carlo methods, the standard deviation σ_X of the result scales with the square root of the number of samples S

$$\sigma_X \propto \frac{1}{\sqrt{S}} \tag{5.6}$$

.

In Fig. 5.3 the convergence behavior of a simulation is shown. 240 separate realizations with different random seeds have been performed, and the PoF and the standard deviation σ_X of the calculated $PoFs$ after a specific number of cycles have been plotted as function of the number of simulated samples S.

For the example shown in Fig. 5.3, the standard deviation of the PoF calculated

with $4.17 \cdot 10^7$ samples can be estimated as $\sigma_{X_{est}} = 2.47 \cdot 10^{-6}$. In Fig. 5.3b it is shown that the standard deviation scales linearly with the root of the number of samples. Using eqn. (5.6), the standard deviation of the mean PoF of all 240 Simulations (10^{10} samples) can be calculated as $\sigma_{X_{ext}} = 1.88 \cdot 10^{-7}$.

The extrapolation approach can be used to stop the simulation after a desired accuracy of the simulation has been reached instead of calculating a fixed number of samples. This has not been implemented to *ProbFM* yet.

Of course the convergence of a simulation depends on the specific problem and on the number of cycles for which the PoF is calculated, as for small cycle numbers the PoF is smaller and following more samples are needed to reach convergence. Typically noise well below the acceptable risk limit is of no practical interest.

5.2. Design Risk Assessment

In the following some ultrasonic specific notations are used, which are described here for a better understanding and shown in Fig. 5.4. From a probabilistic fracture mechanics point of view there are three sizes which are important.

- Decision limit KSR_{dec}
- Noise threshold KSR_{th}
- Flaw size KSR

Depending on the outcome of an ultrasonic inspection of a component, one of these values will be used for the probabilistic fracture mechanics calculation. KSR_{dec} is used during a design calculation and describes a permissible flaw size and is in general defined in a contract with a forgery. If a flaw is detected, which exceeds the permissible flaw size, the customer has the opportunity to reject the forging. KSR_{th} is used during the analysis of a component without indication and is defined by the detection limit of the ultrasonic system. The flaw size KSR is used in the case a flaw has been found during a the ultrasonic inspection.

During the component design phase information about the flaw distribution of a specific component is limited. Thus, the KSR_{lim} value in the ultrasonic flowchart 2.29 can be set to the deterministic decision limit KSR_{dec}. This can be for instance an indication size limit for the rejection of components from a forgery. The KSR_{dec} value used in the deterministic assessment is in general larger than the noise threshold KSR_{th} of the ultrasonic measurement. This implies that the calculated design PoF is higher than the PoF of a specific component, which has been reviewed by ultrasonic

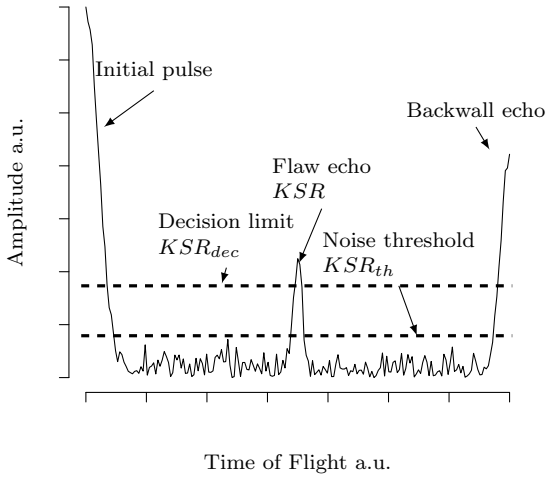

Figure 5.4.: Principle definition of the decision limit, the noise threshold and the flaw size as used in the probabilistic simulation.

without finding an indication (Fig. 5.5). On the other side a component containing an indication can yield a higher PoF, as shown in Fig. 5.8, depending on the size and the location of the flaw in the component. This latter case always requires a re-qualification of the component (either probabilistic or deterministic).

5.3. Risk Assessment of a Component without Ultrasonic Indication

If a specific component has been examined by means of ultrasonic and no indication has been found, the PoF of this component is reduced compared to the design risk as shown in Fig. 5.5. The probability of failure is reduced, as the amount of possible flaws and the size of these is reduced compared to the design risk analysis. The PoF is reduced due to the fact, that the noise threshold KSR_{th} is smaller than the KSR_{dec} value, as shown in Fig. 5.4. If for a specific component no flaw has been detected, the KSR_{lim} value in the simulation can be reduced to the KSR_{th} values as no KSR value up to this size has been observed. Due to this reduced maximum observable KSR size, the clean scan PoF is reduced as shown in Fig. 5.5. For typical gas turbine

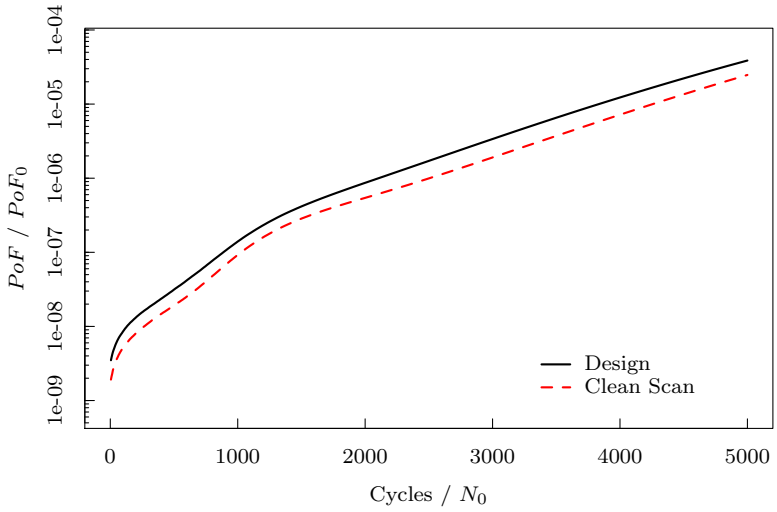

Figure 5.5.: Design and clean scan PoF of a turbine disk

disk designs, the design PoF is approximately two times the clean scan PoF_{no_ind}.

In comparison to the design assessment described in section 5.2, the assessment using the KSR_{th} value as limiting value assumes some knowledge of a clean scan of a component which has been examined by ultrasonic. This application is limited as typically a design calculation has already qualified the design.

5.4. Risk Assessment of a Component with Ultrasonic Indication

The PoF calculated on basis of the KSR database assumes there is no knowledge about KSR indications of a specific forging. If a particular indication has been found in a component, the PoF of this component can be calculated separately using the KSR size, location of the indication and the assumption that the ultrasonic indication is already a sharp crack. Depending on the local stress field and the size of the indication, the PoF of this particular component PoF_{comp} can be different than the PoF based on the KSR database. However, the average risk of the findings should be equal to the design risk since otherwise the assumed KSR distribution is incorrect.

Some examples for risk assessments of a component with an ultrasonic indication

with the same boundary conditions as for the calculations (−20°C, 0°C, 15°C) given in Figure 5.2b are shown in Figure 5.6b and 5.7b.

To calculate the PoF of a single flaw PoF_{ind}, the *ProbFM* ultrasonic inputs have to be changed compared to those in chapter 5.2.

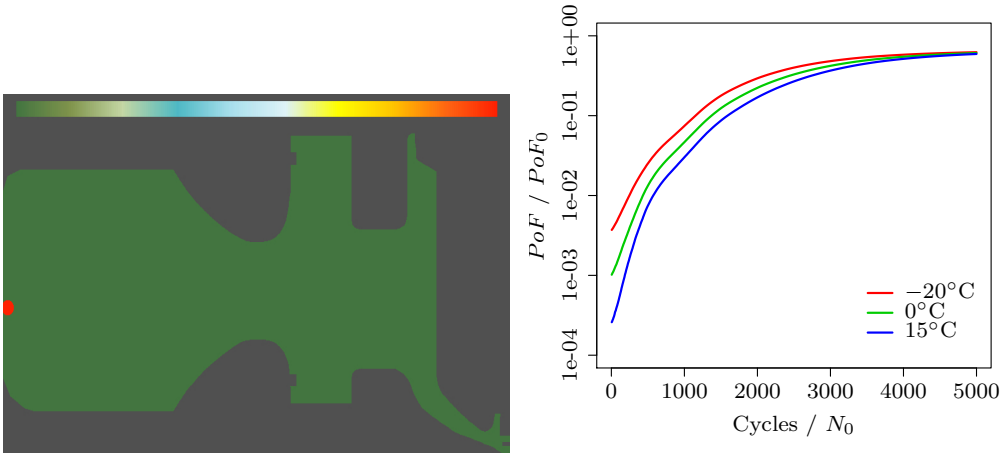

(a) Indication Location in the hub region . (Figure not to scale.)

(b) Indication PoFs

Figure 5.6.: PoF of an example rotor disk at different material temperatures with an ultrasonic indication of size $KSR = 2$mm in the hub region.

A disk with an ultrasonic indication can contain other flaws which have not been detected. A conservative estimate of the total PoF of a component PoF_{comp} with ultrasonic indication is given by equation 5.7.

$$\begin{aligned} PoF_{comp} &= 1 - ((1 - PoF_{no\_ind})\,(1 - PoF_{ind})) \\ &\underset{PoF<<1}{\approx} PoF_{no\_ind} + PoF_{ind} \end{aligned} \tag{5.7}$$

An example for the combined PoF_{comp} of a component with an ultrasonic indication in the middle as shown in the Figure 5.7 is given in Figure 5.8. The combined PoF_{comp} for the component with the hub indication is not shown as it is completely determined by the single flaw risk shown in Figure 5.6.

The single indication assessments shown in this chapter are examples of very rare occurring indications especially in the hub region. As shown in the failure rate map in

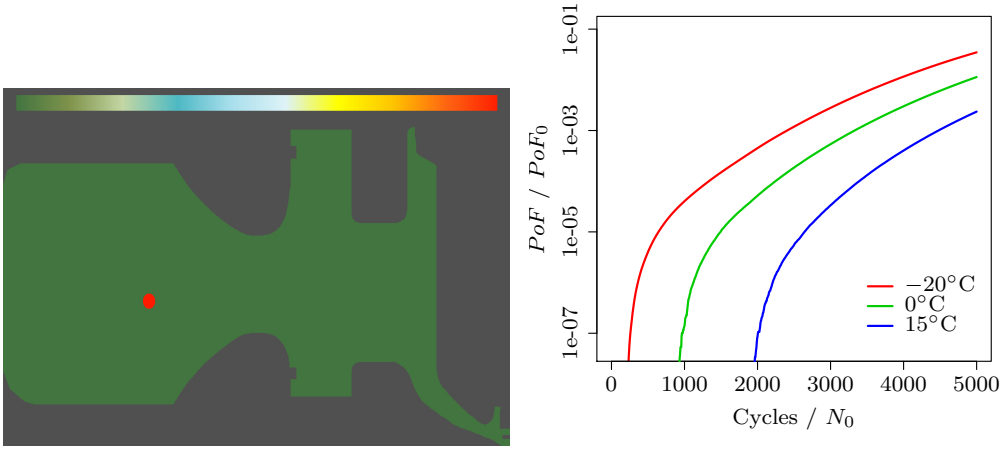

(a) Indication Location in the bulk region . (Figure not to scale.)

(b) Indication PoFs

Figure 5.7.: PoF of an example component at different material temperatures with an ultrasonic indication of size $KSR = 2$mm in the bulk region.

Fig. A.10, the area where the indication is located in the hub region is very critical. On the other side the volume at this location is small compared to other locations, as it is located at the inner radius of the component. Following the occurrence probability of such a flaw is very small. The indication in the bulk area is somewhat more likely but it is by far not as critical as the one in the hub region. In case of the $15°C$ assessment, it does not change the PoF up to Cycles/$q_{cycle} = 1500$ compared to the clean scan PoF. Thus, for most locations and crack sizes, $PoF_{comp} \leq PoF_{design}$ for the number of cycles of interest.

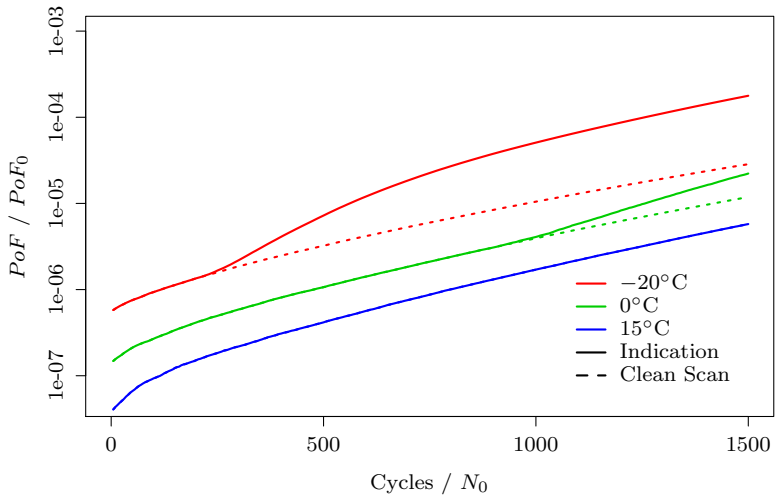

Figure 5.8.: Conservative estimate of the combined PoF of an example component with an ultrasonic indication in the bulk region.

6. Probabilistic and deterministic component life assessment discussion for simplified rotor components

The probabilistic assessment requires a mindset change of the engineer who is performing the assessment because the result of probabilistic analysis is no longer a yes or no answer as it is the case for the deterministic analysis. In the following the results of a deterministic design assessment is called the deterministic life. In the following a comparison between deterministic and probabilistic results is presented. The results presented have been calculated using the linear elastic fracture mechanics module within the developed $ProbFM$ tool.

In a typical deterministic design assessment additional safety factors are applied, for instance the component lifetime is reduced to 67% calculated lifetime. Such safety factors can change and / or reduce the correlation between a deterministic and a probabilistic analysis. For this reason no safety factors are applied in the deterministic calculations presented in this work. To protect Siemens proprietary information an artificial steel material (described in chapter 6.1) and simple geometry components have been developed and utilized for the comparison.

The NASGRO stress intensity factor solutions for elliptical embedded and semi elliptical surface cracks, as described in chapter 2.3.3, and the crack transition model as described in chapter 2.6.3 have been used for the calculations.

The NDE process in case of the design analysis is modeled by the PoD pod-1.5_b as shown in Fig. 2.23, the KSR flaw size distribution as shown in Fig. 2.24, the radial distribution as shown in Fig. 2.25, the conversion factor distribution as published by [29] shown in Fig. 2.21 and $KSR_{lim} = 2mm$.

The $\frac{a}{c}$ ratio is set to be a uniform distribution from 0.2 to 0.5 for the probabilistic assessment.

For the probabilistic single crack assessment it is assumed that a single indication of size $KSR = 2mm$ has been observed.

In order to perform a deterministic analysis with the $ProbFM$ tool the following distributions have been set to single values as follows:

In the deterministic component assessment the NDE process is described by a constant conversion factor $k = 2$ as suggested by [8] and [29] and a KSR flaw size which

is equal the $KSR_{lim} = 2mm$ used in the probabilistic assessment.

For all components a design PoF, single indication PoF and the deterministic life has been calculated. The single indication PoF has been calculated assuming the same KSR size and flaw location as within the deterministic analysis. The PoD is set equal to 1, thus all possible flaws are detected.

6.1. Generic Steel Material

A generic steel material used for the calculation is derived from a high alloyed Cr-Steel, which shows a significant change in the fracture toughness with a transition from brittle to ductile failure mechanism in the operational temperature range of a gas turbine (Fig. 6.1). As the comparison in the following is based on linear elastic fracture mechanics calculations, without failure assessment diagram, only the fracture toughness and an example of the crack growth rate are needed as presented in figures 6.1 and 6.2.

Fig. 6.1 shows the temperature dependence of the fracture toughness and the -2σ value at $15°C$ which is used for the deterministic analysis. As shown there the fracture toughness changes up to $\approx 150°C$ and stays constant thereafter up to the operational temperature limit.

The crack growth rate model used in this assessment is a NASGRO type model as described in 2.7.4, with an exponent $q = 0$. In Fig. 6.2 the crack growth rate at $15°C$ for different R ratios is shown. As $q = 0$ at high ΔK values no divergence of the crack growth rate occurs.

In the deterministic assessment the -2σ quantile of the fracture toughness and for the crack growth rate the $+2\sigma$ quantile at $15°C$ is used, as the deterministic assessment is only presented for an isothermal example. In a deterministic assessment, it is common to use a certain quantile, for instance $\pm 2\sigma$ quantiles, thus the shown comparison depicts a typical situation for a deterministic assessment.

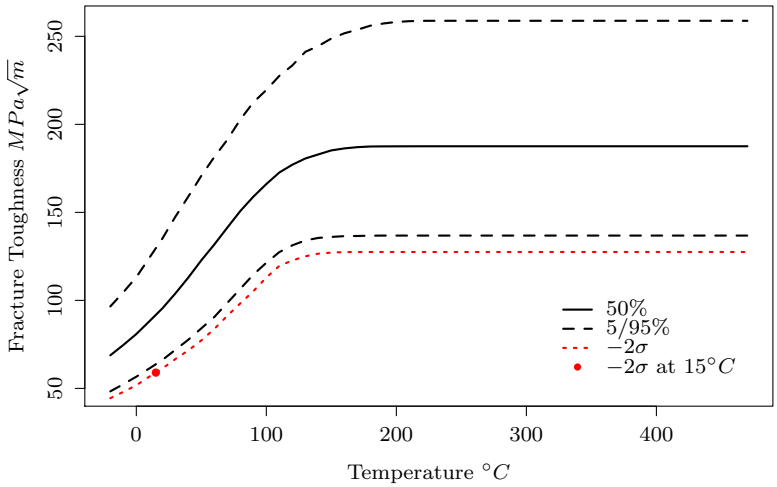

Figure 6.1.: Generic fracture toughness model as used for comparison of deterministic and probabilistic assessments.

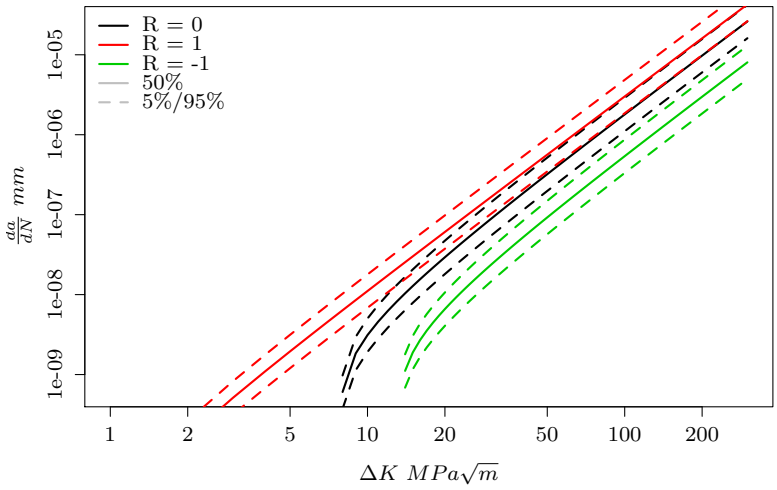

Figure 6.2.: Generic crack growth rate model as used for comparison of deterministic and probabilistic assessments at $15°C$ for different R ratios.

6.2. Assessment of simplified Rotor Components

In the following six simple component geometries have been assessed by deterministic and probabilistic methods. The assessed components are rotating cylindrical disks with a central hole. The tangential stress σ_{tan} in the rotating disks can be calculated by (6.1) which is well known in the literature [21]. The describing parameters outer radius R_o, inner radius R_i, thickness t, density ρ, poisson ratio ν, rotational frequency f for the tangential stress calculation (6.1) are given in Tab. 6.1. r is the radial position in the disk, measured from the rotational axis.

$$\sigma_{tan}(r) = \frac{3+\nu}{8}\,\rho\,(2\,\pi\,f)^2\,\left(R_o^2 + R_i^2 + \frac{R_o^2\,R_i^2}{r^2} - \frac{1-3\,\nu}{3+\nu}\,r^2\right) \tag{6.1}$$

A similar expression for the radial stress can be given (6.2).

$$\sigma_{rad}(r) = \frac{3+\nu}{8}\,\rho\,(2\,\pi\,f)^2\,\left(R_i^2 + R_o^2 - \frac{R_i^2\,R_o^2}{r^2} - r^2\right) \tag{6.2}$$

In Fig. 6.4 the radial and tangential stresses are shown for an arbitrary disk with center hole are depicted. The radial stress is always smaller than the tangential stress. As the first principal stress controls the crack growth for the simple components the calculations are based on the tangential stress field.

In case of the deterministic assessment, a semi elliptic surface crack at the inner radius at the middle of axial direction is assumed as indicated in Fig. 6.5, with the parameters as described in the introduction of chapter 6.

The tangential stress fields in the components, as calculated by equation (6.1), are graphically shown in Fig. 6.5. This plot shows that the high stressed area in a rotating

Parameter	Value
R_o	1m
R_i	0.15m, 0.3m, 0.5m
t	0.15m, 0.9m
ρ	$7820\frac{\mathrm{kg}}{\mathrm{m}^3}$
ν	0.3
f	50Hz

Table 6.1.: Input parameters for analytic stress field calculation

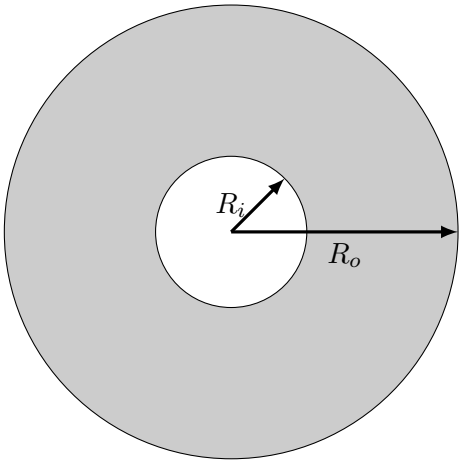

Figure 6.3.: Definition of the geometry of the assessed components.

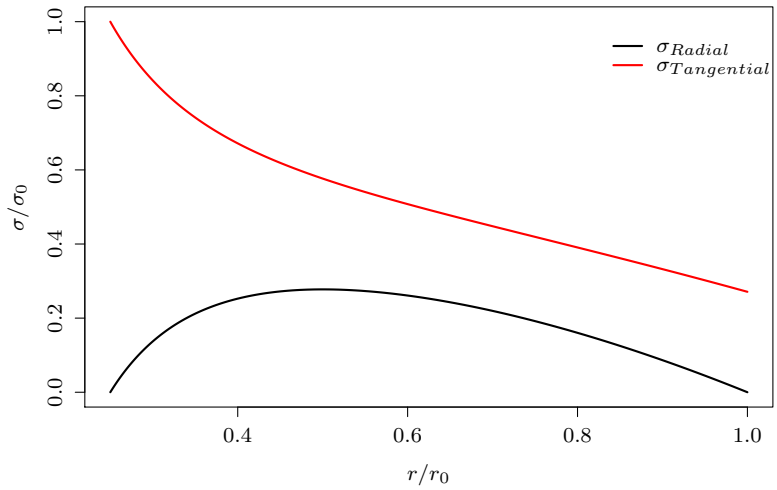

Figure 6.4.: Stress distribution in a rotating ring according to equations (6.1) and (6.2)

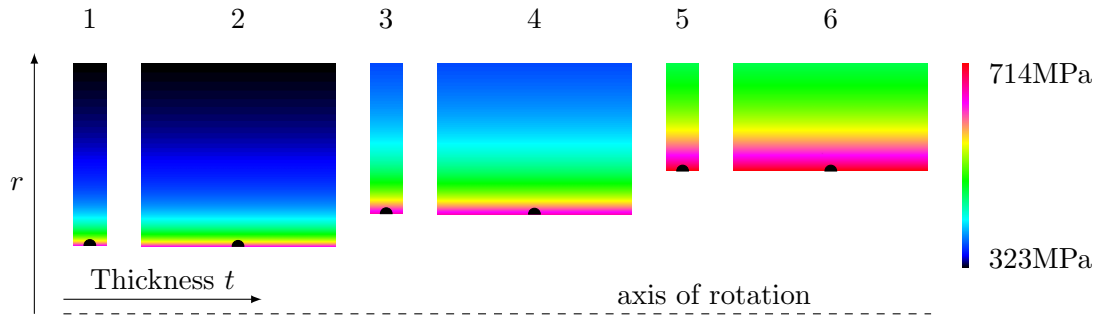

Figure 6.5.: Axis-symmetric representation of the tangential stress field for the six example components. For the single indication and the deterministic analysis the location of the assumed single indication is shown by the unproportional large black semi ellipse.

disk with a central hole increases with increasing inner diameter, if the outer diameter stays constant. The position of the indication for the probabilistic single crack and deterministic assessment is shown. Table 6.2 shows the stress values σ_{max} at the inner diameter. It can be seen that the highest stress in the components increases with increasing inner diameter if the outer diameter stays constant.

Besides the maximum stress the table contains the inner radius R_i, outer radius R_o, thickness t, volume V and deterministic life N_{det} of the component. Furthermore the design and single indication $PoFs$ at the deterministic predicted life are shown.

The deterministic life is the number of cycles after the maximum stress intensity in front of the crack becomes larger or equal than the fracture toughness.

6.2.1. Deterministic - Probabilistic results correlation

The risk at the deterministic design life is not known and varies from design to design and type of operation. This is related to the fact that the deterministic life calculation is done only at a single or few locations in the component with high failure risk (e.g. high stressed locations) and no information about the material and flaw variation is taken into account. Furthermore, the deterministic life is the minimum of this calculated cycle numbers.

In the probabilistic design assessment, the PoF is an integral description of the whole component. Therefore, the PoF is influenced by the whole stress field in the component and not only by a single stress value. In contrast to the design PoF, the local failure rate density and the single indication PoF have a stronger correlation to

Comp.	R_i m	R_o m	t m	V m^3	σ_{max} MPa	N_{det}	$PoF\,(@N_{det})$ Design	$PoF\,(@N_{det})$ Indication
1	0.15	1	0.15	0.921	643.6	3920	$2.59\,10^{-7}$	$5.41\,10^{-4}$
2	0.15	1	0.9	5.527	643.6	3920	$1.34\,10^{-6}$	$5.41\,10^{-4}$
3	0.3	1	0.15	0.858	664.5	3130	$2.96\,10^{-7}$	$5.58\,10^{-4}$
4	0.3	1	0.9	5.146	664.5	3130	$1.37\,10^{-6}$	$5.58\,10^{-4}$
5	0.5	1	0.15	0.707	713.9	1730	$3.83\,10^{-7}$	$5.97\,10^{-4}$
6	0.5	1	0.9	4.241	713.9	1730	$6.2\,10^{-6}$	$5.97\,10^{-4}$

Table 6.2.: Comparison of the deterministic life N_{det} and $PoF(N_{det})$ for a probabilistic design and single indication analysis.

the deterministic calculated life which is calculated at the same location.

In the probabilistic design analysis, the PoF is calculated as an integral over the whole component. Here surface effects, such as crack growth acceleration and / or transitions from embedded to surface cracks have to be accounted for. These effects further weaken the correlation between the design PoF and the deterministic calculated life.

Effects like these are not accounted for in the deterministic life calculation of technical components, as in general each flaw is assumed to be a surface crack.

As shown in Tab. 6.2 and Fig. 6.6 the deterministic calculated life N_{det} has a strong correlation to the PoF of the probabilistic single indication analysis. This is expected, as both assessments assume a crack at the same location.

In contradiction to this, the PoF of the probabilistic design analysis has no direct correlation to N_{det} as shown in Tab. 6.2 and Fig. 6.7, the risk at the deterministic design life can vary by more than an order of magnitude.

The reason for the weak correlation between N_{det} and the design PoF is that the design PoF is evaluated as an integral over the whole component and no specific location and flaw size are assumed within the calculation. In contradiction to this the deterministic analysis utilizes only a specific location and a certain flaw size. There are two effects which are not accounted for in a deterministic analysis: The size effect, as the flaw occurrence rate is proportional to the total volume of the component, as described in chapter 2.8.3, i.e. a larger component with the same stress distribution has a higher risk. Another effect is the surface effect. Cracks which are close to a surface can transition into a surface flaw (chapter 2.6.3) and experience an increased stress intensity at the surface pointing crack tip as well as an area increase during

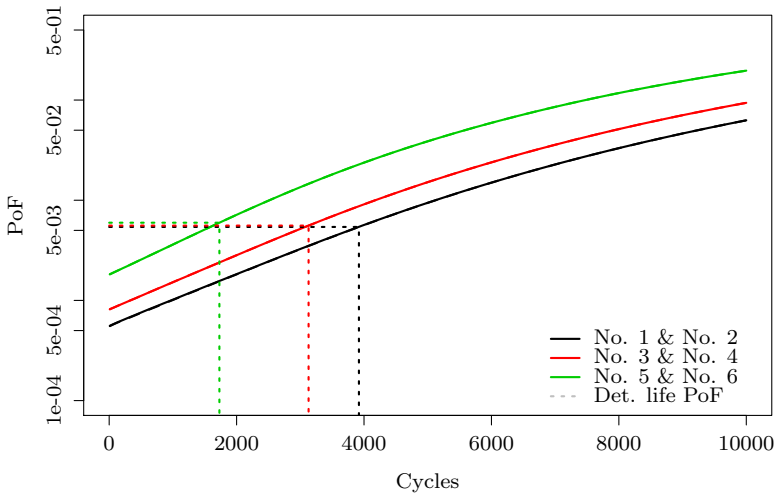

Figure 6.6.: Single indication PoF for the six simple components. The dashed lines indicate the corresponding deterministic life N_{det}

transitioning. In a deterministic analysis of a such large component the transition of an embedded into a surface crack is typically not accounted for.

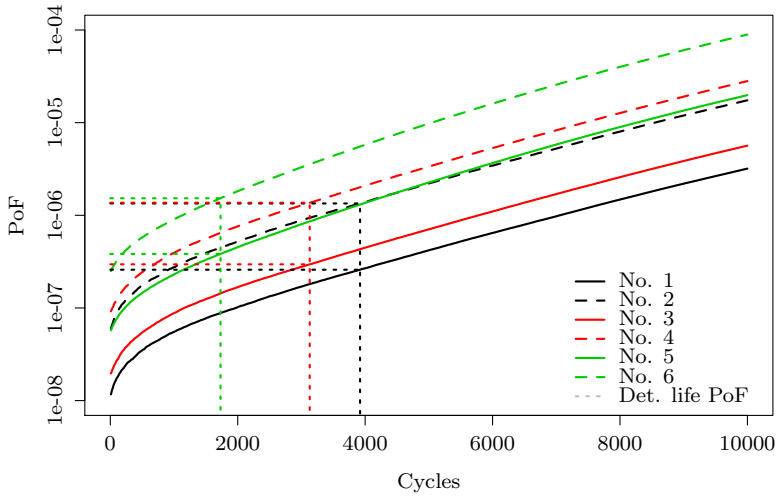

Figure 6.7.: Design PoF for the six simple components. The dashed lines indicate the corresponding deterministic life N_{det}

6.2.2. Probabilistic result correlation for different component geometries

The weak correlation of the design PoF with the deterministic life already suggests a complex relation between the probabilistic results for different components. As a first guess it might be expected, that the design PoF can be simply scaled by the volume ratio, if the stress fields are comparable, as the flaw occurrence rate is controlled by the total volume as described in chapter 2.8.3. This assumption is only correct for large cycle numbers, when all possible flaws in the simulation will fail, as shown in Fig. 6.9. For smaller, in reality more relevant, cycle numbers the PoF ratio is influenced by other effects. Table 6.3 shows the pairwise ratios of the volumes, surface areas and design PoFs @N_{det} of the six simple components. As shown there, the ratio of the design PoFs is not the same as the volume ratios. This is to be expected, as the size of the already mentioned surface effect is different for the six components. In addition in table 6.3 the surface ratios are also shown. As for the volume ratio there is no simple correlation between the design PoFs and the surface areas.

This can be understood, as both effects, the volume and the surface effect, influence the PoF ratio. In the investigated cases, the volume ratio stays the same, but the surface ratio and the stress field changes. Figure 6.8 shows the local failure rate

Components	Volume ratio	Surface area ratio	design PoF ratio @N_{det}
2 / 1	6	1.75	5.47
4 / 3	6	1.88	4.98
6 / 5	6	2.15	4.51

Table 6.3.: Comparison of the volume, surface and design PoF ratio @N_{det} for three pairs of the six components.

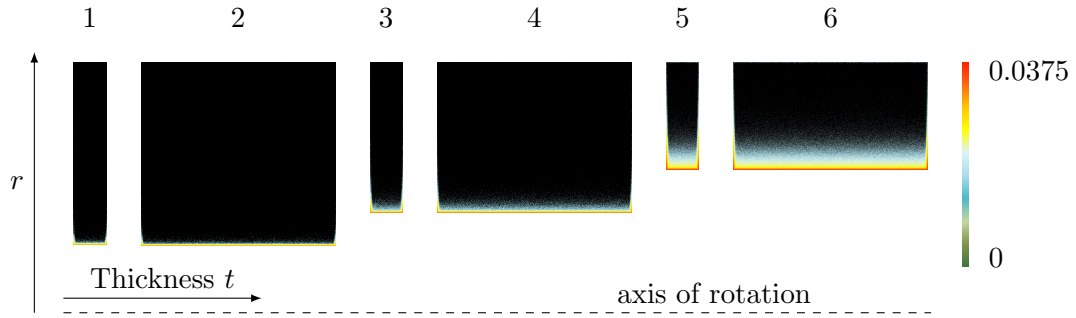

Figure 6.8.: Local failure rate maps on a logarithmic scale of the six example components after 10000 cycles

maps of the respective components. The local failure rate is the local probability of failure under the assumption that a flaw is located there. From this plots it can be understood, that in the case of components 1 and 2 the PoF can nearly be scaled by the volume ratio, as only a small part of the failures is generated at the left and right surface of the component, which is not reflected by the volume scaling for these components. With increasing component number the surface effect becomes more and more dominant, as the surface to volume ratio of the components becomes larger.

In Fig. 6.10 the design PoF, surface and volume ratios versus the number of cycles of the six components are shown. Based on the discussion so far, it is expected that the design PoF ratios are in between the surface and volume ratio of the respective components. This is the case for all component pairs. Furthermore, all PoF ratio curves show a very similar structure. At low cycle numbers the PoF ratio first decreases, before it starts to rise and converges to the volume ratio for a very large number of cycles, as shown in Fig. 6.9.

The failures in the first cycle are the flaws which fail instantaneously due to a large

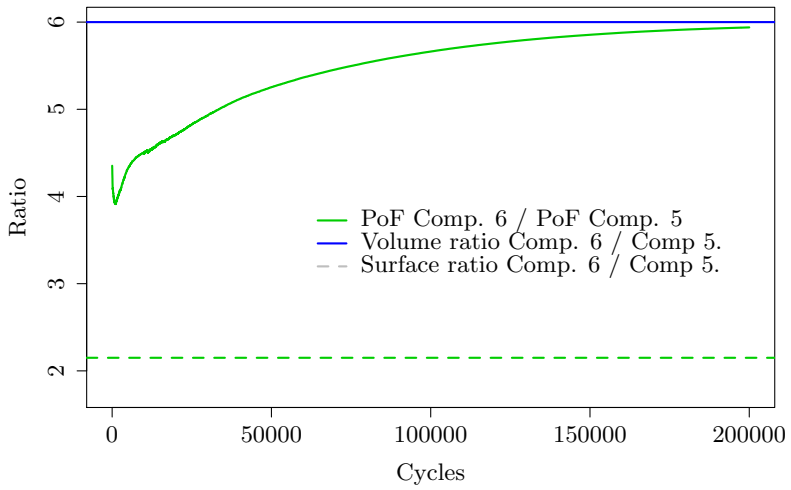

Figure 6.9.: Development of the design PoF ratio of components 5 and 6 for a large number of cycles. Similar relations hold true for components (1 and 2) and (3 and 4)

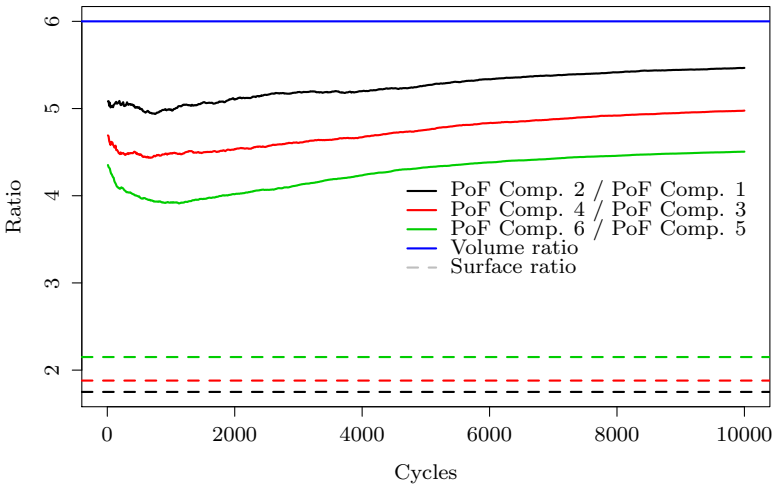

Figure 6.10.: Development of the pairwise design PoF ratio of the six simple components

crack size. In the following other large cracks which reach the critical flaw size after a short growth period will fail. As cracks close to the surface experience an increased stress intensity, as described in 2.3, the crack growth rate and failure probability is increased. Due to this within the first cycles the PoF ratio drops, as the relative amount of failing cracks close to surfaces increases. With further increasing number of cycles the surface close cracks begin to die out and the surface far cracks start to fail. Due to this the PoF ratio increases and converges to the volume ratio of the components. With increasing surface to volume ratio the surface effect becomes more dominant. This can be seen in Fig. 6.10 as the PoF ratio of components five and six is the smallest followed by the ratio of components three and four. The minimum of the curves is a consequence of the competition between surface related and volume related failures as described before.

6.2.3. Scaling of probabilistic results for 50Hz and 60Hz components

The scaling approach shown in the last section is a simple case to show principle effects which have to be accounted for, if probabilistic results are transfered between similar components. A scaling approach with higher practical relevance is presented in this and the following sections.

As stationary gas turbines are often used for electric power generation, the dominant operation frequencies are 50Hz and 60Hz corresponding to the respective electric grid frequencies (50Hz and 60Hz markets). To reduce the expenses during the design phase of a gas turbine oftentimes only one design is developed for a specific frequency and afterwards the components are geometrically scaled for the other frequency. The scaling is done by multiplying the geometric dimensions of the components by the ratio of the respective operational frequencies. As can be seen by (6.1), if the frequency increases by a factor c, all radial dimensions have to be multiplied by $\frac{1}{c}$, to keep the centrifugal stresses in the component the same. From a deterministic fracture mechanics analysis it is expected that the lifetime of the component is the same, if the stresses are the same in the critical regions as shown in Fig. 6.11.

The design PoF for both components is shown in Fig. 6.12. As all geometric dimensions have been scaled by $\frac{5}{6}$ the volume of the component is reduced by a factor of $\left(\frac{5}{6}\right)^3 \approx 0.58$. As already discussed in the last section the ratio of the design PoFs only converges for large cycle numbers to the volume ratio. For this case in Fig. 6.13 the PoF ratio is shown. As shown there the design PoF ratio lies between the volume and surface ratio, as already for the simple components from the last section. As the volume and surface ratio is closer to each other as compared to the six simple components from the last section, the possible error in the calculated design PoFs

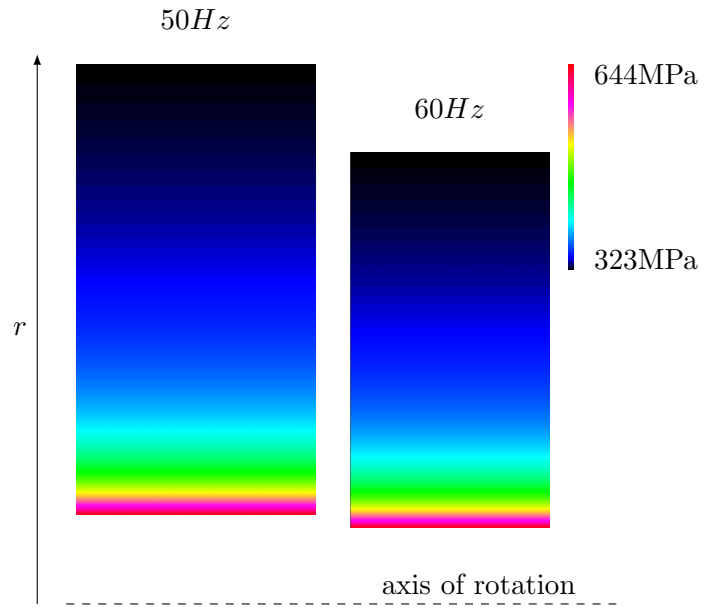

Figure 6.11.: Tangential stresses for disks rotating with 50Hz or 60Hz, with the same maximum stress. The components dimensions are scaled by 5/6

becomes more important. As shown in Fig. 6.13 the error in the design PoF ratio becomes significant especially at small cycle numbers.

In general, as shown in Fig. 6.13 also for this frequency based scaling approach the ratio of the design PoF shows similar trends as for the simpler scaling approach in section 6.2.2.

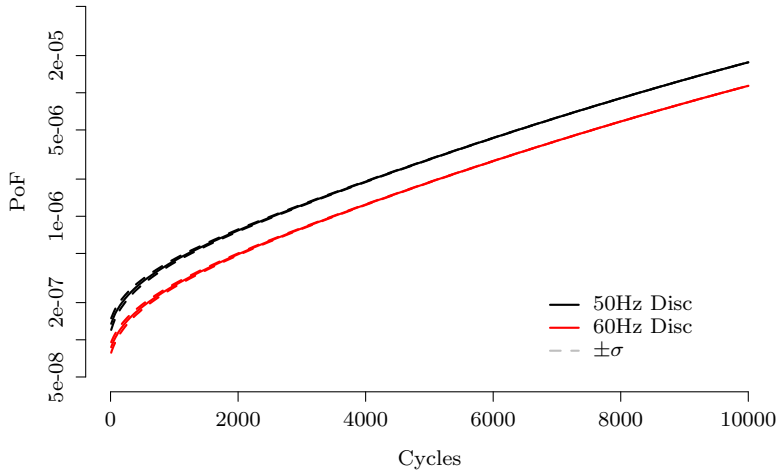

Figure 6.12.: *PoF* for a disk rotating with 50Hz or 60Hz, with the same maximum stress.

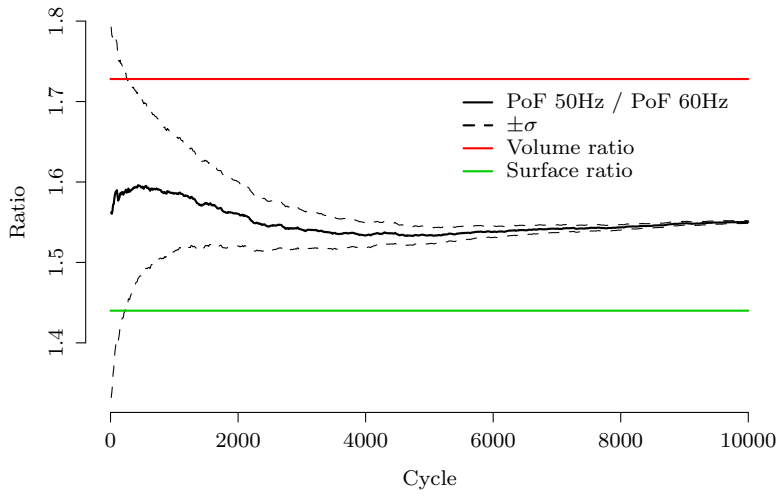

Figure 6.13.: *PoF* ratio for two disks rotating with 50Hz or 60Hz, with the same maximum stress.

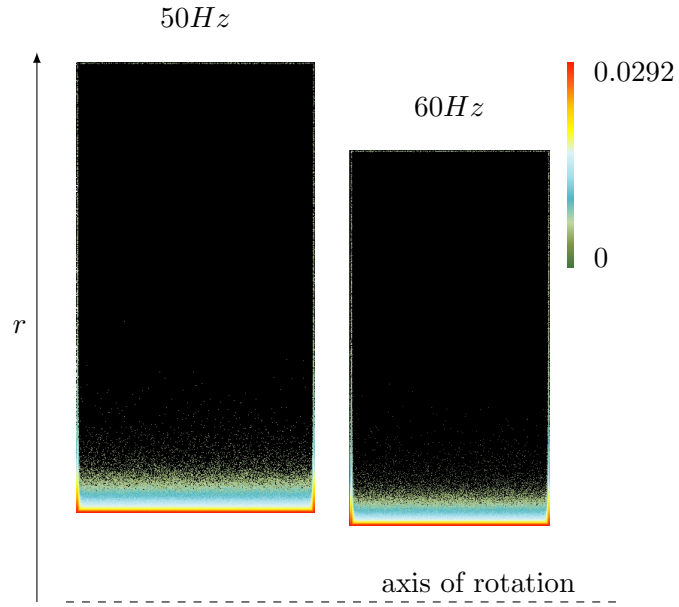

Figure 6.14.: Local failure map on a logarithmic scale of two disks rotating with 50Hz (left) and 60Hz (right).

6.2.4. Scaling of probabilistic results for 50Hz and 60Hz with thermal transient considerations

In the last section the relationship between scaled 50Hz and 60Hz disks for non transient mechanically stress driven components has been presented. In this chapter transient effects as they occur if an engine is started with cold components after a significant amount of downtime will be discussed. In order to analyze the transient behavior of the components discussed in the previous section, transient FEA of these components have been performed.

The transient boundary conditions applied represent a typical start stop cycle of a large stationary gas turbine. In Fig. 6.15 and Fig. 6.16 the assumed gas temperature and rotational frequency are shown. Fig. 6.17 shows the transient development of the first principle stress at the inner radius and at the center location $\approx 2/10$ from the hub for the 50Hz and 60Hz. In Fig. 6.17 it is shown, that the center bulk region experiences a significant stress overshoot, which is driven by thermal stresses, as the temperature at the surface of the component increases faster than in the inner of the component. Due to this the material which is closer to the surface expands faster

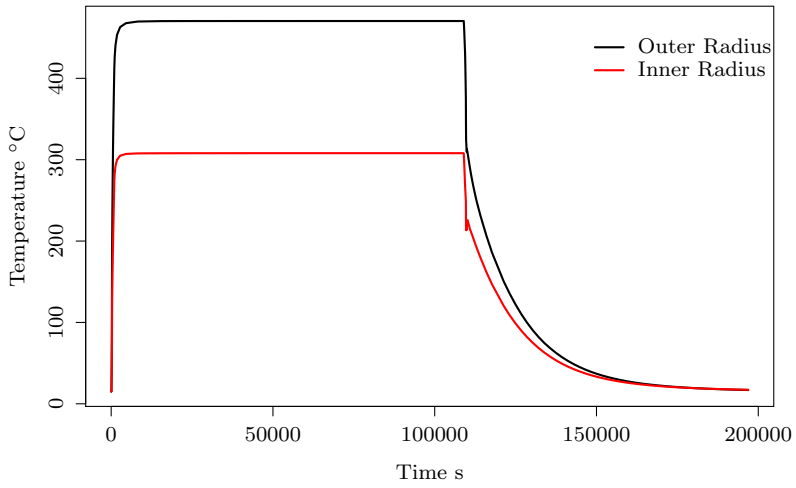

Figure 6.15.: Transient gas temperature boundary conditions as used in the finite element calculation.

and by this additional tensile stresses are introduced. This effect is more pronounced for the larger 50Hz components as shown in Fig. 6.18. At the shut down there is a small overshoot in the hub region, which is also thermal driven. This tensile overshoot relates to a change in the cooling air distribution in the engine, which occurs during the shutdown of the engine. In the FEA this effect is modeled by a change of the heat transfer coefficient, resulting that the inner diameter cools somewhat faster than the outer diameter.

As shown in Fig. 6.17 and Fig. 6.18 different locations in the component have quite different transient stress development. In Fig. 6.19 the maximum first principal stress for the 50Hz and the 60Hz component are displayed. By comparing the plots in Fig. 6.19 with the plots in Fig. 6.11 a change in the structure of the stress field becomes obvious. The most prominent difference between the stress distributions is the increased stress area in the bulk region of the components, which is driven by the aforementioned thermal overshoot during the start up phase.

The plots shown in Fig. 6.20 are the maximum transient stress, the maximum ratio of the first principle stress and the fracture toughness and the local failure rate. All these plots show a similar distribution structure in the inner part of the

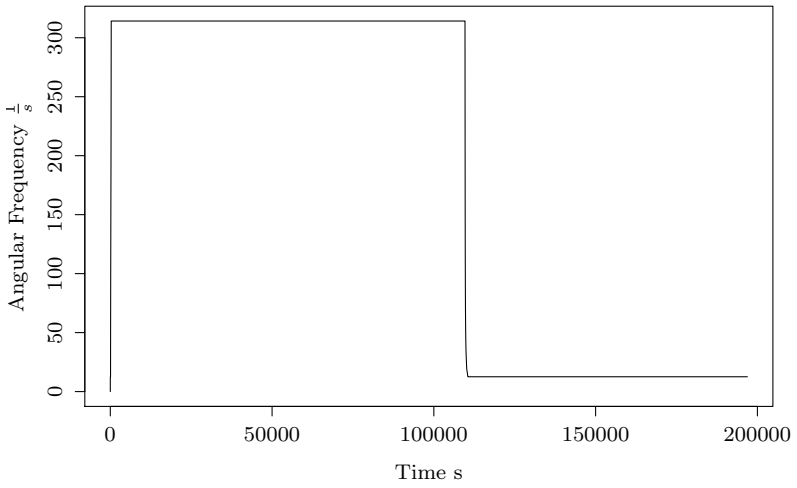

Figure 6.16.: Transient rotational frequency

component, which is essentially controlled by the thermal transient behavior of the components. In general the 50Hz component exhibits a relatively larger area which is controlled by the thermal transient compared to the 60Hz component. This is expected, as only the mechanical stresses are scalable by a frequency scaling approach. Especially the ratio plot of stress and fracture toughness and the local failure plot show a significant difference between the 50Hz and 60hz component. Due to the larger mass and dimension of the 50Hz component it takes in general longer to bring the component into a thermal steady state condition. This also results in a larger stress overshoot in the bulk region for 50Hz components. As the thermal boundary conditions are assumed to be the same for both components, the thermal stresses in the 50Hz component are higher and the mean relevant fracture toughness is lower. This transient effect can change the scaling between 50Hz and 60Hz components as discussed based on the results presented in the last sections.

Fig. 6.21 shows the design PoF ratio as well as the surface and volume ratio of the 50Hz and 60hz components. The design PoF ratio can be significant larger than the volume ratio of the components, which is the upper limit for the steady state comparison discussed in the last section. In addition in Fig. 6.21 the standard deviation of the design PoF ratio based on the design PoF standard deviation is

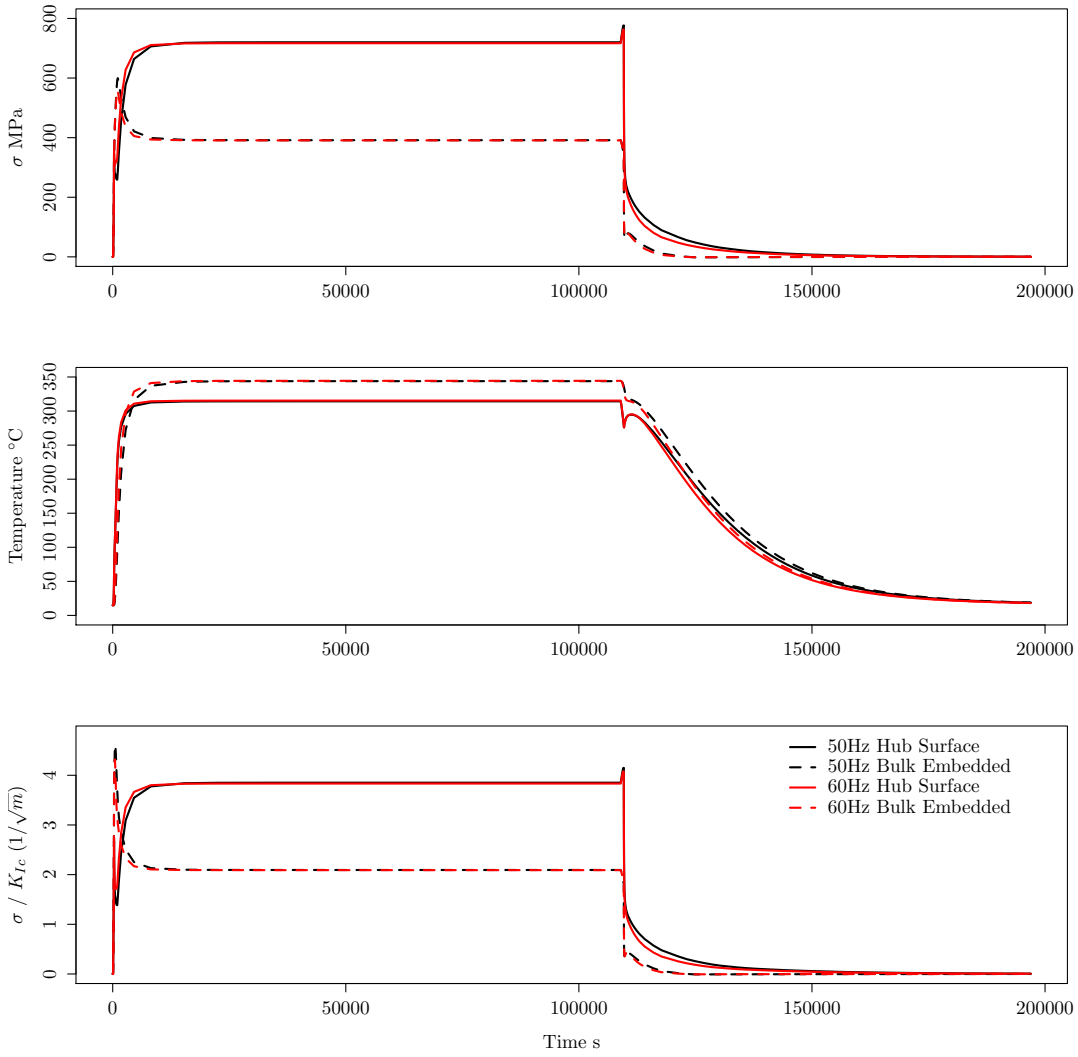

Figure 6.17.: Transient stress, temperature and stress toughness ratio development in the component for a complete start stop cycle.

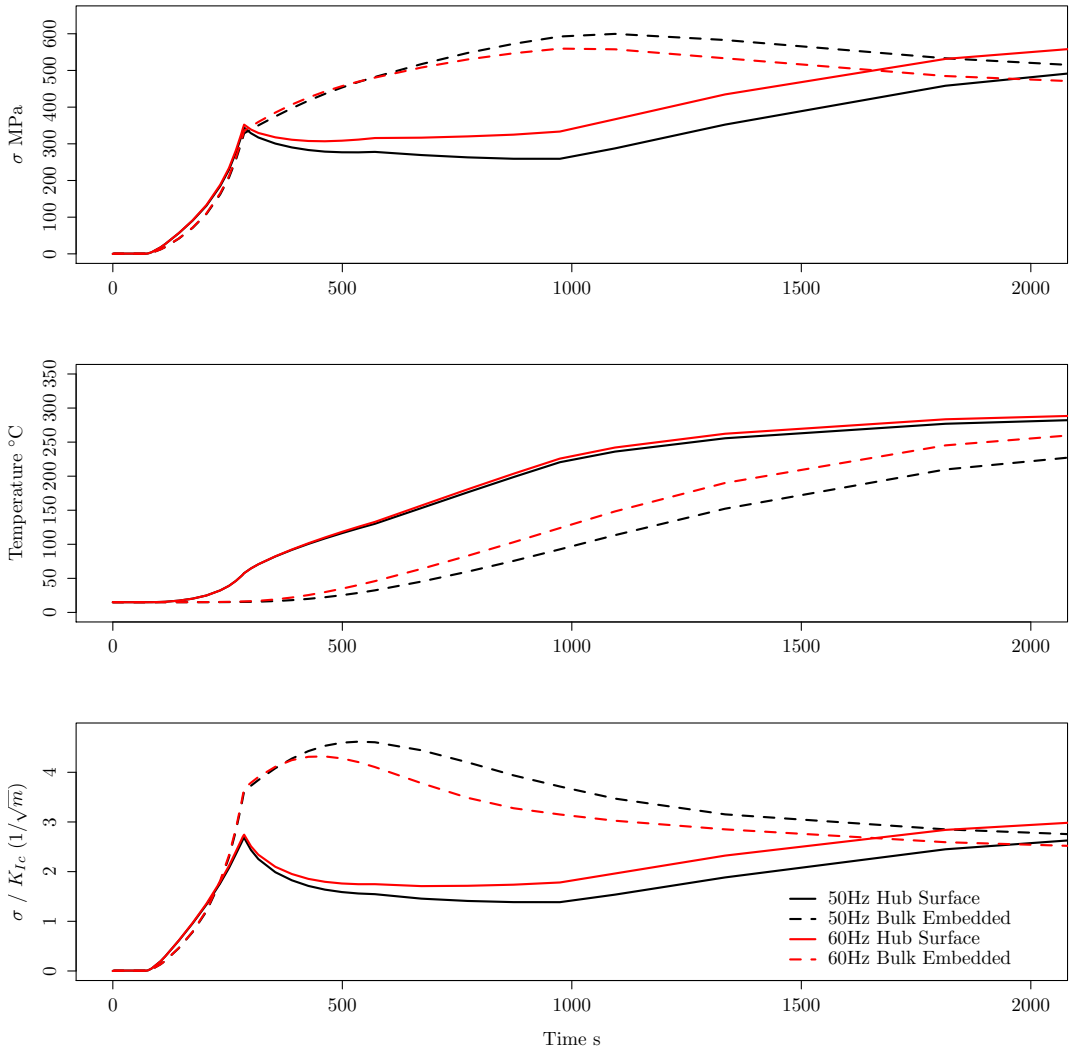

Figure 6.18.: Transient stress, temperature and stress toughness ratio development in the component for the start up phase.

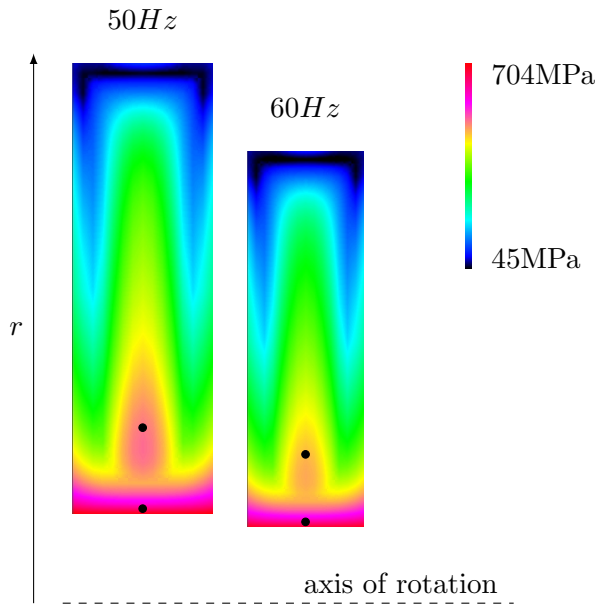

Figure 6.19.: Maximum transient first principal stresses for disks rotating with 50Hz or 60Hz, with thermal transient boundary conditions. The black dots indicate the locations of the transient stress development shown in Fig. 6.17 and Fig. 6.18

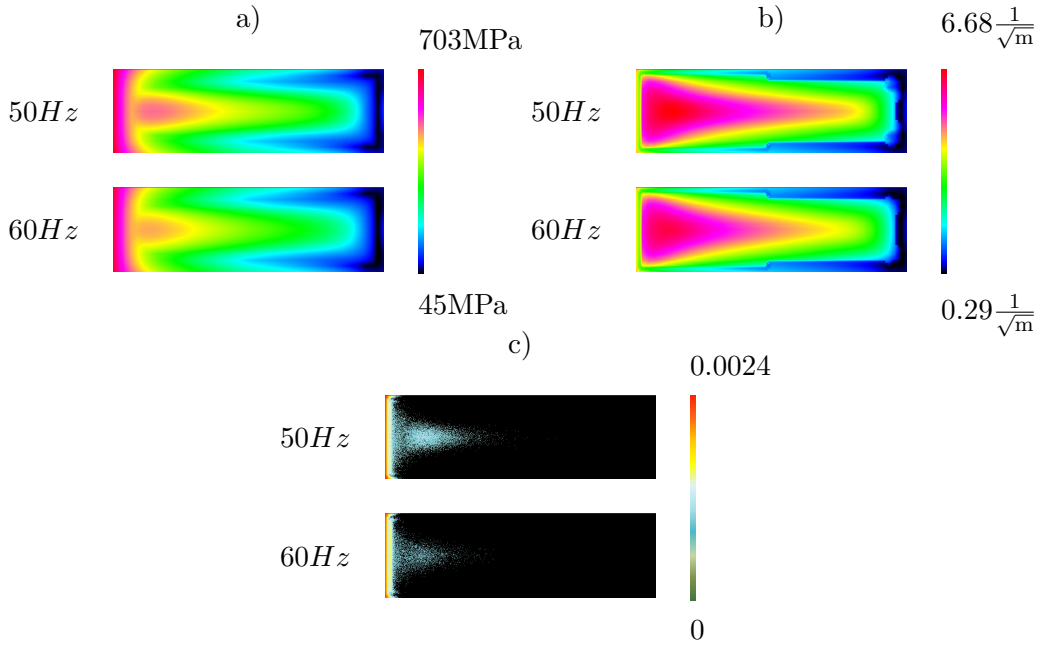

Figure 6.20.: Stress at critical time point (a), ratio of stress and fracture toughness at critical time point (b) and local failure rate map on a logarithmic scale (c). The component geometries of the 60Hz component are scaled by 6/5 for a better comparison. Due to the scaling the relative size of the different features, especially the relative size of the inner failure region, can be compared.

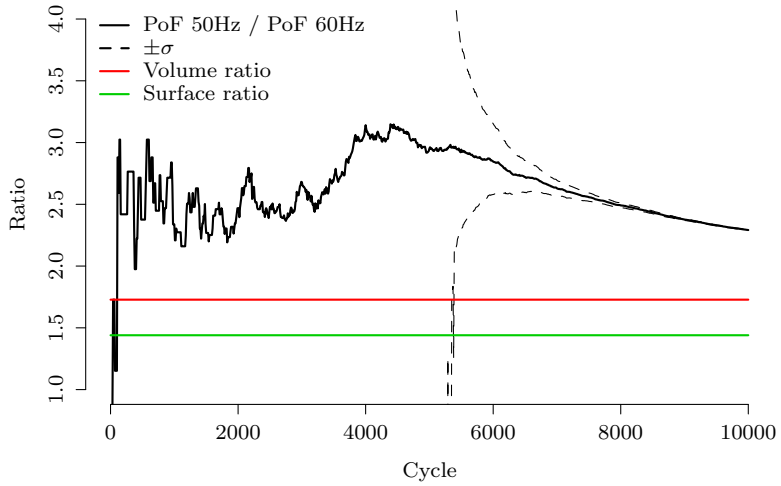

Figure 6.21.: *PoF* ratio for disks rotating with 50Hz or 60Hz, with thermal transient boundary conditions.

shown. The design *PoF* standard deviation can be estimated as described in section 5.1. Fig. 6.22 shows that the design *PoF* of the simulated components becomes quite small and the standard deviation of the design *PoF* becomes larger than the mean *PoF* below approximately 5000 cycles, calculated with 10^{11} samples. Therefore below $\approx$ 5000 cycles the *PoF* ratio can fluctuate significantly.

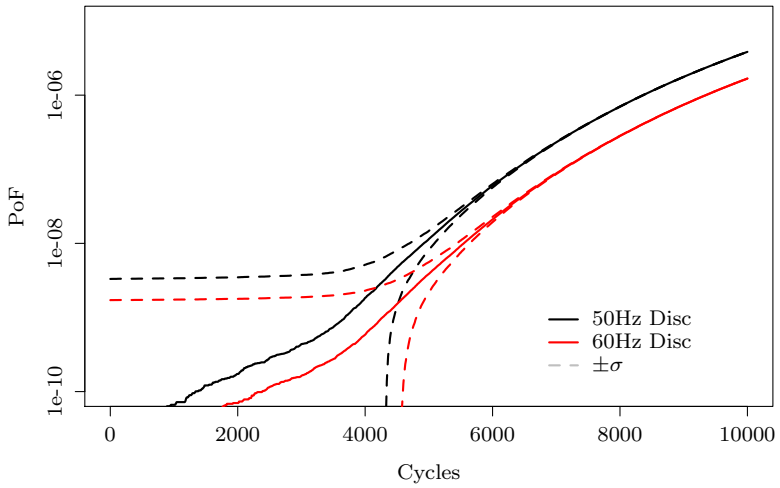

Figure 6.22.: PoF for a disk rotating with 50Hz or 60Hz, with thermal transient boundary conditions.

To overcome the resolution problem with 10^{11} samples at low cycle numbers the same components have been simulated assuming a 130% rotational overspeed condition for the failure criteria. Here it is assumed that all stresses are mechanical and the 130% overspeed condition can occur at each load step of the transient, thus the fracture toughness is effectively reduced by $1.3^2 = 1.69$. This increases the PoF as shown in Fig. 6.23. Such an over speed condition can occur, if for instance in a power plant the generator is disconnected from the grid due to a shortcut. In such a case it is in general not possible to reduce the fuel flow fast enough to prevent an acceleration of the engine. The maximum amount of potential overspeed depends on details of the engine and can vary between $105\% - 130\%$. The comparison of the local failure rate plots in Fig. 6.24 and Fig. 6.20 show that the local failure rate is increased due to the over speed assumption. Also Fig. 6.23 show that the design PoF is increased as expected and that the estimated relative standard deviation is reduced. In order to increase accuracy even further, the components have been calculated for different cycle numbers with different number of samples as shown in table Tab. 6.4.

Fig. 6.24 shows the local failure rate plot of 50Hz and 60Hz component with transient boundary conditions and over speed assumption. Comparing these plots with

Frequency Hz	Cycles	Number of Samples	Standard deviation
50	100	10^{13}	$2.74\,10^{-11}$
50	3000	10^{12}	$3.42\,10^{-10}$
50	10000	10^{11}	$1.00\,10^{-8}$
60	100	10^{13}	$1.20\,10^{-11}$
60	3000	10^{12}	$1.65\,10^{-10}$
60	10000	10^{11}	$5.25\,10^{-9}$

Table 6.4.: Number of cycles, number of samples and estimated standard deviation for the 50Hz and 60Hz components with transient boundary conditions and 130% overspeed condition.

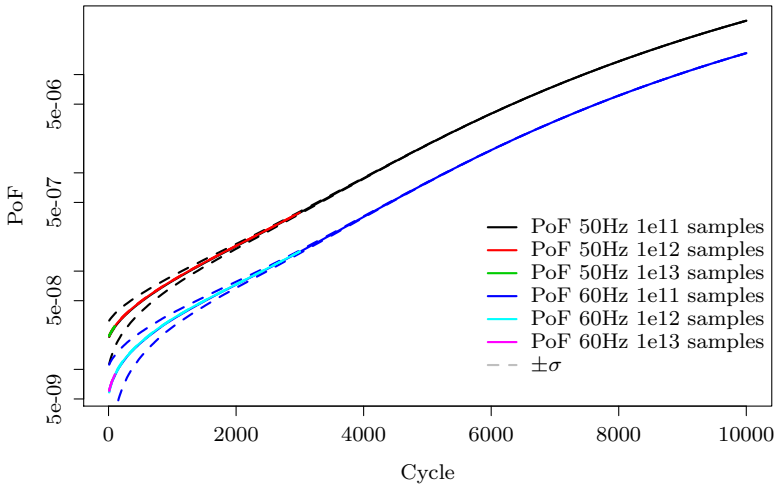

Figure 6.23.: *PoF* for disks rotating with 50Hz or 60Hz, with thermal transient boundary conditions and 130% overspeed.

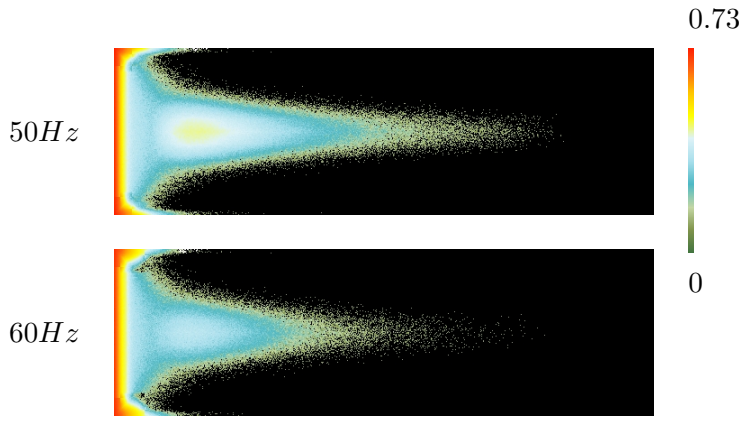

Figure 6.24.: Local failure rate plots for a disk rotating with 50Hz or 60Hz, with thermal transient boundary conditions and 130% overspeed as failure criteria.

the local failure plots in Fig. 6.20 reveals similar structures, whereat the maximum and overall local failure rate in Fig. 6.24 is higher.

As shown in table 6.4 and Fig. 6.23 the standard deviation of the design PoF decreases with increasing number of samples. As the calculation time is nearly linear with the number of samples it was not possible to calculate the PoF up to 10000 cycles with 10^{13} samples within a reasonable time on the available amount of CPUs.

Fig. 6.25 shows the ratio of design PoF, calculated with different amounts of samples, and the surface and volume ratio. As already indicated in Fig. 6.21 the ratio of the design PoFs is controlled by the transient thermal effect even at small cycle numbers. However, as shown in Fig. 6.23 the mean value of the design PoF ratios is independent of the number of simulations and in very good agreement to each other. Based on the standard deviation for the simulation with 10^{11} simulations this is not expected. The reason for this unexpected good agreement is that the simulations with 10^{11} samples have been made with the same random seed, thus the simulated cracks in the components are correlated. In general one should be careful with such correlations within MC-simulations, but in this case the correlation dramatically increased the accuracy of the calculation of the ratio. To assure that this correlation does not introduce unfavorable effects, the simulations with 10^{12} and 10^{13} have been done each with different random seeds and therefore with different flaw and material configurations.

Fig. 6.25 shows that in this case the transient thermal effect dominates the PoF

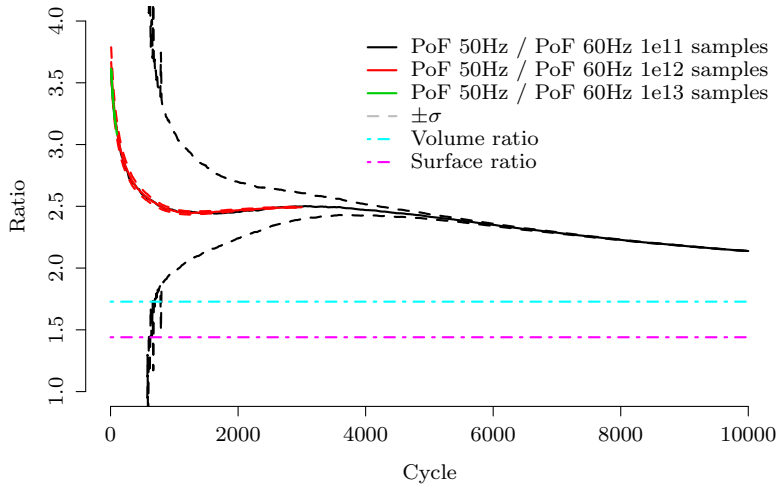

Figure 6.25.: *PoF* ratio for disks rotating with 50Hz or 60Hz, with thermal transient boundary conditions and 130% overspeed.

ratio. With increasing cycle number the ratio converges to the volume ratio. In the range of 1000 to 2500 cycles a small dip occurs in the ratio, which is related to the surface effect. It seems that in this cycle range the surface effect becomes stronger, thus the overall *PoF* ratio is somewhat more driven into direction of the surface ratio.

The results shown so far demonstrate, that it is not easy to transfer *PoF* results from 50Hz and 60Hz components. In detail the design *PoF* ratio depends on the specific components and boundary conditions.

Fig. 6.26 shows the design *PoF* ratio of a 50Hz and 60Hz component, which have the same thermal boundary conditions and material properties as discussed before. The only difference is the thickness of the disks, which is just 25% of the examples shown before. This reduced thickness reduces the discussed transient thermal effect, as the disks reach the thermal equilibrium faster, due to the smaller total mass of the disks. Due to this the thermal stress overshot is reduced and the fracture toughness at the failure critical point in time is increased. As a consequence the transient thermal influence to the *PoF* ratio is reduced. In this case the *PoF* ratio is dominated up to 2500 cycles by the surface effect, then a small overshoot occurs due to the remaining transient thermal effect and finally it converges to the volume ratio.

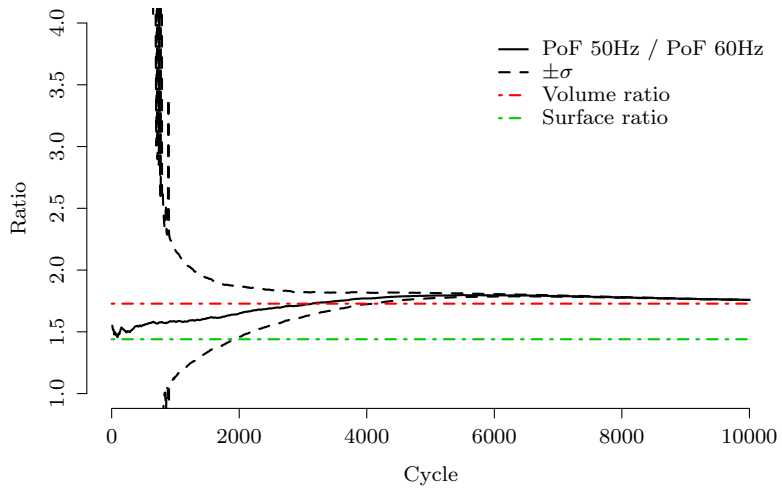

Figure 6.26.: PoF ratio for thin disks rotating with 50Hz or 60Hz, with thermal transient boundary conditions and 130% overspeed.

6.3. Real Component Scaling Behavior

In the last sections three different effects influencing the transferability of probabilistic results with respect to similar components have been discussed. For the sake of simplicity and to get an overview in the last sections simple components, geared to show the dominant effects have been discussed. In this section the transferability of six real gas turbine components, each of them as 50Hz and 60Hz version, will be analyzed. As the discussed models represent real gas turbine components of Siemens a detailed discussion of the calculation boundary conditions cannot be made, but nevertheless additional effects influencing the PoF scaling can be shown and discussed.

The shapes of the discussed components are shown in Fig. 6.27. The components D1, D3 and D5 have a significant larger inner diameter than the components D2, D4 and D6, while the outer diameter of all components is nearly the same. Due to the smaller inner diameter the change of the sound path length within the components D2, D4 and D6 becomes such severe, by scaling from 60Hz to 50Hz, that the noise threshold KSR_{th} of the ultrasonic examination increases. This influences the PoD and the KSR_{dec} value and in total the quality of the ultrasonic inspection is reduced. The influence of the KSR_{th} value to the PoD has been discussed in subsection 2.8.2.

Beside the PoD the KSR_{dec} value is influenced by the KSR_{th} value, but there is no simple model available to describe the relation between KSR_{th} and KSR_{dec}. KSR_{dec} is essentially a value which defines the indication size at which the customer, in this case Siemens, can reject a component from the vendor. According to this KSR_{dec} is strong influenced by commercial considerations like the price of a component, as with a decrease of the KSR_{dec} the price of the component increases.

In the investigated cases of the components D2, D4 and D6 the assumed PoD and the KSR_{dec} value for the 50Hz components is worse compared to the 60Hz components due to a strong change in the ultrasonic sound path length. Due to this the noise threshold increases and the detectability of flaws becomes worse. Following the amount of flaws removed by the quality inspection process is reduced in the larger 50Hz components D2, D4 and D6 compared to the 60Hz equivalents. As the amount of flaws which are initially in the component is assumed to be proportional to the volume of the component, the remaining flaw density in the 50Hz version of the components D2, D4 and D6 is larger than in the 60Hz version. Due this the PoF ratio is larger than the volume ratio even for large cycle numbers, at which the PoF converges to the mean flaw per component value.

In Fig. 6.28 the PoF ratios of six frequency scaled (50/60Hz) gas turbine components are shown. For small cycle numbers the ratios are similar as the ratios which have been discussed in the last sections. The PoF ratio of the components D1, D3 and D5 converge for large cycle numbers, as expected and discussed in subsection 6.2.2, to the volume ratio. The components D2, D4 and D6 do not converge for large cycle numbers to the expected volume ratio. This is related to the difference in the ultrasonic inspection which creates larger flaw densities within the larger 50Hz components due to a worse PoD and a larger KSR_{dec} compared to the smaller 60Hz components. In general the PoF ratio should be larger than the volume ratio for all 50Hz components, as for all 50Hz components the sound path length is increased compared to the 60Hz components.

As the measurement of the PoD is an extreme involved task and the KSR_{dec} is also influenced by economic aspects, during the design process the components are grouped into UT classes depending on the geometric size and material. Within such a group the PoD is described conservatively by a worst case scenario. The 50Hz and 60Hz components D1, D3 and D5 are within the same UT class thus no deviation from the volume ratio is expected. For the components D2, D4 and D6 the 50Hz components are in different UT class than the 60Hz components and following the PoF ratio does not converge to the volume ratio.

However, based on the discussed results in the last chapters practical conservative rules for the transferability of 50Hz and 60Hz components can be deduced. This can

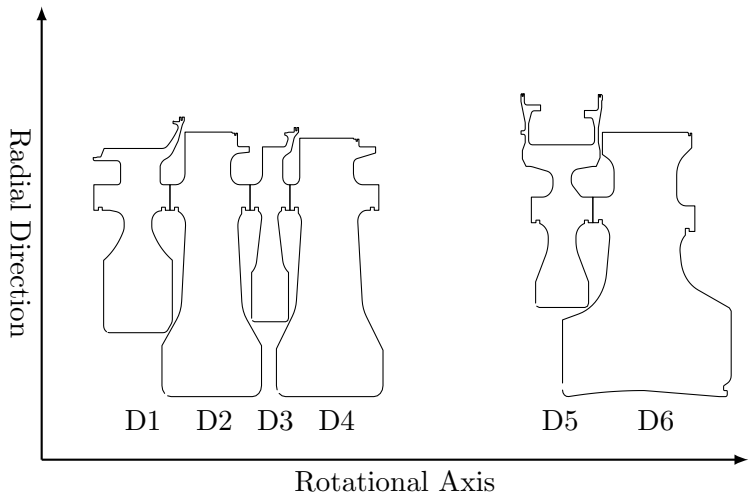

Figure 6.27.: Geometry of the six 50/60Hz rotor components for which the PoF ratios have been calculated. (Figures not to scale.)

reduce the component design process significantly as only a 50Hz component needs to be analyzed in general.

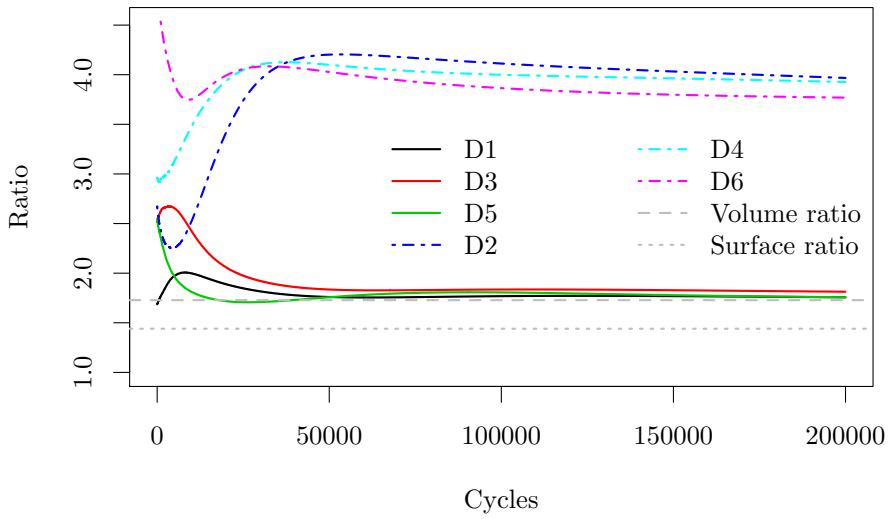

Figure 6.28.: Six *PoF* ratios calculated from six 50/60Hz rotor components of a stationary gas turbine.

6.4. Influence of Crack Shape in Deterministic and Probabilistic Assessment

In general, the shape of the flaw as described by the $\frac{a}{c}$ ratio is not known from the ultrasonic assessment. Therefore, in a fatigue crack growth assessment, an $\frac{a}{c}$ ratio has to be assumed. In a deterministic fracture mechanics assessment of an embedded elliptic flaw, the ratio is often set to $\frac{a}{c} \approx 0.4$, as this is assumed to yield the largest stress intensity factor at the beginning of the calculation [8].

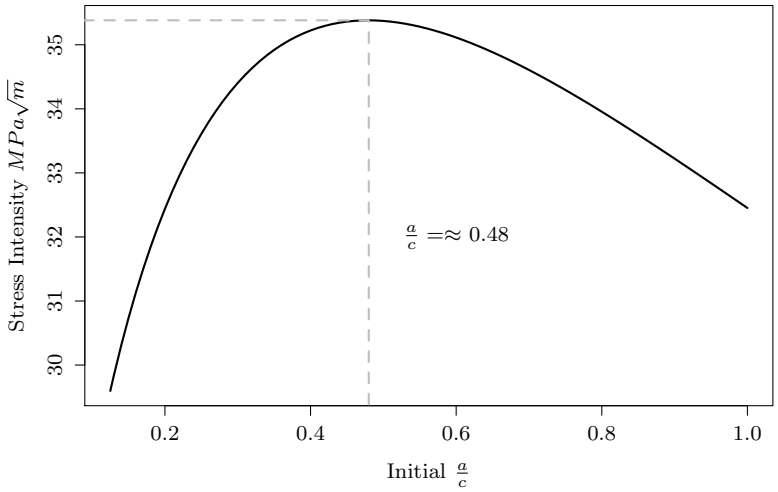

Figure 6.29.: Dependence of the initial stress intensity on the initial $\frac{a}{c}$ for an example embedded elliptic crack.

This assumption is not quite correct as the ratio depends slightly on the used geometry factor function (Fig. 6.29). Here, the stress intensity of an example crack (Tab. 6.5) based on the geometry factor function used in IWM VERB (as described in chapter 2.3.2) is displayed. As shown here the maximum stress intensity occurs in this case at $\frac{a}{c} \approx 0.48$. Further, this assumption is only conservative as long as the $\frac{a}{c}$ ratio is kept constant during the fatigue crack growth calculation. If the $\frac{a}{c}$ ratio changes during the calculation this assumption is in general not conservative with respect to the calculated life as shown in Fig. 6.30 and Fig. 6.32. In todays commercially available fracture assessment software tools like IWM VERB or NASGRO, the $\frac{a}{c}$ ratio is in general not kept constant. Under the assumption that the $\frac{a}{c}$ ratio can change during the progression of the crack, the stress and temperature fields are constant

and the material properties are isotropic, the crack tends to become circular ($\frac{a}{c} = 1$) as the crack grows as shown in Fig. 6.31 and Fig. 6.32.

As an example, the crack growth of an embedded crack with constant crack size and variable $\frac{a}{c}$ ratio, embedded into stress and temperature fields without gradients as given in Tab. 6.5 has been calculated using IWM VERB for different $\frac{a}{c}$ ratios. During the calculation the crack shape is not kept constant.

Initial Crack Area	28mm^2
σ_{max}	$526\text{MPa}\sqrt{\text{m}}$
σ_{min}	$0\text{MPa}\sqrt{\text{m}}$
R	0
C	$1.5\,10^{-7}$
m	2.2
K_{Ic}	$46\text{MPa}\sqrt{\text{m}}$

Table 6.5.: Parameters for the example crack growth calculation.

The crack size and the maximum stress intensity of a crack as function of the cycle number has been calculated for the different initial $\frac{a}{c}$ ratios. As can be seen in Fig. 6.32, the $\frac{a}{c}$ ratio tends to become 1 with increasing numbers of cycles (horizontal direction). The maximum stress intensity, K_I, for low cycle numbers is given by an $\frac{a}{c}$ ratio in the order of 0.48. But with an increasing number of cycles, the lower initial $\frac{a}{c}$ ratios yield higher stress intensities while the crack grows. Assuming a fracture toughness of $46\text{MPa}\sqrt{\text{m}}$, the shortest life time ($\approx$ 4302 Cycles) is obtained by an $\frac{a}{c}$ ratio of approximately 0.175. The life cycle difference between an assumed $\frac{a}{c}$ ratio of 0.4 and 0.175 in this example is in the order of 800 cycles or roughly $\approx 18.8\%$. As shown by this simple example, an $\frac{a}{c}$ ratio of 0.4 does not always yield conservative life cycle estimates and it also demonstrates that the impact of the $\frac{a}{c}$ ratio in a deterministic assessment can be significant. In general it is not possible to give a conservative estimate for the $\frac{a}{c}$ ratio for all possible circumstances and due to inhomogeneous stress fields this becomes even more complex.

In the probabilistic assessment, the initial $\frac{a}{c}$ ratio can be a random variable. As the available information about the initial $\frac{a}{c}$ ratio distribution in real components is very limited, a uniform distribution can be assumed.

As an example, the PoF of a low risk component has been calculated assuming uniform $\frac{a}{c}$ ratio distributions with different ranges. Just as in the deterministic assessment, also in the probabilistic assessment the crack shape can have a significant impact as shown in Fig. 6.33. The large impact in the case of $0.1 \leq \frac{a}{c} \leq 0.4$ to the

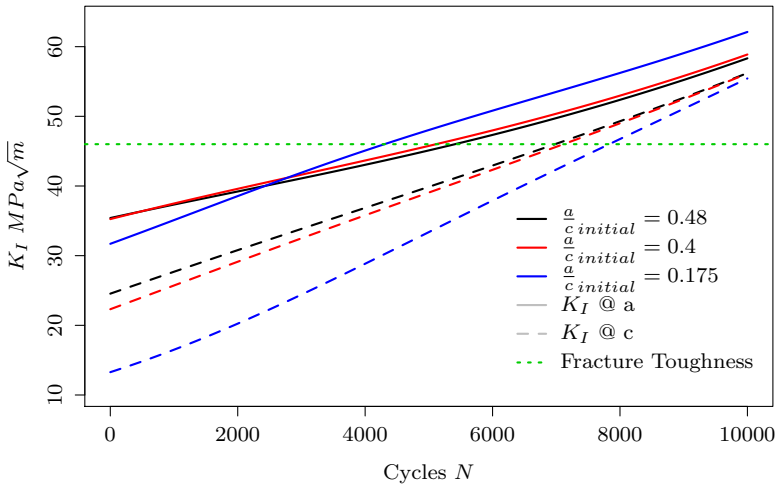

Figure 6.30.: Comparison of the stress intensity development for three different initial $\frac{a}{c}$ ratios.

PoF is related to the fact that the flaws show a more elongated shape and are oriented in a worst case orientation to the surface. In case of gas turbine rotor forgings, such needle-like flaw shapes are not expected.

As long as the $\frac{a}{c}$ distribution is symmetric around 1, the bounds of the distribution have only a small impact on the PoF. If for instance due to the manufacturing process this is not the case and the distribution is dominated by elongated flaws which are oriented parallel to the surface, this is different (Fig. 6.33 $0.1 \leq \frac{a}{c} \leq 0.4$). Such elongated surface parallel flaws can be produced for example by a rolling process during the manufacturing of the component. In the case of gas turbine rotor disks, the observed flaws tend to be more circular than elongated as shown in [29]. Thus, the $\frac{a}{c}$ distribution in case of gas turbine rotor forgings is assumed to be symmetric around 1 still allowing for elongated elliptical flaws.

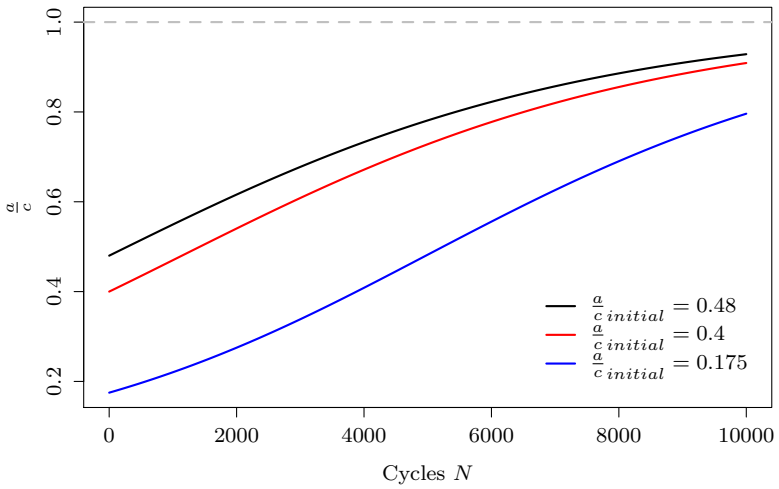

Figure 6.31.: Comparison of the $\frac{a}{c}$ ratio development for three different initial $\frac{a}{c}$ ratios.

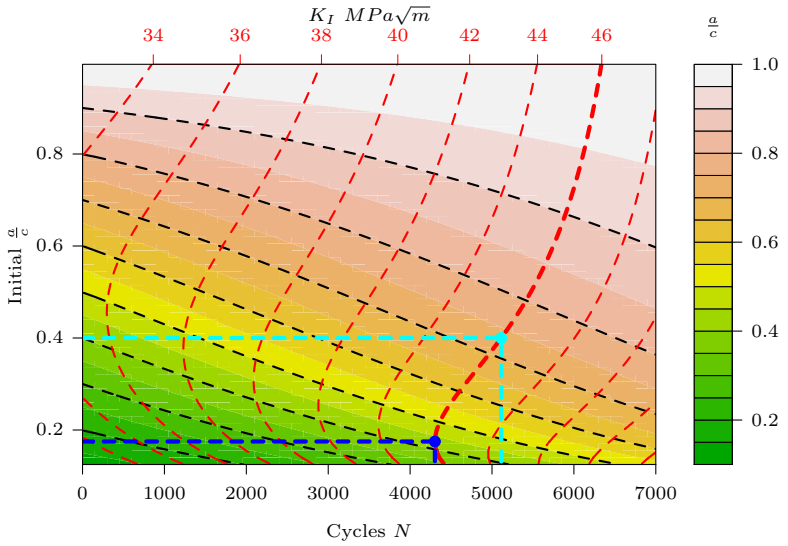

Figure 6.32.: Dependence of the initial $\frac{a}{c}$, cycles N, $\frac{a}{c}$ and stress intensity of an example embedded elliptic crack.

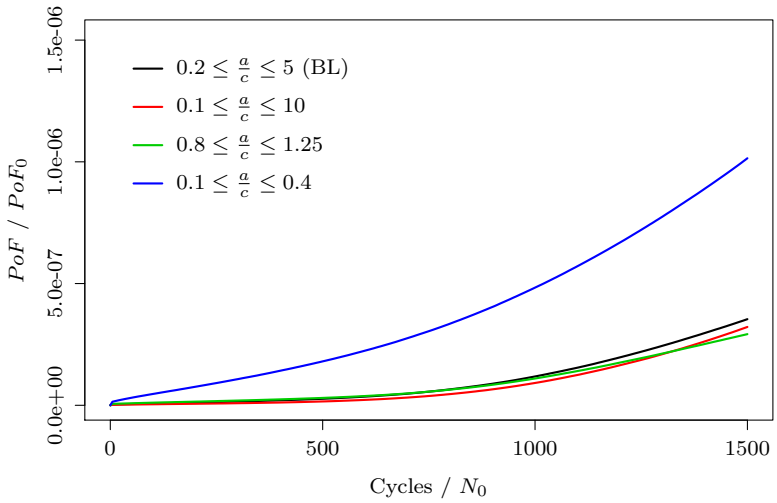

Figure 6.33.: Sensitivity of $\frac{a}{c}$ ratio in *ProbFM* analysis assuming different uniform $\frac{a}{c}$ distributions

7. Conclusions and Outlook

In chapter 6 it has been shown that in general a deterministic fracture mechanics assessment is not performed by applying absolute worst case assumptions. Often the lower or upper bounds of the material and ultrasonic properties are estimated by 2 or 3 standard deviations of the measured scatter. Therefore, the deterministic calculated life is in general not a lower bound of the life and the non-zero risk at the deterministic design point can not be estimated from the deterministic calculated life as shown in chapter 6. Oftentimes, the risk of having a flaw at the highly stressed locations of the component and thus the risk of operation is very low too. However, in a commercial environment these components will be retired from service too early, and resources are ineffectively used. As this is known from experience, often times conservatism in a deterministic approach is reduced by decreasing design factors such as using fewer standard deviations to derive the design curve from the average curve. The problem and risk with this approach is that the risk at the design point is unknown and fleet experience is in general not large enough to quantify the low risks acceptable for large rotating equipment. Hence, in a strongly market driven environment, the probabilistic approach is favored as it quantifies the risk as an integral answer of all important influencing inputs and associated scatter.

One goal of this work was to support the development and implementation of a framework which enables the failure risk management of large rotor forgings in an industrial environment. Another objective was the thorough investigation and analysis of the developed system and framework, as this understanding is necessary for further developments as well as to transfer certain aspects of the approach to different industrial application areas.

Different possible probabilistic modeling approaches have been evaluated and the Direct Simulation Monte Carlo approach has been chosen as the most promising approach to fulfill all requirements. Two other possible options, namely, using commercially available tools, DARWIN or IWM VERB, have been rejected. The reasons for rejecting the aero probabilistic fracture mechanics code DARWIN are discussed in detail in the introduction, but in general the needs in the design of large land based gas turbines are different than the needs in the design of jet engines. The second option was to use a commercially available deterministic fracture mechanics code like IWM VERB or NASGRO to perform the fracture mechanics calculations and create

a wrapper around these tools to perform the probabilistic analysis. This approach has the advantage that the fracture mechanics calculation is performed by an already thoroughly tested tool. As these tools are in general aiming for single crack assessments, they are not optimized for calculation speed and controlling these programs by wrapper code slows them down further. Therefore, within this approach it is not possible to calculate the needed number of crack simulations in a reasonable time.

The developed probabilistic fracture mechanics framework allows for the calculation of the probability of failure and the annual failure risk of forged rotor components. This allows for more design flexibility and risk management of the component such as optimizing service intervals or design optimization with respect to geometry and material.

Furthermore, the presented results show that there is only a weak correlation between the deterministic calculated life numbers and the PoF. This is related to the stress and temperature field distribution and the volume / surface effects in the component as described in chapter 6. The probabilistic approach enables a more comprehensive comparison of different designs, as it evaluates the whole component and not only single locations.

The presented work is only a first step to a full probabilistic fracture mechanics assessment and many improvements and further developments are desired and necessary to remove still existing conservatism of the presented methodology.

For example, the presented single scale temperature scaling approach of the fracture toughness is not favorable from a physical point of view . As the fracture failure mode changes from brittle to ductile, two different scales and scatter processes, which are related to two different physical mechanisms, are expected [12]. The presented modeling assumes only one scale and one scatter process for the entire temperature range. In $ProbFM$ a more sophisticated, physics based two scatter process model has also been implemented, which can not be presented in this work for confidential reasons.

Besides the K_{Ic} modeling, the modeling of the lower bound of the fracture toughness has not been discussed at all, but the lower bound of the fracture toughness can have a significant impact to very small PoFs. In the literature approaches are available which describe this K_{Ic} lower bound modeling based on micro mechanical considerations [18; 19] which might be used in the future to get a more realistic estimate for a potential lower bound.

The fatigue crack growth has been modeled as a fully correlated process where only the C parameter is random. Given the used Paris-law, the probabilistic modeling can be improved with regard to the data fitting procedure, since a scatter in the m

parameter is expected. The Paris law and all other models based on this are heuristic modeling approaches which assume a continuous crack growth. A more physical way of modeling the crack growth might be the use of stochastic differential equations describing the crack growth as a non continuous stochastic process [43; 44].

In the presented assessments, the material properties have been described by one scaling function in conjunction with a residual distribution. In principle this approach misses the uncertainty related to the uncertainty of the scale function. As these uncertainties in the scaling function for large datasets are much smaller than the scatter of the assumed residuals in the simulation, this has only a small impact on the overall PoF and can be described in an effective manner by an increased residual scatter. Further, it should be noted that due to the aforementioned modeling of the scatter, the overall approach is conservative, as desired.

Due to the lack of data, it was only possible to account for correlations between the different tensile material properties such as yield and ultimate strength as well as elastic modulus. For instance, it might be that a high fracture toughness value correlates with a smaller crack growth rate. In such a case the current approach would be conservative as it allows for small fracture toughness values and high crack growth rates at the same time. Unless there is evidence for strong correlation the approach of independent scatter of input variables will give conservative results for low PoF as all possible failure regions in phase space can be accessed by pure combinatorics. In general the fracture toughness increases with temperature as well as the crack growth rate, therefore the presented uncorrelated approach is conservative.

Another possible improvement is related to the ultrasonic properties and their modeling. In the current approach, the PoD for the whole component is estimated in a conservative way by assuming the worst possible PoD location representing the whole component. It is well known that the PoD is dependent on the material, the geometry and the length of the sound path [17]. Based, for instance, on the TVT, the PoD can be modeled as a location dependent random variable, where the random process accounts for the variation of the threshold value at a certain position within the component. As this information is available from the ultrasonic testing, a technical implementation is possible.

One very important aspect of the ultrasonic modeling is the conversion factor distribution of natural flaws and their indication size. In conjunction with the TVT it is a very central aspect of the ultrasonic modeling as it influences the size distribution of the real flaws and the PoD alike. Furthermore, the conversion factor distribution is influenced by many different parameters such as the flaw type, shape, orientation, roughness, scan types, scan directions, etc.. As it is very expensive to measure even

single values for this conversion factor, the amount of available data is very limited. In general it is assumed that the conversion factor is not dependent on the forging process or the material. As the conversion factor distribution depends on many factors, it is very unlikely that this is strictly the case. It is desirable to measure or simulate the conversion factor distribution for different materials to assure that this assumption is correct. In principle it is possible to simulate the ultrasonic wave propagation through the steel and account for the geometrical influences of the component. Thus, a local PoD and a local conversion factor can be calculated. The problem with such an approach is that the PoD and the conversion factor also depend on the geometry and impedance difference between the flaw and surrounding matrix. As these parameters are in general unknown, they can be described by a distribution. To set up such an approach, more information about the different types of flaws and their occurrence probability is needed.

In the described approach strong idealizations are used to describe the fracture mechanics, i.e. the flaw embedded in a plate geometry, stress controlled boundary conditions, elliptic or semi-elliptic cracks and all cracks are mode I. The geometry and the boundary conditions can be described more accurately by means of FE simulations. In such a simulation the aforementioned idealizations can be neglected and more realistic results can be revealed. Especially the consideration of strain controlled boundary conditions can improve the result accuracy and decreases the conservatism of the pure stress controlled cracks, as strain controlled cracks can reduce their crack growth rate or stop before failure. As these FE simulations of cracks are very time consuming, it cannot be directly implemented in the described approach. This is in particular needed for the extension to geometrically more involved components such as blades and vanes where the thermal stresses are becoming more important. However a component specific location dependent SIF solution can be pre-calculated with the aforementioned FE approach.

Further improvement in the fracture mechanics modeling might be possible in the future due to further progress of multi-scale simulation approaches with atomistic resolutions at the crack tip, as the crack advancement occurs at this scale, polycrystal model on the crack length scale and continuum based approaches like FE to describe the component geometry. Besides the large computational time consumed by such approaches, the coupling of the different simulation scales still poses a challenge.

Both described approaches are still subject to research, and currently limited to single crack assessments, but with continuously increasing computational potential it might be possible to account for such sophisticated modeling approaches in a probabilistic fracture mechanics approach to some extent.

The presented work treats stress and temperature fields in the assessed components as deterministic as in general the uncertainty of these values is unknown. The scatter in the stress and temperature fields can have a significant impact on the calculated PoF. In this work only generic assumptions about the scatter in stress and temperature have been made without direct connection to the real scatter in the components. This uncertainty is driven by material property scatter (Young's modulus, specific heat capacity, heat conductivity, etc.) and by unknown variations of the thermal boundary conditions (heat transfer coefficient, gas temperature, etc.) of the FE simulation. To tackle this, a stochastic FEA has to be conducted. As of today, stochastic FEA is not state of the art, hence these uncertainties cannot be accounted for in such a way. A workaround might be a parametric FEA study by varying the potential influence factors. In the present form, typically conservative FEA cold start scenarios are utilized.

In the future a more realistic duty cycle analysis can be implemented. These analyzes will consider not only the extreme conservative assumption of a cold start for each start but analyze sequences of multiple cold, warm starts, as well as the other load change operating profiles.

One very interesting approach would be the coupling of the presented framework and a probabilistic approach which describes a crack nucleation process such as low cycle fatigue (LCF), for which a probabilistic approach has already been developed by S. Schmitz et al [53]. Oftentimes subsequent fracture mechanics life beyond the LCF crack initiation is not accounted for, leading to unnecessary conservative procedures and part replacements. Furthermore, all potential failure mechanisms should be accounted for to calculate the total risk of failure. However, oftentimes only a few mechanisms contribute significantly. Other avenues to pursue would be to include stress corrosion crack growth and its nucleation via pit corrosion pockets. This is a very important failure mechanism for steam turbine rotors and hot gas path parts of gas turbines such as blades and vanes.

The presented probabilistic approach has been successfully used in design and life time extension application of Siemens gas turbine rotors. As this rotor design philosophy change can have legal implications not only Siemen's legal was involved, but also externally reviewed by the Allianz Insurance company Center for Technology in Munich Germany. This review was performed in addition to the validation procedures described in the appendix A of this work.

This work is an example that with today's available computational potential it is possible to perform direct simulation Monte Carlo approaches within industrial environments, and not only at research facilities with large supercomputers. Hence, this should be a motivation to develop further high performance computing tools such as probabilistic design methods for other failure mechanisms or optimization processes in order to perform more reliable designs and risk management.

Bibliography

[1] SINTAP: Structural Integrity Assessment Procedure for European Industry. Technical Report BE95-1426, British Energy Generation, 1999.

[2] Norm ISO 21789 Gas turbine applications - Safety, 02 2009.

[3] R. Abinger, F. Hammer, and J. Leopold. Großschaden an einem 330-MW-Dampfturbosatz. *Der Maschinenschaden*, 61:58–60, 12 1988. URL `http://www.gwp.eu/fileadmin/seiten/download/AZT_Veroeffentlichung_Irschingwelle_T.pdf`. visited: 30.03.2012.

[4] Christian Amann and Kai Kadau. Numerically efficient modified runge-kutta solver for fatigue crack growth analysis. *Engineering Fracture Mechanics*, 161: 55 – 62, 2016. ISSN 0013-7944. doi: http://dx.doi.org/10.1016/j.engfracmech.2016.03.021. URL `http://www.sciencedirect.com/science/article/pii/S0013794416301114`.

[5] T. L. Anderson. *Fracture Mechanics Fundamentals and Applications*. CRC Press, 2005.

[6] E. Atroshchenko, S. Potapenko, and G. Glinka. Stress intensity factor for an embedded elliptical crack under arbitrary normal loading. *International Journal of Fatigue*, 31:1907–1910, 2009.

[7] Christina Berger and E. Maldfeld. Fehler in Gasturbinenscheiben bruchmechanisch bewerten: Prof. Dr.-Ing. habil. Dr.e.h. Horst Blumenauer zum 65. Geburtstag. *Materialprüfung*, 42:S. 26–30, Januar 2000. URL `http://tubiblio.ulb.tu-darmstadt.de/14949/`.

[8] Christina Berger, Georg Blauel, Ludvik Hodulak, Britta Pyttel, and Igor Varfolomeyev. Bruchmechanischer Festigkeitsnachweis für Maschinenbauteile. Technical report, Forschungskuratorium Maschinenbau e. V., 2009.

[9] Marion C. Blakey. Safety Recommendation. Technical report, National Transportation Safety Board, 2006.

[10] Nuclear Regulatory Commission. Standard review plan for the review of safety analysis reports for nuclear power plants, 2007.

[11] E1820-08a. Standard Test Method for Measurement of Fracture Toughness.

[12] Mark T. EricksonKirk and MarjorieAnn EricksonKirk. Use of a Unified Model for the Fracture Toughness of Ferritic Steels in the Transition and on the Upper Shelf in Fitness-for-Service Assessment and in the Design of Fracture Toughness Experiments. *ASME Conference Proceedings*, 2006(47543):529–533, 2006. doi: 10.1115/PVP2006-ICPVT-11-93652. URL `http://link.aip.org/link/abstract/ASMECP/v2006/i47543/p529/s1`.

[13] Royce G. Forman and Sambi R. Mettu. Behavior of surface and corner cracks subjected to tensile and bending loads in Ti-6Al-4V alloy. Technical Report NASA-TM-102165, S-611, NASA Johnson Space Center; Houston, TX, United States, September 1990. URL `http://ntrs.nasa.gov/archive/nasa/casi.ntrs.nasa.gov/19910009960.pdf`.

[14] G. Glinka and G. Shen. Universal features of weight functions for cracks in mode I. *Engineering Fracture Mechanics*, 40(6):1135 – 1146, 1991. ISSN 0013-7944. doi: 10.1016/0013-7944(91)90177-3. URL `http://www.sciencedirect.com/science/article/pii/0013794491901773`.

[15] D. Gross and Th. Seelig. *Bruchmechanik Mit einer Einführung in die Mikromechanik*. Springer-Verlag, 2007.

[16] Peter Gumbsch, Joachim Riedle, Alexander Hartmaier, and Helmut F. Fischmeister. Controlling Factors for the Brittle-to-Ductile Transition in Tungsten Single Crystals. *Science*, 282:1293–1295, 1998. URL `http://www.sciencemag.org/content/282/5392/1293.abstract`.

[17] Yan Guo. *The new methods on NDE systems pod capability assessment and robustness improvement*. PhD thesis, Wayne State University, 2009.

[18] V. Hardenacke, J. Hohe, V. Friedmann, and D. Siegele. Enhancement of local approach models for the assessment of cleavage fracture based on micromechanical investigations. In *Proceedings of the 18th European Conference on Fracture*, 2010.

[19] V. Hardenacke, J. Hohe, V. Friedmann, and D. Siegele. Enhancement of local approach models for assessment of cleavage fracture consider-ing micromechanical effects. Technical report, IWM Freiburg, 2011.

[20] S. Hasse. *Guss- und Gefuegefehler*. Schiel & Schoen GmbH, 2003.

[21] E. J. Hearn. *Mechanics of Materials 2*. Number 0750632666. Butterworth-Heinemann, 3 edition, 1997.

[22] Leonhard Held. *Methoden der statistischen Inferenz*. Spektrum Akademischer Verlag, 2008.

[23] G. R. Irwin. Analysis of stresses and strains near the end of a crack traversing a plate. *Journal of Applied Mechanics*, 24:361–364, 1957.

[24] G. R. Irwin. Linear Fracture Mechanics, Fracture Transition, and Fracture Control. *Engineering Fracture Mechanics*, 1:241–257, 1968.

[25] M. Janssen, J. Zuidema, and R. J. H. Wanhill. *Fracture Mechanics 2nd Edition*. VSSD, 2002-2006.

[26] H.-A. Jestrich, W. Prestel, D. Heinrich, and W. Schmalenbeck. Die Bedeutung der Ultrschall-Ersatzreflektorgröße für die Bruchmechanik, untersucht an schweren Schmiedestücken für Turbomaschinen. *Materialprüfung*, 29:13–16, 1987.

[27] Kai Kadau, Timothy C. Germann, S. Lomdahl, Peter, and Brad Lee Holian. Microscopic View of Structural Phase Transitions Induced by Shock Waves. *Science*, 296:1681–1684, 2002. URL `http://www.sciencemag.org/content/296/5573/1681.abstractl`.

[28] Kai Kadau, Charles Rosenblatt, John L. Barber, Timothy C. Germann, Zhibin Huang, Pierre Carlès, and Berni J. Alder. The importance of fluctuations in fluid mixing. *Proceedings of the National Academy of Sciences*, 104(19):7741–7745, 2007. doi: 10.1073/pnas.0702871104. URL `http://www.pnas.org/content/104/19/7741.abstract`.

[29] T.-U. Kern, J. Ewald, and K Maile. Evaluation of NDT-signals for use in the fracture mechanics safety analysis. In *Material at high temperatures, creep and fatigue crack growth in high temperature plant, international HIDA conference*, 1998.

[30] J. Krautkrämer. Fehlergrößenermittlung mit Ultraschall. *Archiv für Eisenhüttenwesen*, 30:693–703, 1959.

[31] Josef Krautkrämer, J.krämer and Josef Krautkämer. *Werkstoffprüfung mit Ultraschall*. Springer-Verlag Berlin Heidelberg, 1986.

[32] B. Z. Margolin, A. G. Gulenko, V. A. Nikolaev, and L. N. Ryadkov. A new engineering method for prediction of the fracture toughness temperature dependence for RPV steels. *International Journal of Pressure Vessels and Piping*, 80(12): 817 – 829, 2003. ISSN 0308-0161. doi: DOI:10.1016/j.ijpvp.2003.12.005. URL http://www.sciencedirect.com/science/article/pii/S0308016103002114.

[33] George Marsaglia and John Marsaglia. Evaluating the Anderson-Darling Distribution. *Journal of Statistical Software*, 9(2):1–5, 2 2004. ISSN 1548-7660. URL http://www.jstatsoft.org/v09/i02.

[34] George Marsaglia, Wai Wan Tsang, and Jingbo Wang. Evaluating kolmogorov's distribution. *Journal of Statistical Software*, 8(18):1–4, 11 2003. ISSN 1548-7660. URL http://www.jstatsoft.org/v08/i18.

[35] Y. Murakami. *Stress intensity factors*. Pergamon Books Inc.,Elmsford, NY, 1987 Jan 01.

[36] Masayuki Nakao. Brittle Fracture of Turbine Rotor in Nagasaki. http://www.sozogaku.com/fkd/en/hfen/HA1000601.pdf, October 1970. URL http://www.sozogaku.com/fkd/en/hfen/HA1000601.pdf. visited: 27.03.2012.

[37] Masayuki Nakao. Fracture of Turbine Shaft in Wakayama. http://www.sozogaku.com/fkd/en/hfen/HA1000602.pdf, June 1972. URL http://www.sozogaku.com/fkd/en/hfen/HA1000602.pdf. visited: 27.03.2012.

[38] J. C. Newman and I. S. Raju. Prediction of fatigue-crack growth patterns and lives in three-dimensional cracked bodies. Technical report, National Aeronautics and Space Administration, 1984.

[39] Jr. J.C. Newman and I.S. Raju. An empirical stress-intensity factor equation for the surface crack. *Engineering Fracture Mechanics*, 15(1-2):185 – 192, 1981. ISSN 0013-7944. doi: 10.1016/0013-7944(81)90116-8. URL http://www.sciencedirect.com/science/article/pii/0013794481901168.

[40] J. C. Newmann Jr. and Raju. Stress-Intensity Factor equations for cracks in three-dimensional bodies subjected to tension and bending loads. Technical report, Mational Aeronautics and Space Administration, 1984.

[41] Akito Nitta and Hideo Kobayashi. Burst of Steam Turbine Rotot in Nuclear Power Plant. http://www.sozogaku.com/fkd/en/hfen/HB1031029.pdf, September 1969. URL http://www.sozogaku.com/fkd/en/hfen/HB1031029.pdf.

[42] Akito Nitta and Hideo Kobayashi. Burst of Steam Turbine Rotor in Fossil Power Plant. http://www.sozogaku.com/fkd/en/hfen/HB1031027.pdf, June 1974. URL http://www.sozogaku.com/fkd/en/hfen/HB1031027.pdf. visited: 27.03.2012.

[43] Keith Ortiz and Anne S. Kiremidjian. Time series analysis of fatigue crack growth rate data. *Engineering Fracture Mechanics*, 24(5):657 – 675, 1986. ISSN 0013-7944. doi: 10.1016/0013-7944(86)90241-9. URL http://www.sciencedirect.com/science/article/pii/0013794486902419.

[44] Keith Ortiz and Anne S. Kiremidjian. Stochastic modeling of fatigue crack growth. *Engineering Fracture Mechanics*, 29(3):317 – 334, 1988. ISSN 0013-7944. doi: 10.1016/0013-7944(88)90020-3. URL http://www.sciencedirect.com/science/article/pii/0013794488900203.

[45] P. Paris and F. Erdogan. A Critical Analysis of Crack Propagation Laws. *Journal of Basic Engineering*, 85(4):528–533, 1963. doi: 10.1115/1.3656900. URL http://link.aip.org/link/?JBE/85/528/1.

[46] I. S. Raju and J. C. Newmann Jr. Stress intensity factors for a wide range of semi-elliptical surface cracks in finite-thickness plates. *Engineering Fracture Mechanics*, 11:817–829, 1979.

[47] J. R. Rice. A Path Independent Integral and the Approximate Analysis of Strain Concentration by Notches and Cracks. *Jounral of Applied Mechanics*, Vol. 35: 379–386, 1968.

[48] H. A. Richard and M. Sander. *Ermüdungsrisse Erkennen, sicher beurteilen, vermeiden.* Vieweg+Teubner, 2009.

[49] R.O. Ritchie. Mechanisms of fatigue-crack propagation in ductile and brittle solids. *International Journal of Fracture*, 100:55–83, 1999.

[50] J. Rösler, H. Harders, and M. Bäker. *Mechanisches Verhalten der Werkstoffe.* Vieweg+Teubner, 2008.

[51] C. Runge. Über die numerische Auflösung von Differentialgleichungen. *Math. Ann.*, 46:167–178, 1895.

[52] M. Sander. *Sicherheit und Betiebsfestigkeit von Maschinen und Anlagen.* Springer Berlin / Heidelberg, 2008.

[53] S. Schmitz, H. Gottschalk, G. Rollmann, and R. Krause. A PROBABILSTIC APPROACH TO LOW-CYCLE FATIGUE. In *Proceedings of ASME Turbo Expo 2013.* ASME, June 2013. San Antonio, USA.

[54] D P Schwant, R C | Timo. Life assessment of general electric large steam turbine rotors. In R. Viswanathan, editor, *Life Assessment and Improvement of Turbo-Generator Rotors for Fossil Plants*, pages 3.25–3.40, New York, 1985. Pergamon Press.

[55] G. Shen and G. Glinka. Weight functions for a surface semi-elliptical crack in a finite thickness plate. *Theoretical and Applied Fracture Mechanics*, 15(3):247 – 255, 1991. ISSN 0167-8442. doi: 10.1016/0167-8442(91)90023-D. URL `http://www.sciencedirect.com/science/article/pii/016784429190023D`.

[56] *DARWIN 7.1 Users' Manual*. South West Research Institute, San Antonio Texas, 7.1 edition, July 2012.

[57] *NASGRO 6.2 Reference Manual*. Southwest Research Institue, September 2011.

[58] Werner A. Stahel. *Statistische Datenanalyse*. Vieweg+Teubner, 2008.

[59] V.A. Vainshtok and I.V. Varfolomeyev. Stress intensity factor equations for part-elliptical cracks and their verification. *Engineering Fracture Mechanics*, 34(1): 125 – 136, 1989. ISSN 0013-7944. doi: 10.1016/0013-7944(89)90246-4. URL `http://www.sciencedirect.com/science/article/pii/0013794489902464`.

[60] I. Varfolomeev, D Ivanov, and L. Hodulak. *IWM VERB Failure Assessment Software 8.0 Compendium of Stress Intensity Factor and Limit Load Solutions*. Fraunhofer IWM, December 2008.

[61] I. Varfolomeev, D Ivanov, and L. Hodulak. *IWM VERB Failure Assessment Software 8.0 User' Guide*. Fraunhofer IWM, December 2008.

[62] H.-W Viehrig, J Boehmert, and J Dzugan. Some issues by using the master curve concept. *Nuclear Engineering and Design*, 212(1-3):115 – 124, 2002. ISSN 0029-5493. doi: http://dx.doi.org/10.1016/S0029-5493(01)00465-4. URL `http://www.sciencedirect.com/science/article/pii/S0029549301004654`.

[63] J. Vrana, A. Zimmer, K. Bailey, R. Angal, P. Zombo, U. Büchner, A Buschmann, R.E. Shannon, H.-P. Lohmann, and W. Heinrich. Evolution of the ultrasonic inspection requirements of heavy rotor forgings over the past decade. *Review of Quantitative Nondestructive Evaluation*, 29:1623–1630, 2010.

[64] K. Wallin. The master curve method: a new concept for brittle fracture. *International Journal of Materials and Product Technology*, 14:342–354, 1999. doi: doi:10.1504/IJMPT.1999.036276. URL `http://www.ingentaconnect.com/content/ind/ijmpt/1999/00000014/F0020002/art00014`.

[65] X. Wang and S.B. Lambert. Local weight functions for semi-elliptical surface cracks in finite thickness plates. *Theoretical and Applied Fracture Mechanics*, 23 (3):199 – 208, 1995. ISSN 0167-8442. doi: 10.1016/0167-8442(95)00022-7. URL http://www.sciencedirect.com/science/article/pii/0167844295000227.

[66] Christina Weichert. *Auswirkungen eines dreiachsigen Spannungszustandes auf das Verformungsverhalten und das Rissinitiierungsverhalten von Gruppenfehlstellen*. PhD thesis, Fakultaet Maschinenbau der Universitaet Stuttgart, 2004.

[67] J.N. Yang, G.C. Salivar, and C.G. Annis Jr. Statistical modeling of fatigue-crack growth in a nickel-base superalloy. *Engineering Fracture Mechanics*, 18(2):257 – 270, 1983. ISSN 0013-7944. doi: DOI:10.1016/0013-7944(83)90137-6. URL http://www.sciencedirect.com/science/article/pii/0013794483901376.

[68] A. Zimmer, J. Vrana, J. Meiser, W Maximini, and N. Blaes. EVOLUTION OF THE ULTRASONIC INSPECTION OF HEAVY ROTOR FORGINGS OVER THE LAST DECADES. In *Review of progress in quantitative nondestructive evaluation Volume 29*, 2010.

A. Validation of ProbFM

As the acceptable risk for gas turbine rotor disks is very small, in the order of $1e-4/year$, the PoF which has to be resolved is also very small. A very large data set, $\geq 10^5$ samples, needs to be assessed in order to validate a probabilistic fracture mechanics approach directly. For aero-engines there is a large set of service data available which was used to validate and calibrate the DARWIN code. For the *ProbFM* methodology a multi-step validation process was sought which will be described in the following.

The fracture module was validated against the commercially available fracture mechanics codes IWM VERB and NASGRO. Furthermore, the specific fracture mechanics conditions of gas turbine disks have been experimentally validated against LEFM approaches which are implemented in *ProbFM* and IWM VERB. Additionally, a simple disk model was evaluated with DARWIN and *ProbFM* and the results were compared.

A.1. Validation of the Crack Growth Module

In order to validate the crack growth module implemented in *ProbFM*, crack growth has been compared to the two deterministic fatigue crack growth calculation tools IWM VERB 8.0 and NASGRO 6.2.

Randomly chosen sets of input parameters, based on relevant component conditions, have been assessed with *ProbFM*. The same calculations have been done with the aforementioned commercial codes and the results have been compared.

The relative life-cycle difference $\epsilon_{N\,r}$ (A.1) and the absolute life-cycle difference ϵ_N (A.2) to failure have been calculated.

$$\epsilon_{N\,r} = 1 - \frac{N_{ProbFM}}{N_{ref}} \tag{A.1}$$

$$\epsilon_N = N_{ref} - N_{ProbFM} \tag{A.2}$$

N_{ProbFM} and N_{ref} are the numbers of cycles to failure calculated by *ProbFM* and the tool used for comparison.

The integration step size in *ProbFM* has been set to 10 cycles as this is a typical step size in stationary gas turbine *PoF* assessments and more than sufficient to provide a converged result.

A.2. Validation of the Deterministic Crack Growth Calculation in ProbFM with IWM VERB

In *ProbFM*, SIF solutions for the embedded (Solution 1 [59]) and surface (Solution 3 [65]) elliptic cracks from IWM VERB are implemented. A large number of crack growth calculations have been performed with *ProbFM* as well as with IWM VERB 8.0. All these calculations have been carried out with pure membrane stress. In order to make it possible to perform more than 1000 of crack growth calculations with different parameters, a Visual Basic script has been developed to pilot IWM VERB 8.0. As it is not possible to change the crack growth rates in IWM VERB with the script, these have been kept constant.

Four different cases have been investigated with IWM VERB 8.0:

- Embedded Crack
- Embedded Crack with FAD
- Surface Crack
- Surface Crack with FAD

The calculations have been done with an integration step size of 1, since IWM VERB 8.0 uses a simple Euler integration scheme which converges slowly. As the number of intermediate steps is limited, it is not possible to get the numerically exact results from IWM VERB 8.0. Therefore, only effective step sizes of 12.5 up to 100 cycles depending on the calculation are available in the output files. In case of the FAD assessment calculations (effective step sizes of 50 and 100 cycles) the failure cycle is linearly interpolated between the last safe and the first unsafe crack configuration and by this the scatter in the failure cycle difference is reduced. Each calculation has been done with different combinations a_0, c_0, σ_{max}, σ_{min}, K_{Ic}, σ_{RM}, σ_{YS} and E in order to test a large parameter space. The plate size has been chosen large compared to the crack size and thus no finite plate size effects are observed in the comparison.

A.2.1. Elliptic Embedded Crack

In *ProbFM* an embedded crack SIF solution is available which is comparable to Solution 1 [59] in IWM VERB 8.0. The solutions in *ProbFM* and IWM VERB have been

compared with LEFM and FAD mode, without stress gradients and quasi-infinite plate sizes.

Embedded Crack LEFM

The elliptic embedded crack LEFM calculations have been done with a plate model and the settings given in table A.1. The results are shown in Figure A.1. The calculated failure cycle differences are smaller than the effective step size for this calculations. Therefore, it can be concluded that IWM VERB and *ProbFM* produce the same results within the calculation accuracy for embedded elliptic cracks within LEFM approximation.

IWM VERB options	
Integration algorithm	Euler
Integration Steps	10000
Number of Cycles	20000
Number of results in Output	800
Effective Step Size	25
Crack type	Elliptic embedded
SIF Solution	1
Plate width	5000 mm
Wall thickness	2000 mm
Number of calculations	114
IWM VERB calculation time	$\approx$ 2 h

Table A.1.: IWM VERB settings for the embedded crack with LEFM calculations

Elliptic Embedded Crack FAD

The elliptic embedded crack calculations with FAD have been done with a plate model and the settings from table A.2. As the failure cycle is estimated by linear interpolation of the LEFM results, the difference between the failure cycles is significantly smaller than the effective step size. All calculated failure cycle differences are within the effective integration step size (Figure A.2), and thus IWM VERB and *ProbFM* are calculating the same number cycle to failure for the case of FAD as well.

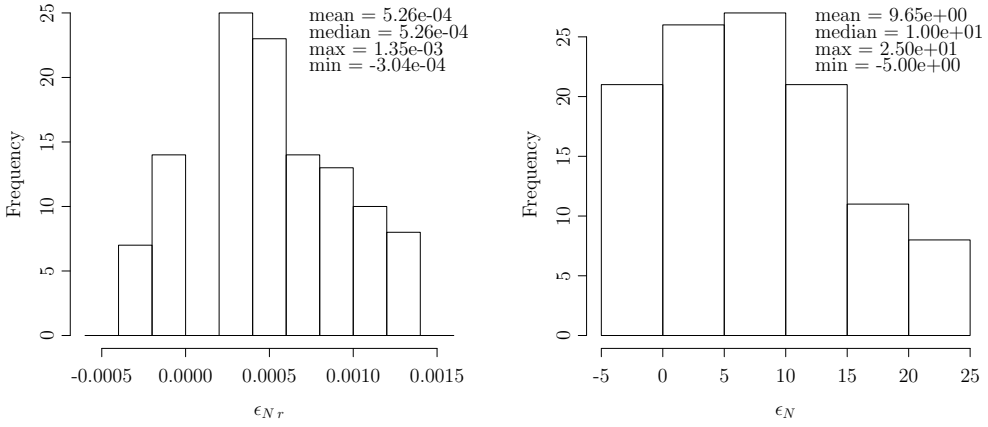

(a) Relative life cycle difference

(b) Absolute life cycle difference

Figure A.1.: Comparison of calculated life cycle differences in IWM VERB and *ProbFM* of embedded elliptic cracks with LEFM

IWM VERB options	
Integration algorithm	Euler
Integration Steps	10000
Number of Cycles	20000
Number of results in Output	200
Effective Step Size	100
Crack type	Elliptic embedded
SIF Solution	1
Limit Load Solution	1
Plate width	5000 mm
Wall thickness	2000 mm
Number of calculations	56
IWM VERB calculation time	$\approx$ 1 h

Table A.2.: IWM VERB settings for the embedded crack with FAD calculations.

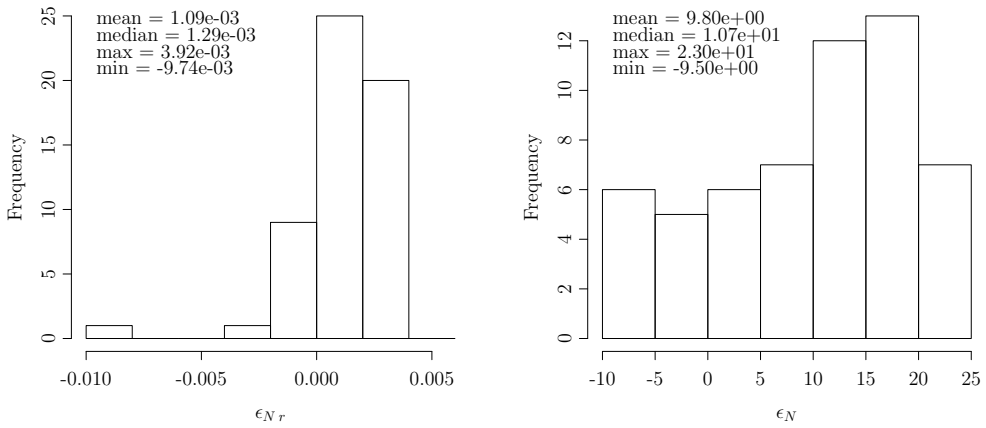

(a) Relative life cycle difference

(b) Absolute life cycle difference

Figure A.2.: Relative life cycle difference of the embedded cracks. (FAD IWM VERB vs. *ProbFM*)

A.2.2. Semi Elliptic Surface Crack

In *ProbFM*, a semi elliptic surface crack SIF solution is available corresponding to Solution 3 [65] in IWM VERB 8.0. The solution in *ProbFM* and IWM VERB have been compared with LEFM and FAD mode, without stress gradients and quasi infinite plate sizes.

Semi Elliptic Surface Crack LEFM

The semi elliptic surface crack LEFM calculations have been done with a plate model and the settings from table A.3. The results are shown in Figure A.3 and all calculated failure cycle differences are smaller than the effective step size. Within the calculation accuracy the results from IWM VERB and *ProbFM* are equivalent.

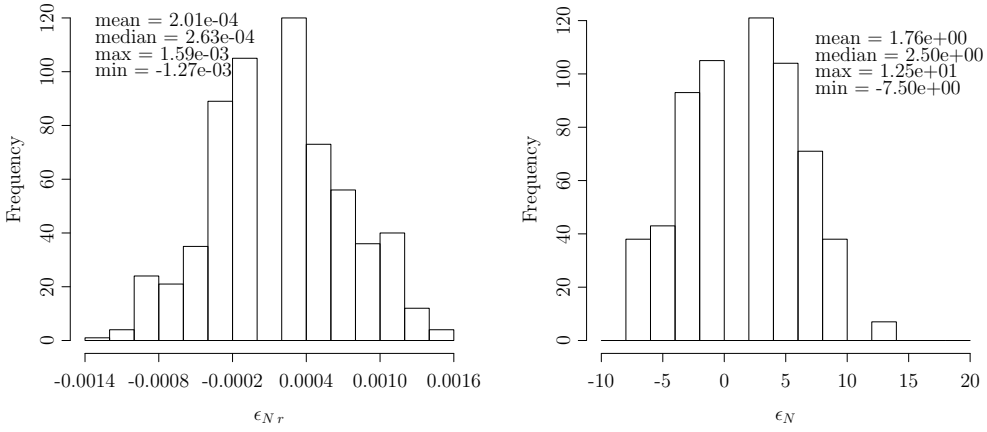

(a) Relative life cycle difference

(b) Absolute life cycle difference

Figure A.3.: Relative life cycle difference surface crack IWM VERB *ProbFM*

IWM VERB options	
Integration algorithm	Euler
Integration Steps	10000
Number of Cycles	10000
Number of results in Output	800
Effective Step Size	12.5
Crack type	Semi-elliptical
SIF Solution	3
Plate width	5000 mm
Wall thickness	2000 mm
Number of calculations	620
IWM VERB calculation time	$\approx$ 12 h

Table A.3.: IWM VERB settings for the semi elliptic surface Crack with LEFM calculations.

Semi Elliptic Surface Crack FAD

The semi elliptic surface crack calculations with FAD have been done with a plate model and the settings from table A.4. As the failure cycle is estimated by linear interpolation of the LEFM results, the difference between the failure cycles is significantly smaller than the effective step size. All calculated failure cycle differences are within the effective integration step size (Figure A.4).

IWM VERB options	
Integration algorithm	Euler
Integration Steps	10000
Number of Cycles	10000
Number of results in Output	200
Effective Step Size	50
Crack type	Semi-elliptical
SIF Solution	3
Limit Load Solution	1
Plate width	5000 mm
Wall thickness	2000 mm
Number of calculations	298
IWM VERB calculation time	$\approx$ 6 h

Table A.4.: IWM VERB settings for the semi elliptic surface crack with FAD calculations

A.3. Deterministic Validation of ProbFM with NASGRO

An additional set of SIF solutions has been implemented in *ProbFM* which is based on the EC05 and SC17 SIF solutions of NASGRO 6.2. The advantage of the SIF solutions in NASGRO compared to the SIF solutions in IWM VERB is that the $\frac{a}{c}$ ratio can be greater than 1, which is needed for the crack transition models. For comparison, a simple geometry with a simple stress field has been used (Figure A.5a). The geometry has a width of 0.5m and a thickness of 0.3m. The stress field is a linear function from 900MPa to 450MPa as shown in Fig. A.5.

For convenience only a single crack growth rate curve without scatter has been used. In total, 255 different crack geometries have been simulated for comparison with NASGRO.

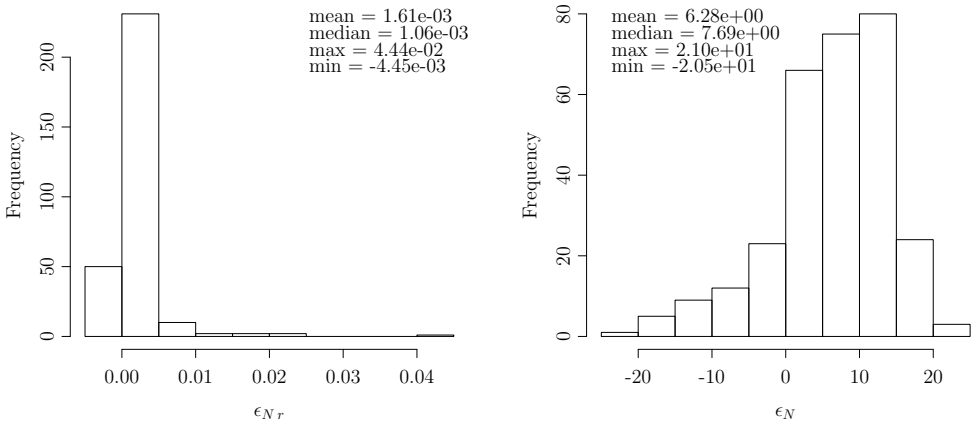

(a) Relative life cycle difference

(b) Absolute life cycle difference

Figure A.4.: Relative life cycle difference plot for surface crack comparison with FAD of IWM VERB and *ProbFM*

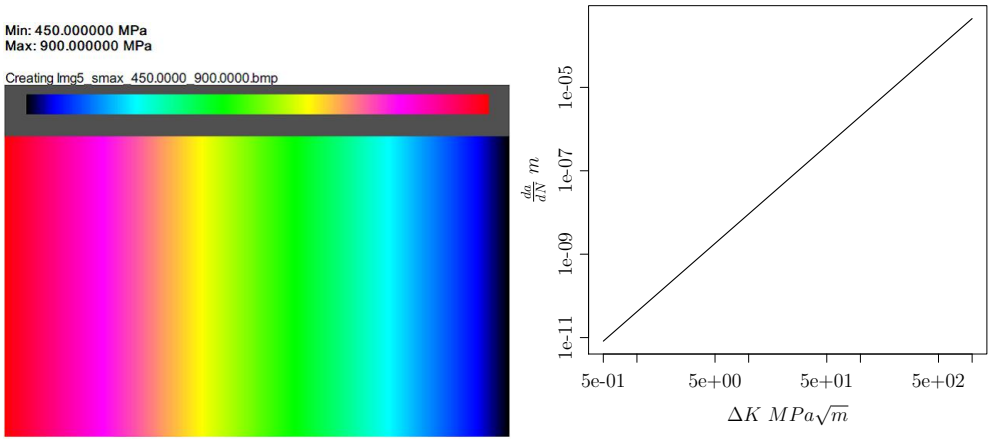

(a) Stress field used for NASGRO - *ProbFM* comparison

(b) Crack growth rate curve used for NASGRO - *ProbFM* comparison

Figure A.5.: Boundary conditions used for NASGRO - *ProbFM* comparison

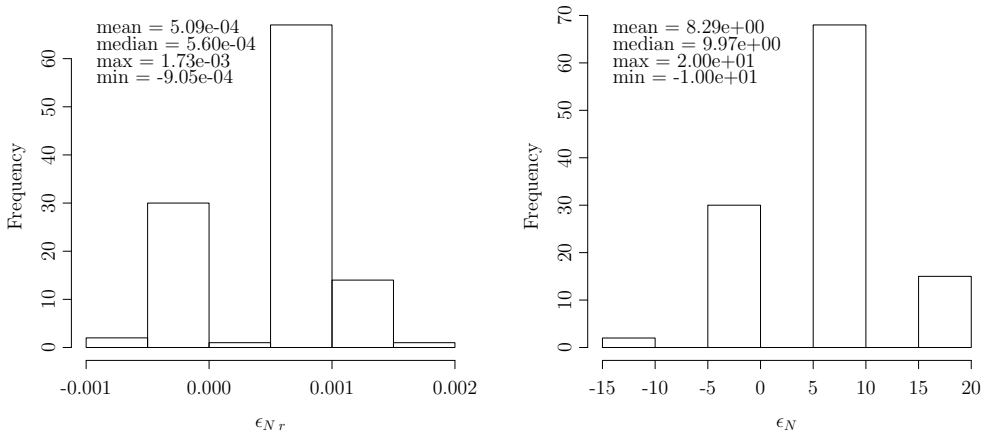

(a) Relative life cycle difference

(b) Absolute life cycle difference

Figure A.6.: Comparison of calculated life cycle differences in NASGRO and *ProbFM* for embedded cracks and pure membrane stress

A.3.1. Embedded Elliptic Cracks without Surface Crack Transition

The simulated cracks in this section do not transit into a surface crack before they cause a failure of the component. The crack growth calculation is influenced by membrane and/or bending stress and the crack center to surface distance.

Embedded Elliptic Crack with pure Membrane Stress

115 of the simulated Cracks are with pure membrane stress and without crack transition to a surface crack. The failure cycle differences are shown in Figure A.6. Within the calculation accuracy, the results are equal. Furthermore,*ProbFM* tends to yield the more conservative results, mean of $\epsilon_N \geq 0$, because of the used modified integration scheme.

Embedded Elliptic Crack with Membrane and Bending Stress

About 120 embedded cracks with stress gradient have been compared as shown in Figure A.7. As in *ProbFM* only the stress intensity increase due to the gradient is accounted for, the crack growth rate is overestimated compared to the NASGRO

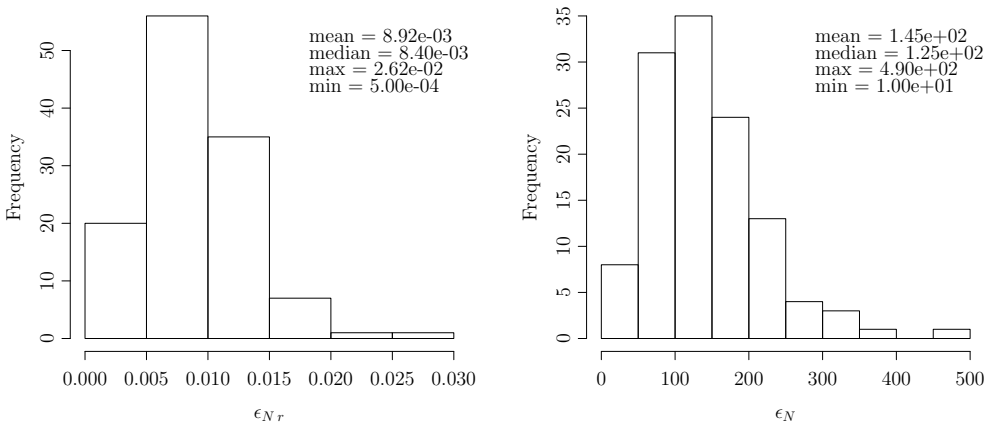

(a) Relative life cycle difference

(b) Absolute life cycle difference

Figure A.7.: Comparison of calculated life cycle differences in NASGRO and *ProbFM* with embedded cracks, membrane and bending stress.

solution. But the relative error in this comparison remains a few percent of the number of cycles to failure. From this point of view the accuracy of the implemented solution is sufficient as the error of the SIF solutions is in the order of 5% and the number of cycles to failure is a conservative estimate of the NASGRO solution.

A.3.2. Pure Semi Elliptic Surface Cracks

This type of crack is very rare in *ProbFM* calculations as it is very unlikely that a crack starts from the first cycle as a surface crack. The majority of cracks stay for at least a few cycles as an embedded crack before they transit into a surface crack. In the test geometry only three of the 255 simulated cracks have been semi-elliptic surface cracks from the beginning. The crack growth calculations have been done without account for the stress gradient. The stress at the crack center has been used as membrane stress since it is currently not implemented in *ProbFM* to use stress gradients for semi-elliptic surface cracks. The results of this 3 calculations are shown in table A.5.

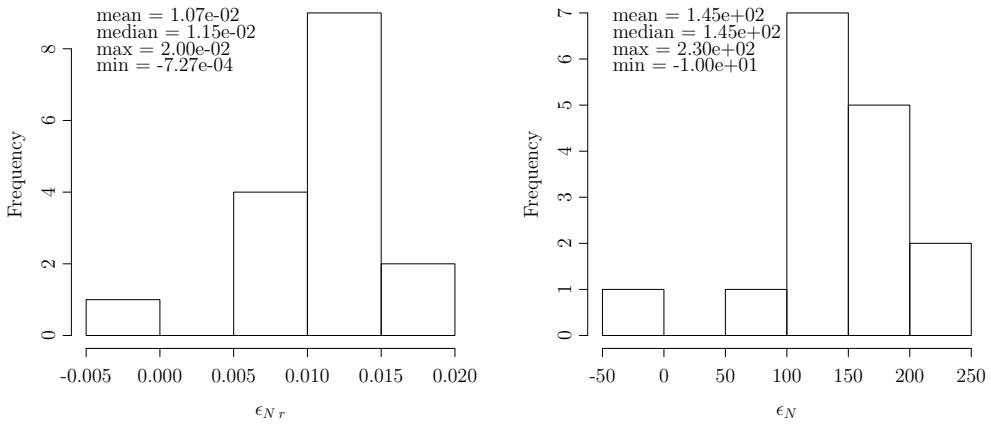

(a) Relative life cycle difference

(b) Absolute life cycle difference

Figure A.8.: Comparison of calculated life cycle differences in NASGRO and *ProbFM* with embedded cracks, pure membrane stress and crack transition

$N_{failure\,NASGRO}$	$N_{failure\,ProbFM}$	Difference ϵ_N	relative Difference $\epsilon_{N\,r}$
17140	17160	-20	-1.17e-3
7720	7730	-10	-1.29e-3
11010	11020	-10	-9.07e-3

Table A.5.: Failure cycles of semi elliptic surface cracks without transition from embedded crack.

A.3.3. Embedded Elliptic Cracks with Surface Crack Transition

One advantage of the NASGRO EC05/SC17 models compared to IWM VERB is the implementation of a crack transition model (subsection 2.6.3). In a probabilistic analysis which integrates over the whole component, a significant part of the calculated cracks will transit from an embedded crack into a surface crack. The results are shown in Figure A.8. *ProbFM* tends to slightly underestimate the failure to cycle compared to NASGRO. As already mentioned in the previous section, the relative accuracy is within the typical accuracy of the SIF solutions, and *ProbFM* yields conservative results compared to NASGRO.

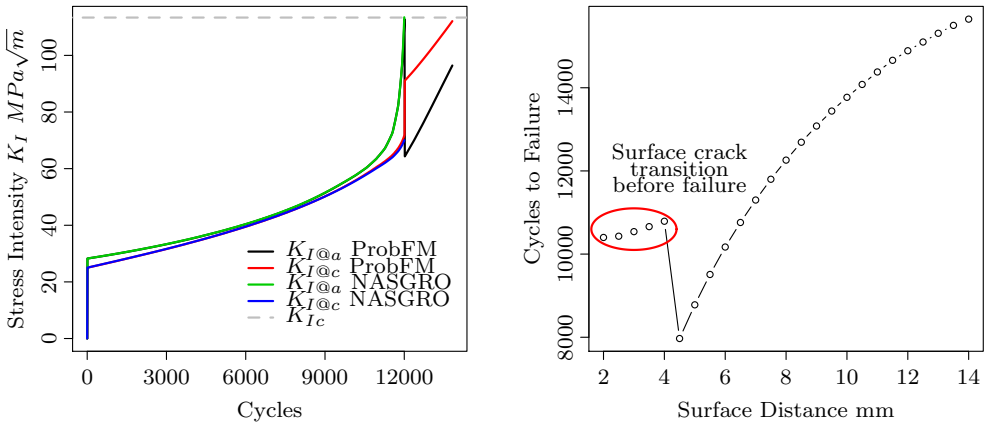

(a) Development of the stress intensity during crack growth and crack transition

(b) Cycles to failure depending on the surface to crack center distanc

Figure A.9.: Unsteady shape of the failure surface of the NASGRO model

Furthermore, there are some effects in the NASGRO crack growth model which are not obvious. In Figure A.9a one case is shown. The stress intensity at the a_1 tip (2.5) in NASGRO reaches the critical crack Fracture toughness 1 cycle before it transits into a surface crack. Due to this a failure is predicted and the calculation is stopped. The same crack in *ProbFM* first reaches the transition criterion and due to this the maximum stress intensity is reduced. In this case the crack life in *ProbFM* is approximately 3000 cycles larger than in NASGRO. This effect can also occur in the other direction and *ProbFM* calculates much shorter life than NASGRO.

The same effect can be shown in NASGRO by calculating the cycles to failure of a crack in a constant stress field as function of the crack center to surface distance (Figure A.9b). Due to the increased stress intensity at the surface facing crack tip a_1, the critical stress intensity K_{Ic} can be reached before the crack transits into a surface crack, even if the stress intensity at the other crack tip is still far below the K_{Ic} value. Due to this modeling approach, cracks which are near to the surface but still do not touch it are more critical than surface cracks. This behavior can be seen in the *ProbFM* failure rate map (Figure A.10) where a narrow region near to the surface

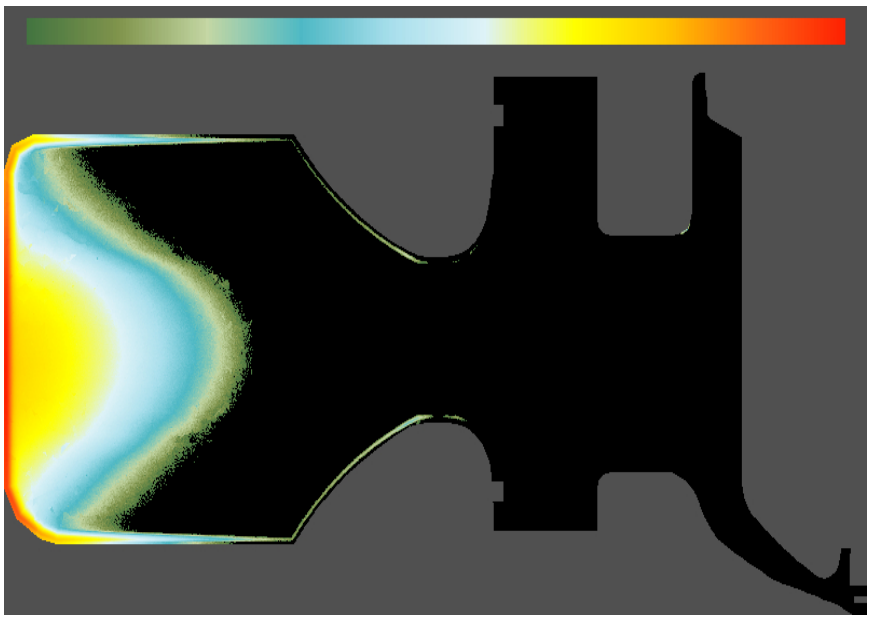

Figure A.10.: *ProbFM* failure rate map with logarithmic scale of a medium risk component. (Figure not to scale.)

has a higher failure risk than the surface itself. Fig. A.9 shows that the NASGRO failure surface is unsteady. In MC integration methods which rely on the steady- and smoothness of the failure surface like FORM or importance sampling severe problems can arise with such unsteady failure surfaces. Another reason for applying a direct MC simulation approach.

A.4. Probabilistic Validation of ProbFM

In this chapter multiple different validations of the probabilistic aspects of *ProbFM* have been performed. The validation includes a risk comparison between the commercially available DARWIN code and *ProbFM*. The latter not only tests the probabilistic module but also the fracture mechanics and stress processing module of *ProbFM*.

A.4.1. Validation of Component Volume Calculation

To calculate the *PoF* of a component, the volume of this component is needed to determine the flaw occurrence rate. With *ProbFM* one can calculate the volume of

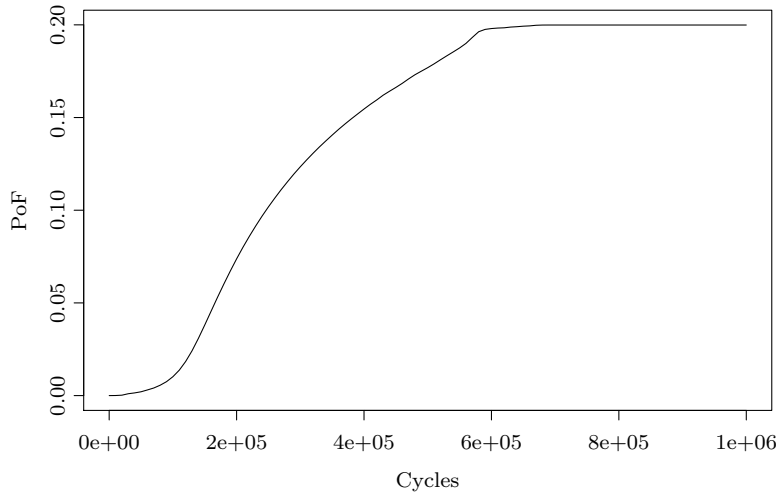

Figure A.11.: Consistency check of PoF of a test component

a component by MC methods. For example ANSYS calculates the volume of the test component with 0.376m^3 and *ProbFM* calculates a volume of 0.378m^3 using 10^9 samples. This is a deviation of about 0.5%. This small deviation is a result of the discrete voxel representation of the component in $ProbFM$.

A.4.2. Validation of Flaws per Component in ProbFM

In order to validate the number of flaws in an component, a simple example has been calculated with *ProbFM*.

For the calculation it is assumed that the KSR occurrence rate is $\rho_{Flaw} = 0.1\frac{Flaw}{m^3}$ with all flaw sizes equal to 1mm^2 and the volume of the component is $V_{Comp} = 1m^3$. The conversion factor is set to $k = 1$, the probability of detection is $PoD = 0.5$ for all flaw sizes and the KSR decision limit is set to the large value of $KSR_{lim} = 100\text{mm}^2$ to accept all forgings. With this assumptions the PoF for an infinite number of cycles can be calculated quite easy by

$$PoF_{limit} = \frac{\rho_{Flaw} V_{Comp}}{PoD} = 0.2 \tag{A.3}$$

ProbFM calculates with the above mentioned assumptions with 10^8 samples after

10^6 Cycles a PoF of $PoF = 0.1999$ (Figure A.11). This is a deviation of 0.05% and is within the numerical accuraccy. The deviation further decreases with an increasing number of samples and cycles.

A.4.3. ProbFM - DARWIN Comparison

DARWIN is a probabilistic fracture mechanics tool which has been developed for the use in the aero-industry with the original scope on the assessment of hard alpha inclusions in titanium rotor disks and is a highly validated tool. The reasons why DARWIN is not used for the land based gas turbines are already discussed in the Introduction.

To compare *ProbFM* and DARWIN, a test case has been set up with comparable inputs in *ProbFM* and DARWIN. As both tools have different capabilities, only a subset of all possible input parameters, such as crack growth rate and flaw density, can be used for comparison. The geometry used for comparison is a simple rotating disk with a hole in the middle. This model has been simulated using ANSYS (Table A.6) and has been meshed with 24 x 8 PLANE183 Elements. In *ProbFM* the calculations have been done with 10^{10} samples on 10 CPUs within 12.5h. The calculations using DARWIN have been done with 10^4 samples per zone on a single CPU using the importance sampling algorithm within 16h (76 zones bivariant).

Property	Value	Unit
Inner Diameter R_i	100	mm
Outer Diameter R_o	1000	mm
Thickness t	300	mm
Young's modulus E	209.9	GPa
Poisson ratio ν	0.285	
Density ρ	7.824	$\frac{\mathrm{g}}{\mathrm{cm}^3}$
Temperature T	15	°C
Frequence f	0-50	Hz

Table A.6.: Input parameters for the finite element analysis of the test component

DARWIN has no capability to find critical stress orientations from the input file, thus the hoop stress has been used for DARWIN and *ProbFM*. The fracture toughness and crack growth rate data tables are limited to 40 temperatures and seven R-ratios in DARWIN. To ensure that the same material properties are used, only a single temperature level is used for comparison.

In DARWIN the component has to be divided manually in several zones. For each zone one 'critical' location has to be defined, in general the highest stressed region is

Figure A.12.: *ProbFM* failure rate map of the DARWIN *ProbFM* comparison model

used, at which a crack representative for the whole zone is placed. This is in general not a trivial task as the critical location can depend on the crack size and shape, as well as the transient stress tensor behaviour. The failure probability of the single zones is calculated based on the failure probability of this chosen 'critical' location. The PoF for the whole component according equation A.4, with PoF_i is the probability of failure of zone i.

$$PoF_{DARWINtotal} = 1 - \prod_{i=1}^{n} (1 - PoF_i) \tag{A.4}$$

As no data for the probabilistic lifing model in DARWIN is available no scatter in the material properties is used. Furthermore, DARWIN has no capability to account for the FAD or the IPZE. Therefore the calculations are done with purely LEFM.

The zone assignment in DARWIN is dependent on the available nodes describing the stress field. In Figure A.13, the zone assignment in the component for up to 36 zones is shown. In Figure A.13a, the zoning is done on the original FEA elements imported from the ANSYS result file. Unfortunately, the FEA mesh density is in general not sufficient to define enough zones to get a converged solution (Figures A.14 and A.15). Therefore, additional elements have to be defined manually by linear interpolation between the available nodes to refine the zones. This manual refinement is extremely time consuming and has poor reproducibility as it depends on the user performing the refinement.

The zone refinement in this case has been done preferably in radial direction and only to some extend in axial direction. The refinement strategy is based on the failure rate map from *ProbFM* (Figure A.12).

Moreover, the graphical user interface to assign the zones becomes very slow if a large number of nodes has to be handled.

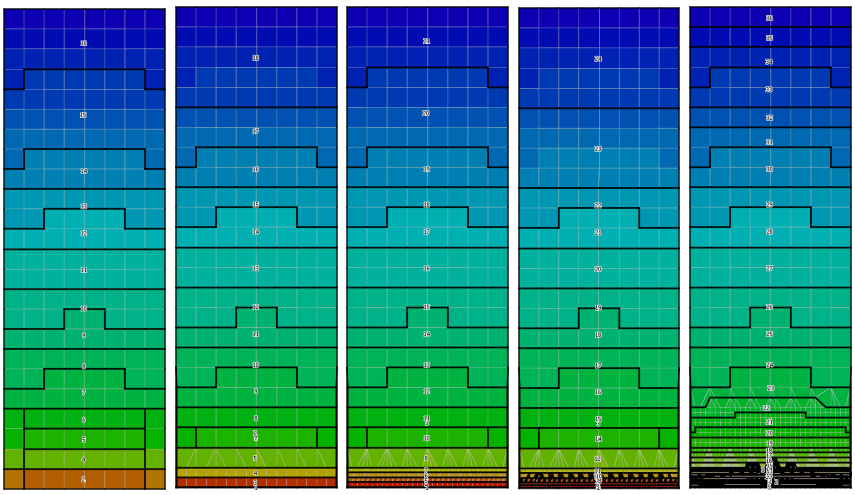

(a) 16 Zones (b) 18 Zones (c) 21 Zones (d) 24 Zones (e) 36 Zones

Figure A.13.: DARWIN component zoning

As *ProbFM* does not need the manual zone definition and mesh refinement, it is much easier, faster and has a better repetitious accuracy to set up a calculation model.

In the discussed test case, up to 76 zones in DARWIN have been defined in the component, and the probability of failure has been calculated with different zone definitions and SIF solutions. DARWIN has capabilities to use uni- and bivariant and corner crack stress intensity factor solutions. Figure A.14 shows the results for the univariant SIF solutions and Figure A.14 for the bivariant SIF solutions.

In case of the univariant SIF solution the DARWIN calculated PoF converges with increasing number of zones towards the *ProbFM* calculated PoF (Figure A.14). Up from 36 zones, the solutions seem to be converged, i.e. with increasing radial radial resolution, as there is no change in the PoF by increasing the number of zones in radial direction up to 76 (not shown in Figure A.14). Potentially, the PoF converges further to the *ProbFM* PoF if the zones would be further refined in axial direction. As the DARWIN graphical user interface is already at its limits, this analysis has not been performed.

Using the bivariant SIF solutions in DARWIN, the PoF converges at high zone numbers nearly perfectly to the *ProbFM* calculated PoF (Figure A.15). At this point it should be noted that the *ProbFM* calculations have been done without using the

gradient information from the stress field and no corner crack solution is implemented in *ProbFM*. Therefore, it seems to be more important to calculate cracks at different positions in the component than having more complex bivariant SIF solutions, as gradients are implicitly picked up by large number of fracture mechanics simulations within one zone.

The convergence behavior of the bivariant PoF with increasing number of zones shows that the highest stressed location in a zone is not necessarily the most critical location. Otherwise, it is expected that the PoF decreases with increasing number of zones which is not necessary the case as shown in Fig. A.15. In DARWIN it is possible to separate individual $PoFs$ of the different zones. By these means the increased PoF — in particular visible for low cycles — for the 18 to 36 zones calculations can be identified by corner cracks representing the whole zone. By increasing the number of zones, this increased PoF vanishes, as in the limit of small zones the weight of corner cracks vanishes. Therefore, the impact of corner cracks for the investigated components here is negligible. This can be understood as the corner crack is only a singular event in a two dimensional object with a limited number of corners. Corner cracks however, might become more important if crack nucleation at corners and subsequent crack growth are life limiting conditions.

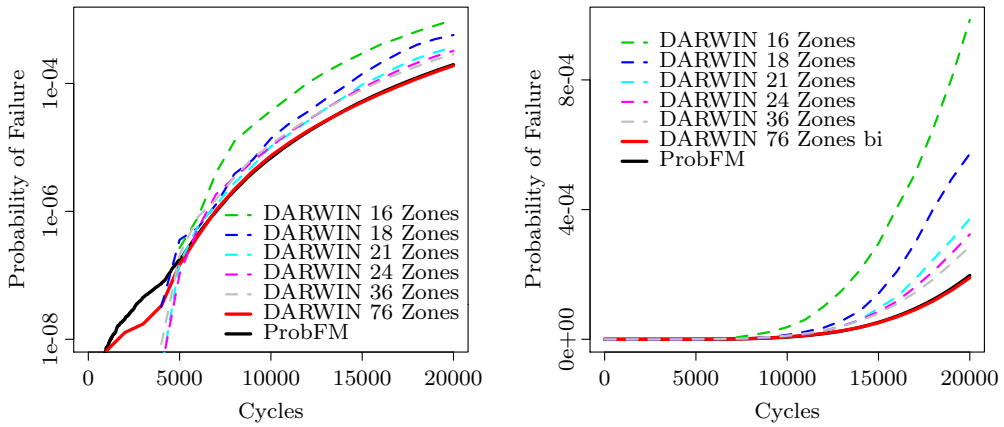

(a) Logarithmic scale (b) Linear Scale

Figure A.14.: Comparison of the convergence of the Probability of failure in DARWIN depending on the zones using univariant SIF solutions. For comparison the converged 76 zone bivariant solution is shown.

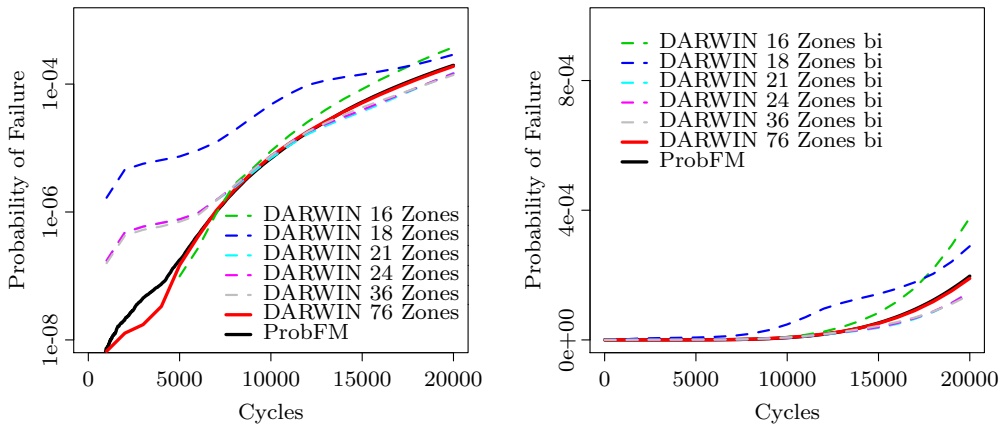

(a) Logarithmic scale (b) Linear Scale

Figure A.15.: Comparison of the convergence of the probability of failure in DARWIN for an increasing number of zones using bivariant SIF solutions. The *ProbFM* solution is almost identical with the 76 zone DARWIN solution.

A.5. Experimental Fracture Mechanics Validation for Large Forgings

Within the framework of the development of the *ProbFM* methodology a set of high stress fracture mechanics tests have been conducted at the *Fraunhofer Institut für Werkstoffmechanik* (IWM) in Freiburg Germany. The complete results are listed in the Report *Investigation to the extension of flaws under cyclic loading* IWM Report V 373/2011.

The aim of the experiments was to validate the LEFM at high, service relevant stresses and to confirm the existence of a nucleation time for natural defects to assure the conservatism of the assumptions made in the probabilistic calculations. Four specimens have been manufactured from a forged rotor disk billet with ultrasonic indications. After testing, only three of the specimens have revealed a visible defect in the fracture surface. The fourth specimen failed in the specimen transition radius. Subsequently the specimen has been broken up at the anticipated crack location but no visible defect could be detected. Hence, only three specimens are discussed in the following. For confidence reasons quantitative details of crack growth and predictions are not shown here.

The specimens have been manufactured in a way that the indications were as good as possible in the center of the tensile specimens and have been cycled at stress levels from 600MPa up to 800MPa with different stress ratios R. After testing, the specimens have been broken up, the crack growth has been measured and the visible flaw area has been compared with the ultrasonic indication size. The specimens were named FZ1, FZ2 and FZ3 and the cross section dimension are shown in table A.7.

Specimen	Cross section [mm^2]	KSR [mm]
FZ1	30 x 20	1.3
FZ2	52 x 35	2.7
FZ3	30 x 20	1.6

Table A.7.: Specimen cross sections and ultrasonic indication size

The test results of the specimens have been compared with the theoretically expected crack sizes. The theoretical crack sizes have been calculated using the software IWM VERB [61]. These indications are the reason why this disk has been rejected for service use.

To calculate the crack growth, the average Paris parameters have been used which have been estimated from crack growth rate measurements, also conducted at the Fraunhofer IWM.

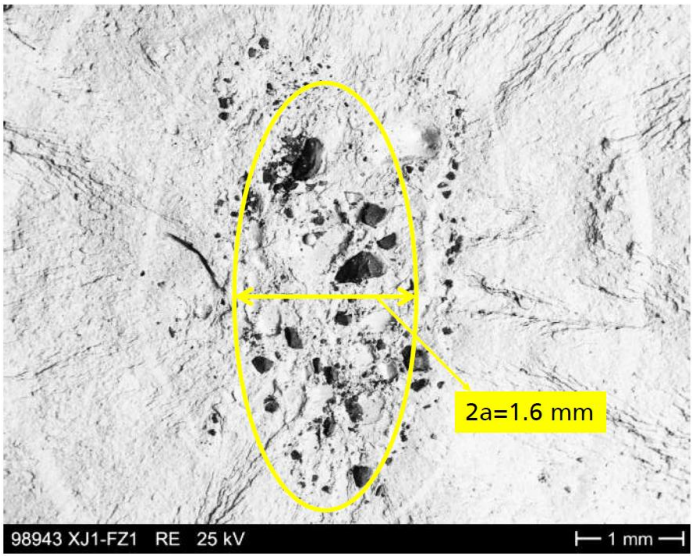

Figure A.16.: Inclusion field of FZ1 with estimated elliptic crack shape and size as determined by ultrasonic inspection and subsequent conversion into WEFG.

A.5.1. Indication 1

The ultrasonic indication of FZ1 has had a size of 1.3 KSR (FBH). According to [29] the KSR (FBH) has to be converted into a WEFG. Furthermore, an elliptic crack with an aspect ratio of 0.4 is assumed (A.5) and (A.6).

$$a = \frac{2KSR}{\sqrt{10}} = 0.82\text{mm} \tag{A.5}$$

$$c = 2.5\frac{2KSR}{\sqrt{10}} = 2.06\text{mm} \tag{A.6}$$

The specimen has been cycled with nine blocks with maximum stresses of 600MPa and 800MPa. In the eighth block the plastic deformation of the specimen increased significantly. After the cycling procedure the specimen has been broken up and the size of the ultrasonic indication has been measured. As shown in Figure A.16, the assumed flaw size matches well the size of the inclusion field which has been found after opening the specimen. The optical flaw size measurement is not a well defined task as in general natural flaws are not of elliptical shape and they consist of groups of smaller inclusions.

The beach marks indicate that during the first 6000 cycles no crack growth has occurred. Assuming the estimated crack size from the ultrasonic examination and the 50% crack growth rate, during approximately 600cycles of the first 800MPa load block, no crack growth has occurred either.

By comparing the measured and the calculated crack sizes it is obvious that the calculation overestimates the crack sizes. Additionally it seems that the 800MPa load blocks introduce compressive stresses in the plastic zone in front of the crack which reduce the crack growth rate during the following 600MPa load block.

A.5.2. Indication 2

Specimen FZ2 has had the largest cross section and contained the largest ultrasonic indication. During the second load block with 800MPa, one of the load transfer bolts started bending and the specimen was shifted out of the centerline. In the following the specimen was re-adjusted and in the cycling was continued with the third load block. In the fourth load block, the load transfer bolt finally was broken after 65 cycles. After replacing the broken bolt, the test was continued with a maximum stress of 600MPa. After another 3824 cycles, the second bolt broke too. Upon replacement of the bolt, the cycling with an maximum stress of 600MPa was continued until the deformation of the specimen significantly increased. The specimen has been subject to more than 33000 cycles in total.

A.5.3. Indication 3

Specimen FZ3 has been tested in two load blocks. The first load block consisted of 20000 cycles with a maximum stress of 600 MPa and an R-ratio $R = 0.1$ and a second block of 20000 cycles with a maximum stress of 800MPa with the same R-ratio. Every 6000 cycles, the R-ratio has been changed to $R = 0.5$ for a small number of cycles to introduce beach marks in the fracture surface to enable a measurement of the crack growth rate.

During the first load block no increase in the deformation of the specimen has been observed. The deformation increased significantly after 19900 cycles of the second load block with 800MPa and the specimen has been broken up cycling it with a maximum stress of 600MPa.

In the following analysis of the fracture surface, the beach marks, which should be introduced by the changed R-ratio, could not be detected. The fracture surface reveals no crack growth marks during the first 20000 cycles with a maximum stress of 600MPa. Thus, it is assumed that no crack growth has occurred during the first load block, indicating a long nucleation time of forging flaws.

A.5.4. High Stress Test Conclusion

The high stress tests of specimens with forging flaws document that a significant amount of cycles is needed to nucleate a crack from the forging flaws even at high stress levels. Thus, the probabilistic modeling approach overestimates the probability of failure as the time to nucleate a crack is assumed to be 0. As only a very limited amount of specimens have been tested, it is not possible to deduce a model for the nucleation process from these tests. Nevertheless it is expected from the tests that the nucleation time is somehow anti-proportional to the applied stress and the inclusion size. Different types of forging flaws will also represent different nucleation behavior.

Furthermore, the tests show that the linear elastic fracture mechanics approach in conjunction with the 50% crack growth rates, measured with CT-specimens at lower stress levels, overestimates the crack growth rates in the tested high stress specimens. Thus, the LEFM approach using the stress intensity factor range as crack growth dominating factor can be used as a conservative approach for estimating the crack growth.

Additionally, the results show that the crack growth rate is significantly overestimated if a 600MPa load block follows a 800MPa load block. This might be related to additional compressive stresses which are introduced in the plastic zone in front of the crack. This suggests that the crack growth rate after, for instance, an over speed condition is overestimated.

Furthermore, the test at service conditions show that all indications would not have led to failure during typical service intervals. This demonstrates additional layers of conservatism. Additional research in the area of crack nucleation, experimental tests, as well as theoretical micro mechanical modeling approaches should be used to investigate this topic further.

B. Sensitivity Study

As the probabilistic fracture mechanics approach includes several different input parameters, it is important to determine the influence of those inputs on the results to get information of the main driving parameters. The local sensitivity depends on the curvature of the failure surface at a particular position of the PoF, and can therefore be estimated locally.

The sensitivities of two components with different risk levels have been analyzed (Fig. B.1). As there is no analytic solution available, the sensitivity has been analyzed by numeric means by varying inputs in typical orders of magnitude. The results were than compared to a baseline (BL) analysis.

The PoF of the medium risk component is about 80 times larger than the PoF of the low risk component after the calculated number of cycles.

B.1. Sensitivity Study of a Medium Risk Component

In Figures B.2 to B.4 the results of the sensitivity study of the medium risk component are shown.

In case of the medium risk component, the fracture toughness, the conversion factor, the decision limit and the PoD_{dat} have a significant influence on the calculated PoF.

The fracture toughness sensitivity has been tested by calculating the PoF with different models for the residual scatter: model free, no scatter, normally distributed, as well as different distribution tail cut off margins: minimum/maximum values and 4 sigma. Model free in this context means that only the measured test data residuals have been used for the simulation and have not been drawn from a fitted distribution. The minimum/maximum residual cut of margins are defined by the minimum/maximum observed residual of the measurements. All the results in Fig. B.2a have been calculated with the same median fracture toughness curve except the deterministic minimum curve, which has been calculated using a typical K_{Ic} curve used in deterministic assessments.

The conversion factor distribution sensitivity (Fig. B.2b) has been tested by using the published conversion factors from Kern [29] (BL) and Schwant [54] (GE) and using the deterministic conversion factor named in the FKM Richtlinie ($k = 2$), and the mean of the Kern distribution ($k = 1.42$). The conversion factors published by

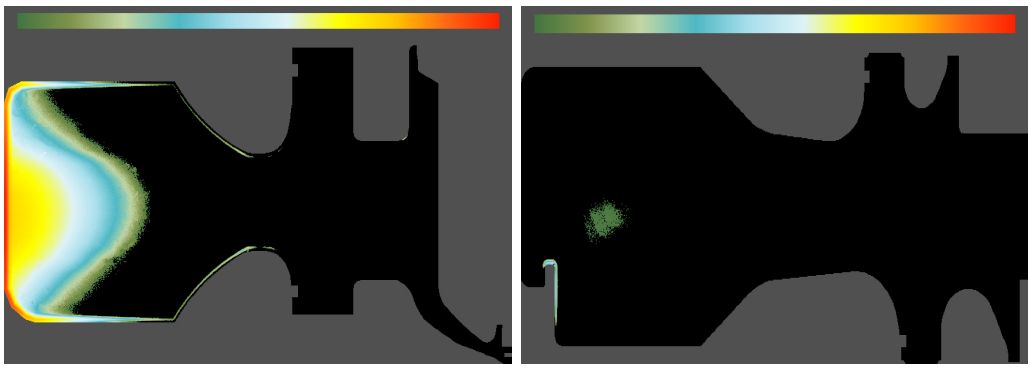

(a) medium risk component (b) low risk component

Figure B.1.: Failure rate maps of the medium and low risk component used for the sensitivity analysis. (Figures not to scale.)

Schwant are much bigger than the conversion factors published by Kern. This is related to changes in the ultrasonic inspection technology, for instance the demand to maximize the echo height of an indication, as well as the difference between GE's and Siemens' ultrasonic specifications in general.

Compared to the uniform flaw distribution, the radial flaw distribution only has a minor effect on the PoF as the component has a large hole in the center and many flaws are cut out, and the peak in the flaw density for small radii (Fig. 2.25) does not affect the PoF of this component significantly.

The influence of the PoD and the KSR_{dec} value in general have significant influence on the PoF (Fig. B.2c, Fig. B.3a and Fig. B.3b). However, if, for instance, the PoD_{dat} is much higher than the PoD_{acc}, consequently the PoD_{acc} has only small influence to the PoF and vice versa; the same is true for the KSR_{dec}. If KSR_{dec} is in the order of a 'critical' crack size or larger it has a significant influence to the PoF. Hence for reasonable PoDs, the PoD_{dat} and the PoD_{acc} have only a small influence to this design. Both calculations which show a strong deviation from the baseline (BL) are calculated for extreme cases, such as a 50% PoD for all flaw sizes or a 50% PoD at a $TFS = 3mm$ with $KSR_{lim} = 1.5mm$, this underlines the significance of a high fidelity ultrasonic inspection of the forgings. In the latter case nearly no flaws will be removed as only very few of the detected flaws are detected with a size larger than KSR_{lim}. Depending on the critical crack size distribution in the component at the last cycle, and how the initial crack size distribution evolves, the value of KSR_{dec} can

have a major influence on the PoF.

In general, the FE results are deterministic stress and temperature values. However, it is known that there are uncertainties in the boundary conditions of the FE calculations. To study the influence of this uncertainty on the PoF, a normally distributed relative scatter with $\pm 4\sigma$ cut off has been applied artificially to the stress field. As the uncertainty of the FE analysis is unknown three different σ values of 5% 10% and 20% (respectively 0.05, 0.10 and 0.2 =) are applied. In general the error of a FE calculation is expected to be within 5% to 10%. The 20% can be interpreted as a severe deviation of the service conditions from the design assumptions. Within the expected accuracy of FE calculations, 5% and 10%, the applied stress scatter shows only a small influence on the PoF. With an assumed $\sigma = 20\%$, the PoF deviates strong from the baseline, but it should kept in mind that in this case the stresses are multiplied by values of up to 1.8.

The influence of the different fracture mechanics methods LEFM, FAD and IPZE (Fig. B.3d) is somewhat significant, but not as pronounced as the influence of the aforementioned factors. Here, the LEFM assessment calculates by far the smallest PoF followed by the FAD, and the IPZE shows the highest PoF. The IPZE PoF curve intercepts the FAD PoF curve. This is related to the fact that the FAD only applies to the failure criterion as it effectively reduces the fracture toughness. Thus the FAD at low cycle numbers predicts a higher PoF than the IPZE. For larger cycle numbers this changes as the IPZE increases the effective crack size and by this it influences the crack growth rate and the failure criterion.

The scatter of the crack growth rate and the tensile properties have only a small influence on the PoF (Fig. B.4a). A calculation with a correlated conversion factor distribution, as explained in chapter 2.8.5, yields as expected a more conservative PoF than the same calculation with decorrelated conversion factors (Fig. B.4b). Fig. B.4c shows that the calculation with ultrasonic expert PoD estimates and a calculation using $PoDs$ based on the TVT which are in good agreement to each other, which supports the assumptions made for the PoD, as no real measured PoDs are available for large rotor forgings.

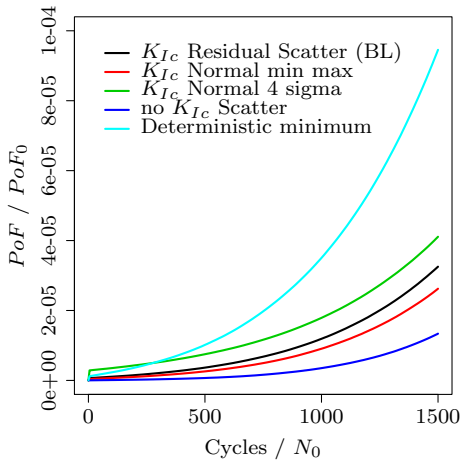

(a) Influence of the K_{Ic} curve and scatter

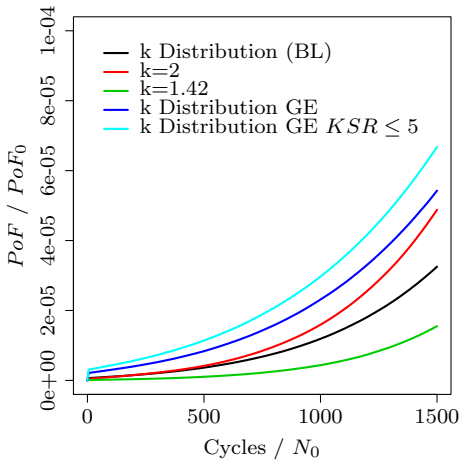

(b) Influence of the conversion factor and scatter

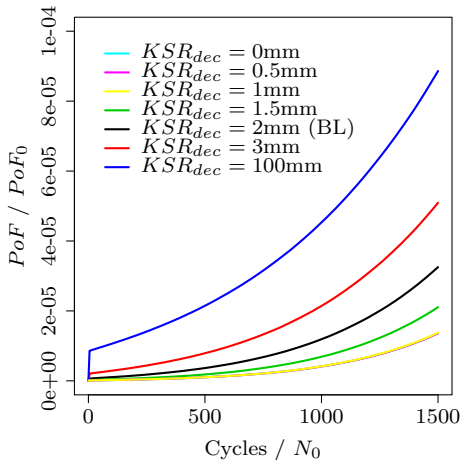

(c) Influence of the KSR decision limit

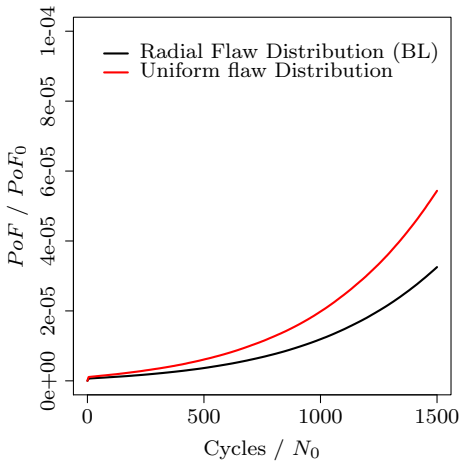

(d) Influence of the radial flaw density

Figure B.2.: *ProbFM* sensitivity studies of medium risk component, baseline is denoted by BL

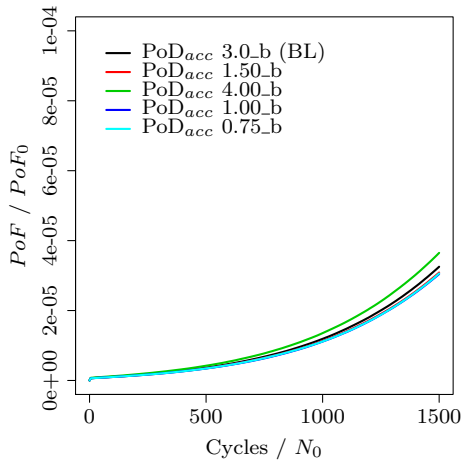

(a) Influence of the acceptance PoD

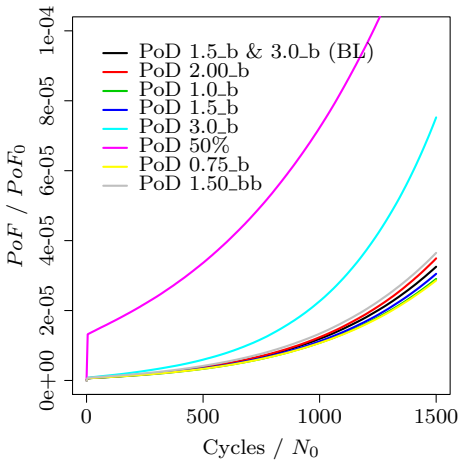

(b) Influence of Database and acceptance PoD

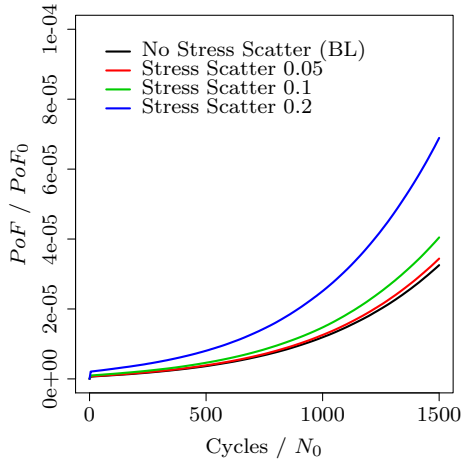

(c) Influence of Stress uncertainty

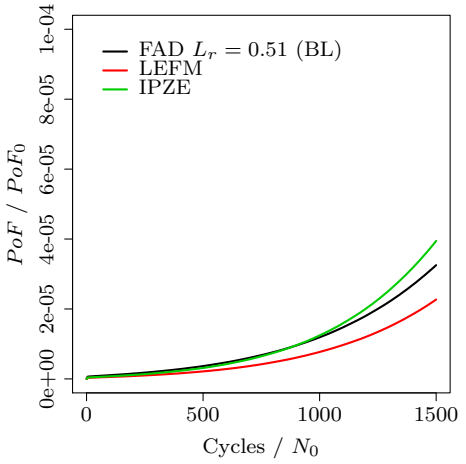

(d) Influence of linear and nonlinear fracture mechanic

Figure B.3.: *ProbFM* sensitivity studies of medium risk component, baseline is denoted by BL

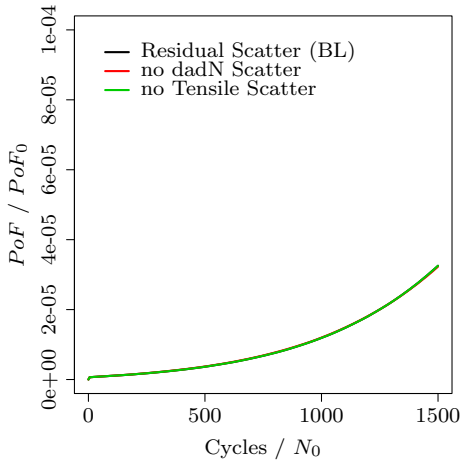

(a) Influence of the crack growth rate and the tensile properties scatter on the PoF

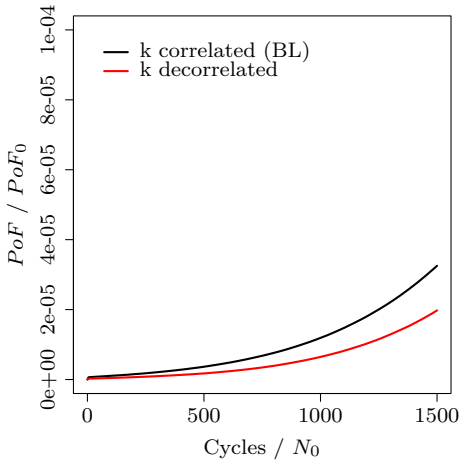

(b) Influence of the conversion factor correlation

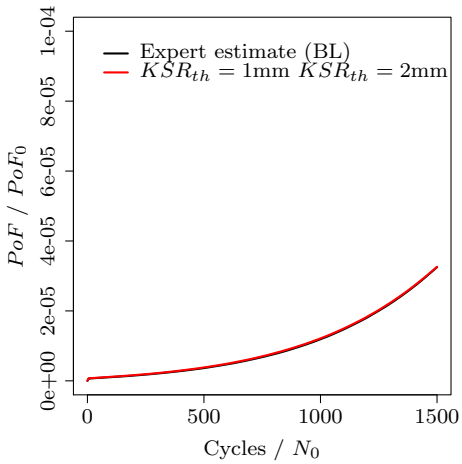

(c) Comparison PoD Expert and threshold value theorem estimate

Figure B.4.: *ProbFM* sensitivity studies of medium risk component, baseline is denoted by BL

B.2. Sensitivity Study of a Low Risk Component

In Figures B.5 to B.7, the results of the sensitivity study of the low risk component are shown. The calculations have been done with the same inputs as for the medium risk component.

In Fig. B.5a, the influence of the fracture toughness is shown. The normal distribution with 4 σ cut off shows the biggest relative impact on the PoF. This behavior is related to the overall low PoF of this component. By allowing the very low likelyhood tail to contribute, additional failures occur. This contribution is small compared to general acceptable risk limits and is therefore not relevant for component design.

As shown in Fig. B.5b, the difference between conversion factor distribution published by Kern [29] and the constant conversion factors is small. This is related to the fact that both constant conversion factors are contained in the conversion factor distribution and at this low PoF only the large conversion factors contribute to the PoF. For the same reason the conversion factor distribution published by Schwant [54] produces larger PoF values as it allows for larger conversion factors.

The uniform flaw distribution has nearly no effect on the PoF (Fig. B.5d) as the component PoF is dominated by a very small area at which the uniform and the radial flaw distribution are at the same level.

The decision limit has a major impact on the PoF as especially the 'infant mortality' probability is increased since the large flaws which can cause an immediate failure of the component are not rejected. 'Infant mortality' in this context means that flaws in the component will cause an immediate failure of the component in the first cycle. Furthermore, other non critical areas of the component produce failures due to the large flaws with increasing number of cycles.

It seems that at least in the range of typical variation, the PoD only has a small influence on the PoF (Fig. B.6a and Fig. B.6b).

The influence of the fracture mechanics model (Fig. B.6d) is small as the component load is such small that only small effects due to these plastic corrections occur.

Fig. B.7a shows that the influence of the scatter of the crack growth rate and the tensile properties is very small.

As expected, the influence of the correlation of the conversion factor distributions is small and in the correlated assessment delivers the higher PoF (Fig. B.7b).

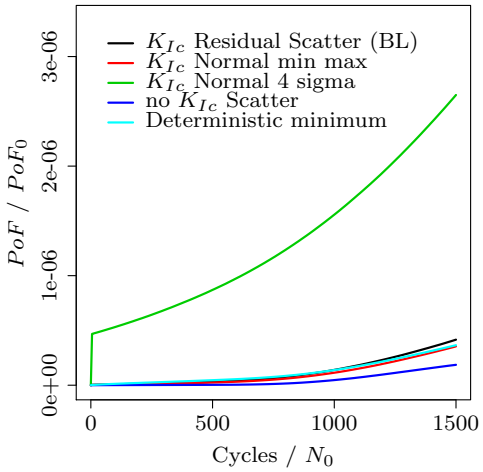

(a) Influence of the K_{Ic}curve and scatter

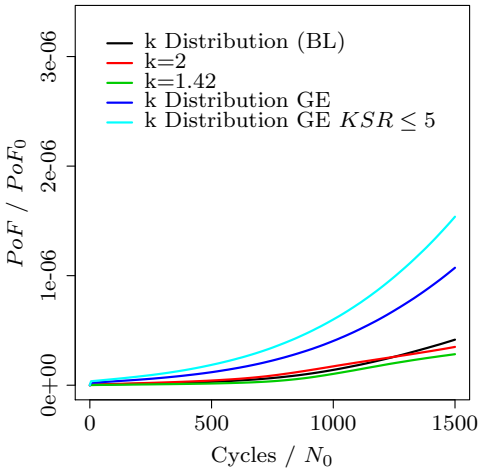

(b) Influence of the conversion factor and scatter

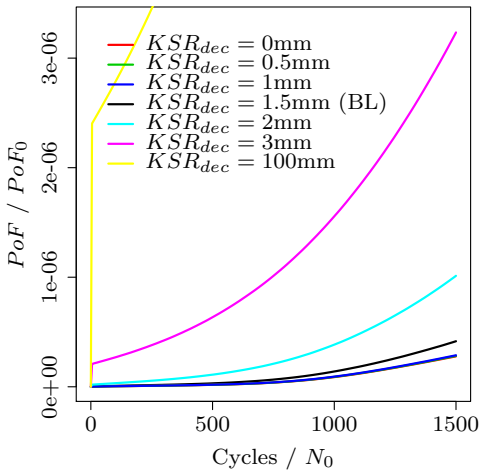

(c) Influence of the KSR decision limit

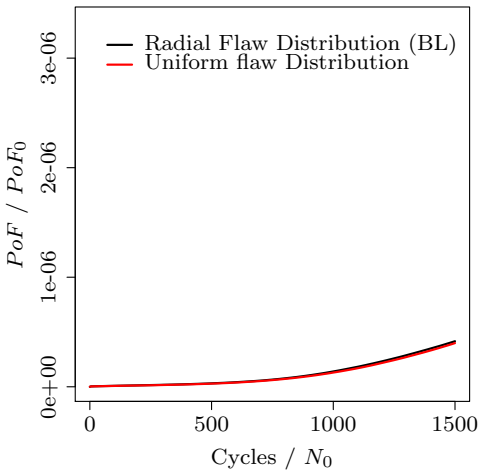

(d) Influence of the radial flaw density

Figure B.5.: *ProbFM* sensitivity studies of low risk component, baseline is denoted by BL.

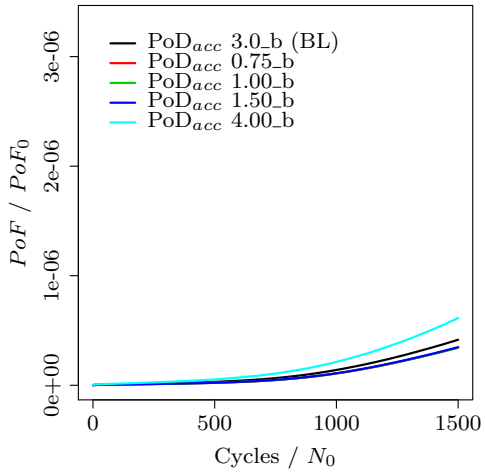

(a) Influence of the acceptance PoD

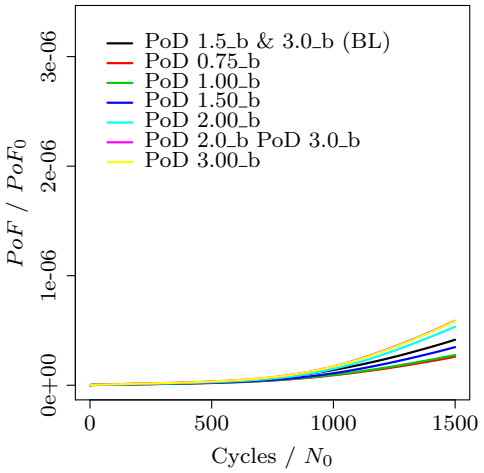

(b) Influence of Database and acceptance PoD

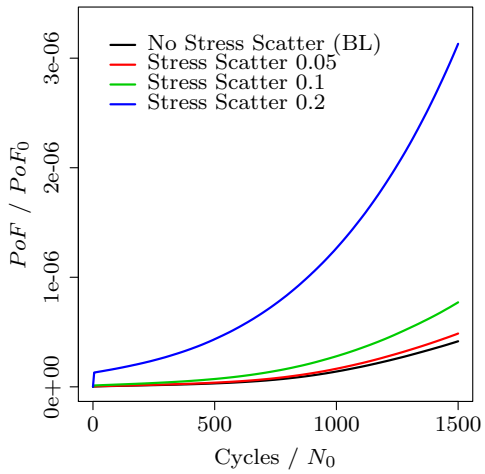

(c) Influence of Stress uncertainty

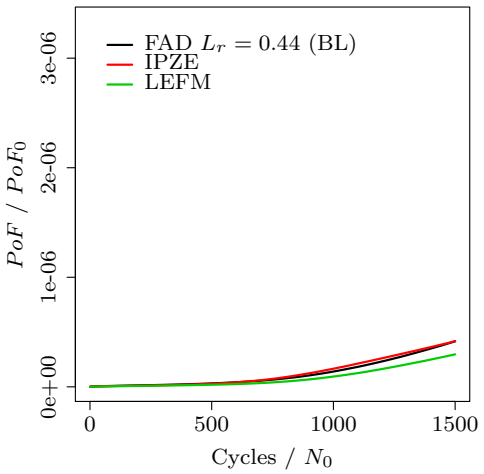

(d) Influence of linear and nonlinear fracture mechanic

Figure B.6.: *ProbFM* sensitivity studies of low risk component, baseline is denoted by BL.

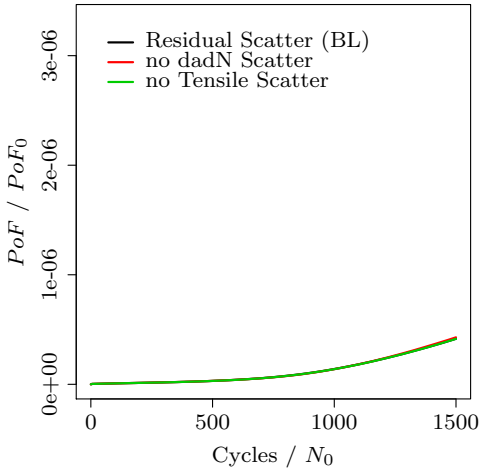

(a) Influence of the crack growth rate and the tensile properties scatter on the PoF

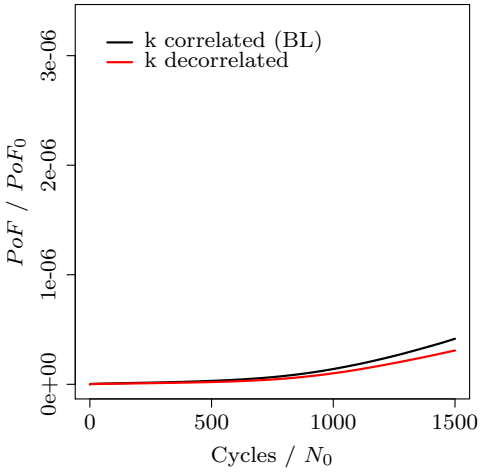

(b) Influence of the conversion factor correlation

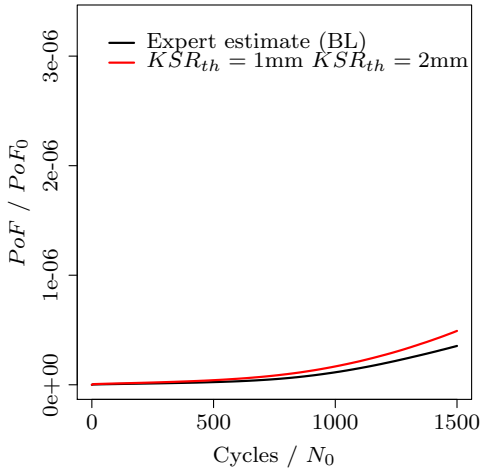

(c) Comparison PoD Expert and threshold value theorem estimate

Figure B.7.: *ProbFM* sensitivity studies of low risk component, baseline is denoted by BL.

B.3. Comparison of Medium and Low Risk Results

In the two previous sections the sensitivity study results of a medium and a low risk components have been presented.

For some input parameters both components can show a different dependency.

For instance, the fracture toughness and the parameters of the ultrasonic model have a big influence to the PoF for both components.

The scatter of the crack growth rate and tensile properties have a much smaller effect on the PoF. The crack growth scatter sensitivity depends on the number of cycles calculated. For a larger number of cycles, the sensitivity of the scatter in the crack growth rate becomes larger. As the investigated examples have only been calculated up to a typical component design life, the sensitivity of the PoF is strongly controlled by cracks which are already at the beginning close to the critical crack size. Especially for the low risk component, the PoF is very sensitive to the smallest possible K_{Ic} (Fig. B.5a), as this raises the infant mortality.

Both components have a very different deterministic lifetime. Assuming the deterministic calculated lifetimes are correlated to the calculated PoF, the PoF at the end of the deterministic component lifetime should be similar. To compare the $PoFs$ and Hazard rate in Figures B.8a and B.8b, the number of cycles has been normalized by the deterministic calculated life cycle number. As shown here, the PoF and the Hazard rate at the end of the deterministic lifetime differs by orders of magnitude. This has multiple reasons. One is to find an appropriate crack location for the deterministic analysis in the component which describes the crack growth in a representative way for the whole component.

Another reason is the size effect. In general, in a deterministic approach, the most critical location, i.e. region with high stress, in a component is used for the life cycle calculation. In some components like the low risk component (Fig. B.1b), the high stress is localized in a narrow volume. Therefore, it is very unlikely that an inherent forging flaw is located in this volume. On the other hand, in the medium risk component (Fig. B.1a) a larger volume is exposed to high stresses and hence it is more likely to find a flaw within this volume.

The comparison between the low and medium risk components demonstrates the two different lifing philosophies between deterministic and probabilistic fracture mechanics, namely the safe-life approach suggesting zero tolerance for failure and no ability to quantify risk, and the probabilistic approach accepting a low failure probability and allowing for risk management. Both analyzed components are well below the acceptable risk limit beyond the design life.

In conclusion the largest influence is the quality of the forgings specified by the

ultrasonic indications and the PoD. That underlies the importance of a continued quality control process by ultrasonic for the forgings. The fracture toughness and potential degradation with service time (aging) is also very important for the structural integrity of large rotating components.

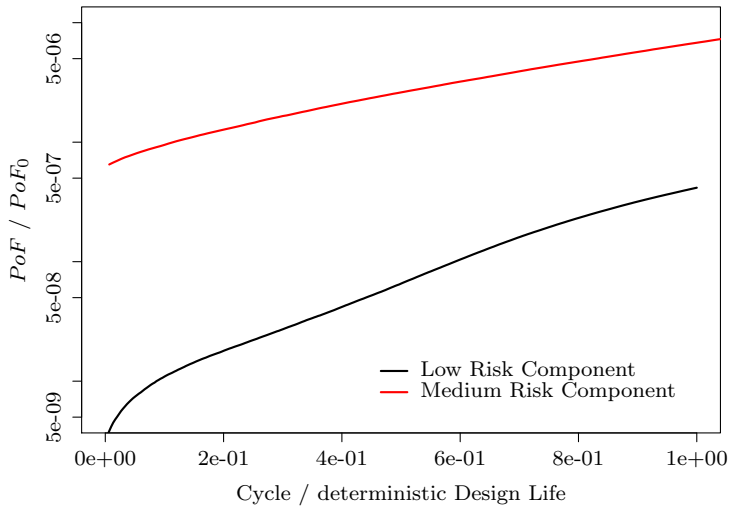

(a) Comparison of the PoF

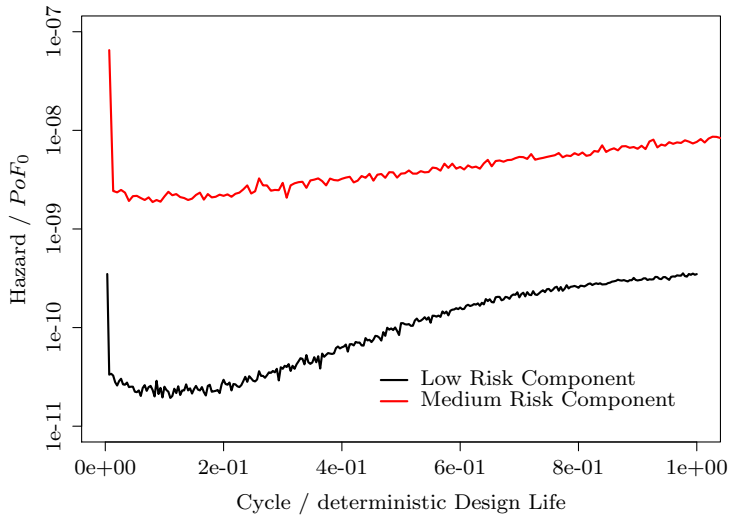

(b) Comparison of the Hazard rate

Figure B.8.: Comparison of PoF and hazard rate of the medium and low risk components versus the normalized number of starts.